Chapter 10

THEORY OF LOW-ENERGY ELECTRON DIFFRACTION AND PHOTOELECTRON SPECTROSCOPY FROM ULTRA-THIN FILMS

Jürgen Henk*
Max-Planck-Institut für Mikrostrukturphysik, Halle/Saale, Germany

Contents

1. INTRODUCTION

If an extended condensed-matter system is reduced in its dimensionality, it can exhibit novel physical properties. These finite-size or quantum-size effects are fascinating from a fundamental point of view as being likewise important with regard to technological applications. For example, quantum wells and superlattices build up by semiconductors or magnetic metals are prominent examples for intensively investigated and applied systems [1, 2].

When reducing the dimension from three to two, one goes from the "bulk" system to an "ultra-thin" film. For the latter, the extension in one dimension is small compared to those in the two other dimensions. What, however, actually is meant by "ultra-thin" depends on the physical quantity under consideration. Because this chapter is on electron spectroscopies, ultra-thin films can be regarded as of a few nanometer thickness. The properties of ultra-thin films are obviously determined by the material of the "bulk" system. However, because films are (usually) realized by evaporation on a substrate, their properties can significantly be influenced by the film–substrate interface, especially for films a few angstroms thick.

Probably the most striking fact of films is that electrons can become confined to the film and thus show discrete energy levels; that is, the electron energies become quantized with respect to the direction normal to the film. Many properties of films can be attributed to these quantum-well states (QWSs). For example, the giant magnetoresistance (GMR) effect [3], that is, the change of the resistance of a stack of magnetic films (usually named multilayer or superlattice) due to the arrangement of the magnetic moments within each film, can be explained in terms of QWSs. The GMR is still of interest in fundamental science as well as it is applied in modern computer hard disks [4, 5].

The key to the understanding of the various physical phenomena in these systems lies in a detailed knowledge of both

*To my sons Kai-Hendrik and Jan-Malte.

ISBN 0-12-512910-6/$35.00

Handbook of Thin Film Materials, edited by H.S. Nalwa
Volume 2: Characterization and Spectroscopy of Thin Films

their electronic and geometric structures, which are intimately related. Two prominent experimental techniques that allow for detailed investigations of these properties are low-energy electron diffraction (LEED) and angle-resolved photoelectron spectroscopy (ARPES). Both have been very successfully applied to semi-infinite systems. However, applied to an ultra-thin film on a substrate, features in the spectra occur that are closely related to the particular electronic states within the film; that is, they are direct manifestations of QWSs in the spectra. Therefore, these signatures give access to the electronic and geometrical structures of the film–substrate system and can further be related to more fundamental quantities, for example, the thickness and the magnetization of the film.

Because the interpretation of experimentally obtained LEED and ARPES data is rather difficult without theoretical aid, there is need for a theoretical description of the electronic structure of the film–substrate system and, based on this, of the spectroscopies. Basic physical properties can be obtained by *ab initio* total-energy calculations. But these often do not provide a direct link to spectroscopically measured quantities, such as, for example, LEED intensities or photocurrents. Therefore, theoretical methods have to be developed that are based on *ab initio* results and yield spectroscopic quantities that can directly be compared to experimental data.

This chapter first introduces the geometrical and electronic description of ultra-thin films (Section 2). In Section 3, theories of LEED at various levels of sophistication together with some applications are presented. Subsequently, theories of ARPES are given (Section 4). A complete coverage of ARPES is clearly beyond the scope of this chapter. Therefore, it focuses on photoemission from valence states that are excited by light within the vacuum-ultraviolet (VUV) range of photon energies, the latter being well suited for the study of QWSs. Further, important experimental results are used to illustrate the theoretical findings. Of particular interest are films formed either by normal or by magnetic metals. A description of magnetic systems is best given by means of a relativistic theory, rather than incorporating the electron's spin into a nonrelativistic theory. In this way, exchange and spin-orbit interaction are treated on an equal footing (which is essential for understanding some of the effects). Therefore, multiple-scattering theory is introduced in its relativistic form. This requires some background knowledge of quantum and solid-state physics. For the reader interested in more details, references to review articles and books as well as to important original articles are given.

2. THIN FILMS AND QUANTIZED ELECTRONIC STATES

In this section, we introduce the geometry of films on a substrate (Section 2.1) and describe electronic states within a film (Section 2.2).

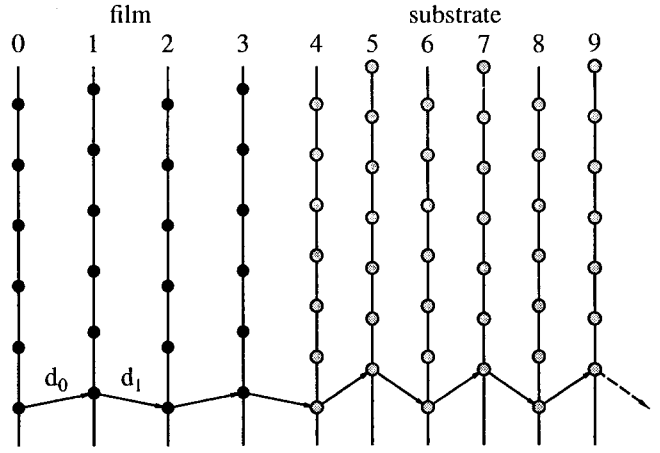

Fig. 1. Geometrical arrangement of an ultra-thin film grown on a substrate. The film consists of layers (vertical lines) $j = 0, \ldots, 3$ connected by translation vectors $\mathbf{d}_j$. The substrate is made up by all layers $j \geq 4$. Sites are represented by black (film) or gray (substrate) circles.

2.1. Films, Substrates, and Lattices

Before turning to the description of electrons confined to an ultra-thin film, one has to consider the geometry of the system under consideration. An ultra-thin film can be regarded as stack of layers, the basic object, grown on a substrate. Each layer consists of sites (circles in Fig. 1) that form a lattice.[1] In principle, these two-dimensional lattices may vary from layer to layer. This is schematically depicted in Figure 1: The distance between next-nearest sites in the film and the substrate layers differs. Especially at the surface (layer index $j = 0$), sites can be rearranged in such a way that the two-dimensional lattice at the surface differs from those of the other layers. For example, the (110) surface of Pt shows a reconstruction where each second row of Pt atoms is missing [the "missing-row" reconstruction of Pt(110)1 × 2 [6]].

Each layer j is connected to the next-nearest layer $j + 1$ by a translation vector $\mathbf{d}_j$. The latter may be different for each layer, in particular, at the surface where usually $\mathbf{d}_0$ can differ considerably from that of the other layers; that is, there is layer relaxation.

Geometrical rearrangements such as relaxation and reconstruction usually take place near the surface. Deep in the interior of the system, all layers are identical; that is, they show the same lattice and the same translation vector $\mathbf{d}$. We take this feature as the definition of the bulk system (i.e., an infinitely repeated arrangement of identical layers). Note that for some systems the repeated entity does not consist of a single layer but of a stack of layers. One can comprise this stack into a principal layer and use this as the basic quantity. For example, in Figure 1 a principal layer would consist of two substrate layers.

[1] A two-dimensional (three-dimensional) lattice is a set of vectors that can be expressed as the set of all integral linear combinations of two (three) basis vectors, not all along the same direction (in the same plane).

After considering the basic geometry of film and substrate, we can turn to the structure of the layers (i.e., the two-dimensional lattices).

2.1.1. *Two-Dimensional Crystal Structures*

Because the surface breaks the three-dimensional periodicity of the bulk, the 14 Bravais lattices [7] of the latter are no longer suitable for the description of semi-infinite systems. Instead, one is concerned with five types of two-dimensional nets, the translation vectors of which connect identical positions (see, e.g., [6, Chap. 3]).

Consider the unit cell[2] of the substrate spanned by the vectors $\mathbf{a}_1$ and $\mathbf{a}_2$ [8, 9],

$$\mathbf{a}_1 = a_{11}\mathbf{e}_1 + a_{12}\mathbf{e}_2 \tag{1a}$$

$$\mathbf{a}_2 = a_{21}\mathbf{e}_1 + a_{22}\mathbf{e}_2 \tag{1b}$$

where $\mathbf{e}_1$ and $\mathbf{e}_2$ are orthonormal vectors. The preceding equations establish the matrix A,

$$A = \begin{pmatrix} a_{11} & a_{12} \\ a_{21} & a_{22} \end{pmatrix} \tag{2}$$

It can easily be verified that the area of the unit cell F_A is given by the determinant of A, $\det(A)$.[3] Note that each translational vector reads $\mathbf{t} = m\mathbf{a}_1 + n\mathbf{a}_2$ with m and n integers, that is, $m, n \in \mathbb{Z}$. The set of vectors $\mathbf{t}$ defines the two-dimensional lattice. The five two-dimensional Bravais lattices are shown in Figure 2.

The unit cell of the film layers is spanned by the vectors $\mathbf{b}_1$ and $\mathbf{b}_2$, which, in analogy to Eq. (1), gives rise to a matrix B. Both sets of vectors are connected linearly by

$$\mathbf{b}_1 = n_{11}\mathbf{a}_1 + n_{12}\mathbf{a}_2 \tag{3a}$$

$$\mathbf{b}_2 = n_{21}\mathbf{a}_1 + n_{22}\mathbf{a}_2 \tag{3b}$$

which establishes the matrix N. The areas of the unit cells are related by $F_B = F_A \det(N)$.

All periodic lattice structures can be cast into the following three categories [9, 12]:

Simply related structures have all $n_{ij} \in \mathbb{Z}$. Thus, $\det(N)$ is also an integer. For example, commensurate adsorbate layers belong to this class.

Coincident structures have rational n_{ij}. Incommensurate adsorbed layers belong to this class.

Incoherent structures have irrational n_{ij}. In contrast to the other two cases, there is no common periodicity of substrate and film.

[2] A unit cell is a region that fills space without overlapping when translated through some subset of the vectors of a Bravais lattice [7].

[3] A general definition of the area which is valid for all spatial dimensions is given by the outer product $\mathbf{a}_1 \wedge \mathbf{a}_2$ of the corresponding geometric algebra [10, 11]. In two dimensions, it corresponds to the determinant, in three dimensions to the cross product $|\mathbf{a}_1 \times \mathbf{a}_2|$.

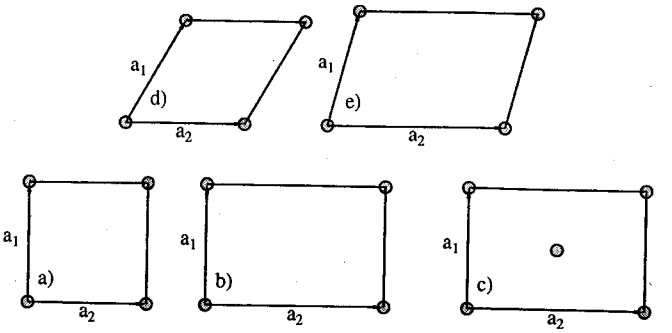

Fig. 2. Two-dimensional Bravais lattices: (a) square ($|\mathbf{a}_1| = |\mathbf{a}_2|$, $\alpha = 90°$), (b) primitive ($|\mathbf{a}_1| \neq |\mathbf{a}_2|$, $\alpha = 90°$), (c) centered rectangular ($|\mathbf{a}_1| \neq |\mathbf{a}_2|$, $\alpha = 90°$), (d) hexagonal ($|\mathbf{a}_1| = |\mathbf{a}_2|$, $\alpha = 60°$), and (e) oblique ($|\mathbf{a}_1| \neq |\mathbf{a}_2|$, α arbitrary), with $\alpha = \angle(\mathbf{a}_1, \mathbf{a}_2)$.

A lattice can be represented either in direct space (covariant representation, $\mathbf{a}_i$) or in reciprocal space (contravariant representation, $\mathbf{g}_i$). Both are related by

$$\mathbf{g}_i \cdot \mathbf{a}_j = \delta_{ij} \qquad i, j = 1, 2 \tag{4}$$

The vectors $\mathbf{g}_i$ from the basis of the reciprocal lattice. Introducing a matrix G by

$$\mathbf{g}_1 = \mathbf{e}_1 g_{11} + \mathbf{e}_2 g_{21} \tag{5a}$$

$$\mathbf{g}_2 = \mathbf{e}_1 g_{12} + \mathbf{e}_2 g_{22} \tag{5b}$$

gives, using Eq. (4), $G = A^{-1}/F_A$. Thus, the area of the unit cell of the reciprocal lattice is $F_G = 1/F_A$. Defining in analogy to Eq. (5) the reciprocal net of the film layers, that is, the matrix H, and the relating matrix M, the latter is given by $M = N^{-1}$.

As we have seen, the space can be filled with (conventional) unit cells. One can also fill the space by cells with the full symmetry of the Bravais lattice, for example, with Wigner–Seitz cells. The latter are defined as regions in space about a lattice point that are closer to that particular point than to any other lattice point. The Wigner–Seitz cell of the reciprocal lattice is called the (first) Brillouin zone [7].

2.2. Quantum-Well States

In 1928, Bloch showed that the energy spectrum of an electron in a solid consists of continuous stripes of allowed energies that are separated by regions of forbidden energies [13]. These stripes are called energy bands; correspondingly, the forbidden intervals are named bandgaps. The energy E of an electron within a band is continuous with respect to the momentum $\mathbf{k}$, which gives rise to the concept of band structure, $E(\mathbf{k})$. Undoubtedly, this concept is one of the most successful in condensed-matter physics. In the following, we discuss the energy spectrum of electrons confined to a film.

Because the geometrical structure and the electronic structure are closely related, several descriptions of electrons confined to a film will be presented (for an introduction, see [14]). In Section 2.2.1, the simple free-electron model will be introduced. The envelope picture presented in Section 2.2.2 can be

regarded as a refinement of the preceding. A tight-binding description is given in Section 2.2.3.

2.2.1. *Free-Electron Description of Quantum-Well States*

As a preliminary, we recall the well-known basics of the electronic structure of an electron in a potential with rectangular shape, the so-called rectangular well (see, e.g., [15]). The well is assumed to be infinitely extended in the xy plane and to extend from $-a/2$ to $a/2$ along the z axis. Thus, it can be regarded as a simple representation of a film. According to the model of a quantum well, the film is structureless in the xy plane, and, thus, the potential function $V(\mathbf{r})$ depends exclusively on z,

$$V(\mathbf{r}) = \begin{cases} U & z < -a/2 \\ 0 & -a/2 \le z \le a/2 \\ U & a/2 < z \end{cases} \tag{6}$$

The three different regions along the z axis are denoted I, II, and III (cf. Fig. 3). For convenience, we introduce the in-plane vector $\boldsymbol{\varrho} = (x, y)$. Therefore, $\mathbf{r} = (\boldsymbol{\varrho}, z)$. Because the potential is symmetric with respect to the plane $z = 0$, that is, $V(\boldsymbol{\varrho}, z) = V(\boldsymbol{\varrho}, -z)$, the electronic wave functions $\Psi(\boldsymbol{\varrho}, z)$ have to have either even (+) or odd (−) parity: $\Psi(\boldsymbol{\varrho}, z) = \pm\Psi(\boldsymbol{\varrho}, -z)$. Further, due to the translational invariance of the potential in the xy plane, that is, $V(\boldsymbol{\varrho}, z) = V(\boldsymbol{\varrho}', z)$ for all $\boldsymbol{\varrho}$ and $\boldsymbol{\varrho}'$, the wave functions obey Floquet's theorem, $\Psi(\boldsymbol{\varrho}+\boldsymbol{\varrho}', z) = \lambda(\boldsymbol{\varrho}')\Psi(\boldsymbol{\varrho}, z)$. Obviously, $\lambda(\mathbf{0}) = 1$ and $\lambda(\boldsymbol{\varrho} + \boldsymbol{\varrho}') = \lambda(\boldsymbol{\varrho})\lambda(\boldsymbol{\varrho}')$, which is the functional equation of the exponential function. Because $|\Psi(\mathbf{r})|^2$ is the probability of finding an electron at $\mathbf{r}$, the wave functions have to be square integrable ($\Psi \in \mathcal{L}_2$), that is, $\int |\Psi(\mathbf{r})|^2 dr^3 < \infty$. With a normalized Ψ (i.e., $\|\Psi\| = 1$), it follows that $|\lambda(\boldsymbol{\varrho})| = 1$ for all $\boldsymbol{\varrho}$. Therefore, one can write $\lambda(\boldsymbol{\varrho})$ as $\lambda(\boldsymbol{\varrho}) = \exp(i\mathbf{k}_\parallel \cdot \boldsymbol{\varrho})$. In conclusion, the wave functions can be written as

$$\Psi(\boldsymbol{\varrho}, z) = \exp(i\mathbf{k}_\parallel \cdot \boldsymbol{\varrho})\Psi(0, z) \tag{7}$$

which (i) establishes a classification of the wave functions with respect to $\mathbf{k}_\parallel$ and (ii) reduces the initially three-dimensional problem to a one-dimensional problem [which has to be solved for $\Psi(0, z)$; the in-plane wave vector $\mathbf{k}_\parallel$ acts as a parameter in reciprocal space].

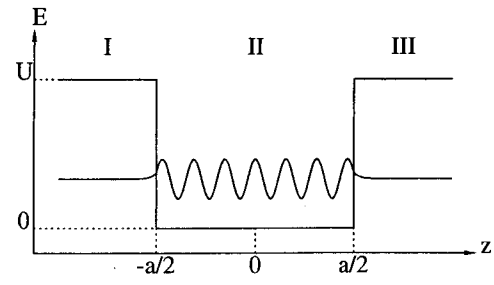

Fig. 3. Quantum well of rectangular shape. The potential $V(z)$ is given as in Eq. (6) with $U > 0$. In the three regions I, II, and III, representatives of the wave functions with energy $0 < E < U$ are shown schematically in addition.

We now solve the time-independent Schrödinger equation[4] for the potential of Eq. (6),

$$\left(-\frac{1}{2}\nabla^2 + V(\mathbf{r})\right)\Psi(\mathbf{r}) = E\Psi(\mathbf{r}) \tag{8}$$

which reduces, using Eq. (7), to the one-dimensional problem[5]

$$\left(-\frac{1}{2}\partial_z^2 + V(z)\right)\Psi(0, z) = \left(E - \frac{1}{2}\mathbf{k}_\parallel^2\right)\Psi(0, z) \tag{9}$$

In region II, the potential vanishes and one is left with

$$-\frac{1}{2}\partial_z^2\Psi^{(\mathrm{II})}(0, z) = \left(E - \frac{1}{2}\mathbf{k}_\parallel^2\right)\Psi^{(\mathrm{II})}(0, z) \qquad \mathbf{r} \in \mathrm{II} \tag{10}$$

which is immediately solved by plane waves,

$$\Psi^{(\mathrm{II})}(\mathbf{r}) = A^{(\mathrm{II})}\exp(i\mathbf{k}_\parallel \cdot \boldsymbol{\varrho})\exp(ik_\perp^{(\mathrm{II})}z) \tag{11}$$

The z component of the wave vector, $k_\perp^{(\mathrm{II})}$, is related to the energy by

$$k_\perp^{(\mathrm{II})} = \sqrt{2E - \mathbf{k}_\parallel^2} \tag{12}$$

In region I, the Schrödinger equation reads

$$-\frac{1}{2}\partial_z^2\Psi^{(\mathrm{I})}(0, z) = \left(E - \frac{1}{2}\mathbf{k}_\parallel^2 - U\right)\Psi^{(\mathrm{I})}(0, z) \qquad \mathbf{r} \in \mathrm{I} \tag{13}$$

and, using the preceding results, Eqs. (11) and (12),

$$\Psi^{(\mathrm{I})}(\mathbf{r}) = A^{(\mathrm{I})}\exp(i\mathbf{k}_\parallel \cdot \boldsymbol{\varrho})\exp(ik_\perp^{(\mathrm{I})}z) \tag{14}$$

with

$$k_\perp^{(\mathrm{I})} = \sqrt{2(E - U) - \mathbf{k}_\parallel^2} \tag{15}$$

Note that $k_\perp^{(\mathrm{I})}$ can be either real [$2(E - U) \ge \mathbf{k}_\parallel^2$] or imaginary [$2(E - U) < \mathbf{k}_\parallel^2$]. For region III, one obtains the same results as for region I.

The next step is to construct the wave function of the entire system. Therefore, one has to match both the wave function and its derivative at the region boundaries, $z = \pm a/2$, for a given energy E and $\mathbf{k}_\parallel$. Because we are interested in bound states, that is, those confined to the well, we choose $U > 0$ and assume $0 < 2E - \mathbf{k}_\parallel^2 < 2U$.[6] In this case, $k_\perp^{(\mathrm{I})}$ and $k_\perp^{(\mathrm{II})}$ are imaginary and real, respectively. Setting $\kappa^{(\mathrm{I})} = ik_\perp^{(\mathrm{I})} > 0$, the ansatz for the wave function reads, using Eqs. (11) and (14),

$$\Psi(0, z) = \begin{cases} A^{(\mathrm{I})}\exp(\kappa^{(\mathrm{I})}z) & \mathbf{r} \in \mathrm{I} \\ A^{(\mathrm{II})}\left(\exp(ik_\perp^{(\mathrm{II})}z) \pm \exp(-ik_\perp^{(\mathrm{II})}z)\right) & \mathbf{r} \in \mathrm{II} \\ \pm A^{(\mathrm{I})}\exp(-\kappa^{(\mathrm{I})}z) & \mathbf{r} \in \mathrm{III} \end{cases} \tag{16}$$

[4] We use atomic units throughout (i.e., $e = \hbar = m = 1$). Lengths are in bohrs ($1a_0 = 0.529177$ Å), energies in hartrees ($1H = 2$ Ry, 1 Ry = 13.6058 eV). The speed of light is given by the reciprocal fine-structure constant, $c = 137.036$.

[5] The notation ∂_z (∂_z^2) is short for d/dz (d^2/dz^2).

[6] There is at least one bound state in this case [16].

where the upper signs are for even parity, the lower ones for odd parity. Note that in region II the two linearly independent solutions $\exp(\pm ik_\perp^{(\mathrm{II})} z)$ were superposed. In regions I and III, one would have had the two solutions $\exp(\pm\kappa^{(\mathrm{I})} z)$ but only one of them is square integrable in the respective region. The matching conditions at $z = a/2$ yield

$$\pm A^{(\mathrm{I})} \exp(-\kappa^{(\mathrm{I})} a/2) = A^{(\mathrm{II})} \left(\exp(ik_\perp^{(\mathrm{II})} a/2) \pm \exp(-ik_\perp^{(\mathrm{II})} a/2)\right) \quad (17a)$$

$$\mp A^{(\mathrm{I})} \kappa^{(\mathrm{I})} \exp(-\kappa^{(\mathrm{I})} a/2) = iA^{(\mathrm{II})} k_\perp^{(\mathrm{II})} \left(\exp(ik_\perp^{(\mathrm{II})} a/2) \mp \exp(-ik_\perp^{(\mathrm{II})} a/2)\right) \quad (17b)$$

(The conditions for $z = -a/2$ give no additional equations.) Because the coefficients $A^{(\mathrm{I})}$ and $A^{(\mathrm{II})}$ remain arbitrary until Ψ is normalized, the two conditions are equivalent to the requirement that the logarithmic derivative of Ψ, $(\partial_z \Psi(0, z))/\Psi(0, z)$, is continuous at $z = a/2$. Using Euler's formulas, one eventually obtains transcendental equations in the wave numbers,

$$\kappa^{(\mathrm{I})} \cos(k_\perp^{(\mathrm{II})} a/2) = k_\perp^{(\mathrm{II})} \sin(k_\perp^{(\mathrm{II})} a/2) \quad \text{even parity} \quad (18a)$$

$$-\kappa^{(\mathrm{I})} \sin(k_\perp^{(\mathrm{II})} a/2) = k_\perp^{(\mathrm{II})} \cos(k_\perp^{(\mathrm{II})} a/2) \quad \text{odd parity} \quad (18b)$$

which can be solved numerically.

At this point, it it illustrative to consider a well with infinitely high barriers. The limit $U \to \infty$ implies $\kappa^{(\mathrm{I})} \to 0$, and, therefore, the wave function vanishes in regions I and III. Thus, there is no requirement for the z derivative of $\Psi(0, z)$, and the remaining matching condition $\Psi^{(\mathrm{II})}(0, \pm a/2) = 0$ immediately gives

$$k_{\perp n}^{(\mathrm{II})} = \frac{\pi}{a} \begin{cases} (2n+1) & n \in \mathbb{N}_0 \quad \text{even parity} \\ (2n) & n \in \mathbb{N} \quad \text{odd parity} \end{cases} \quad (19)$$

which can be combined to

$$k_{\perp m}^{(\mathrm{II})} = \frac{m\pi}{a} \qquad m \in \mathbb{N} \quad (20)$$

Therefore, the energy levels E_m are given by

$$E_m = \frac{1}{2}\left[\left(\frac{m\pi}{a}\right)^2 + \mathbf{k}_\parallel^2\right] \qquad m \in \mathbb{N} \quad (21)$$

The lowest energy level is for an even-parity state, and levels of even and odd states alternate. Because the Hamiltonian is invariant under time reversal,[7] both Ψ and Ψ^* are solutions of the Schrödinger equation (8) to the same energy.[8] This is expressed by the fact that both $\mathbf{k}$ and $-\mathbf{k}$ lead to the same energy, or, more specifically, $E_m = E_{-m}$. Therefore, it is sufficient to consider only positive wave numbers $k_{\perp m}^{(\mathrm{II})}$.

In comparison to the case of free electrons, that is, $V(\mathbf{r}) = 0$ for all $\mathbf{r}$, with energy band $E = \mathbf{k}^2/2$, the energy of the electrons confined to the well is quantized. In other words: the spectrum E_m is discrete, as is shown in Figure 4. The electronic states Ψ_m are called quantum-well states (QWSs) and have even (odd) parity for even (odd) m.

If one identifies the width a of the quantum well with a certain number N of layers with thickness d, $a = Nd$, the energy levels are given by

$$E_m(N) = \frac{1}{2}\left[\left(\frac{m\pi}{Nd}\right)^2 + \mathbf{k}_\parallel^2\right] \qquad m \in \mathbb{N} \quad (22)$$

These are shown in Figure 5. Connecting energy levels with identical quantum number m gives the typical $1/N^2$ behav-

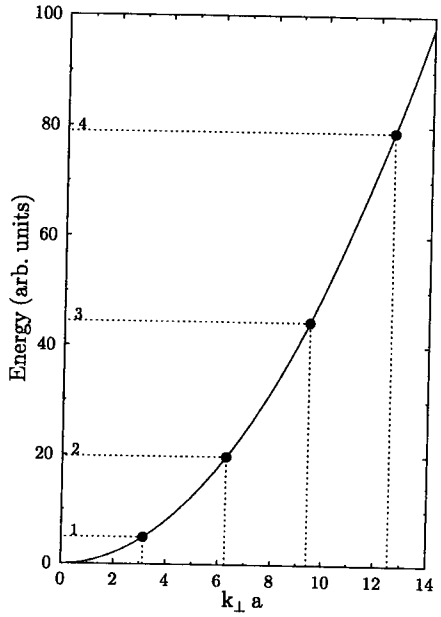

Fig. 4. Quantization of energy levels of an electron confined to a quantum well with infinitely high barriers ($U = \infty$). The solid line is the parabolic free-electron band, $E = k_\perp^2/2$. Filled circles represent the discrete spectrum of the confined electron. The allowed wave numbers $k_{\perp m} = m\pi/a$ are equidistant, cf. Eq. (20), and marked by dotted lines. The quantum number m is given at the left. The width of the well is a.

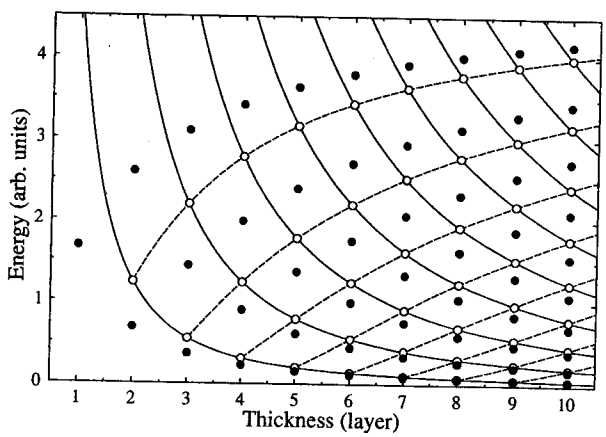

Fig. 5. Energy levels of an electron confined to a quantum well versus well thickness a. The latter is given in layers, $a = Nd$, d being the interlayer distance. Empty circles indicate energy levels for a well with infinitely high barriers. Solid lines connect levels with the same quantum number m, cf. $E_m(N)$ in Eq. (22). Dashed lines, however, connect levels with identical $m - N$. Filled circles indicate energy levels for a well with finite barriers, $U = 4.5$ ($\beta = 1.5$).

[7] The nonrelativistic time-reversal operator is complex conjugation, K_0. Its relativistic counterpart reads $-i\sigma_y K_0$, σ_y being a Pauli matrix.

[8] This is called Kramer's degeneracy [17].

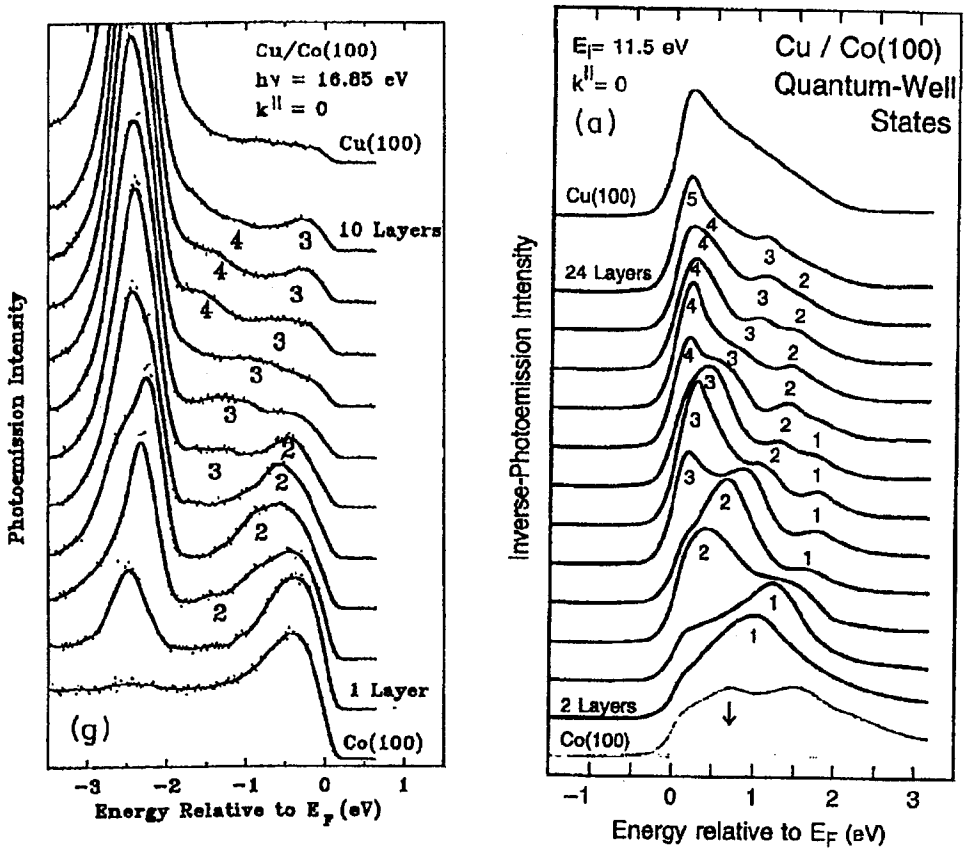

Fig. 6. Experimental photoelectron spectroscopy from quantum-well states of Cu films on fcc Co(100) for $\mathbf{k}_{\parallel} = 0$. Left: photoemission for 16.85 eV photon energy. The lowest spectrum shows the intensity for the uncovered substrate [fcc Co(100)], the uppermost that of semi-infinite Cu(100). Spectra for Cu film thicknesses from 1 layer up to 10 layers are shown in between. Intensity maxima that are related to quantum-well states are labeled by numbers. Right: inverse photoemission with 11.5 eV initial energy. The same quantum-well states as in the left panel are detected but above the Fermi energy E_F (cf. the numbers associated with the intensity maxima). Reprinted with permission from J. E. Ortega, F. J. Himpsel, G. J. Mankey, and R. F. Willis, *Phys. Rev. B* 47, 1540 (1993). Copyright 1993, by the American Physical Society.

ior (solid lines in Fig. 5). If levels with identical $m - N$ are connected (dashed lines in Fig. 5), one obtains a more tight-binding-like visualization, as we will see later.

We now return to the well with finite barriers. Defining $\xi = k_{\perp}^{(II)} a/2$, $\beta = a\sqrt{U/2}$, and $\eta = \cot\xi$, the matching conditions Eq. (18) can be written as

$$\eta = \frac{\xi}{\sqrt{\beta^2 - \xi^2}} \qquad \text{even parity} \qquad (23a)$$

$$-\eta = \frac{\sqrt{\beta^2 - \xi^2}}{\xi} \qquad \text{odd parity} \qquad (23b)$$

From this, one can extract that (i) all bound states are nondegenerate, (ii) even and odd solutions alternate with increasing energy, and (iii) the number of bound states is finite and equals $M + 1$ if $M\pi < 2\beta \leq (M + 1)\pi$. The first two statements have already been observed for the case of infinitely high barriers ($U \to \infty$, $\beta \to \infty$). Note that the well is sufficiently characterized by the dimensionless parameter β.

The energy levels for a well with finite β (finite height) are shown in Figure 5 as filled circles. For the parameters chosen, the number of states is equal to the number of layers. The global behavior in dependence on the film thickness is close to that for a well with $\beta = \infty$.

The preceding dispersion relations $E_m(N)$ for the QWSs can be experimentally determined by ARPES and angle-resolved inverse photoelectron spectroscopy (ARIPES); see Section 4. As a prototypical example, we address Cu films grown on face-centered cubic (fcc) Co(100). The photoelectron spectra taken for emission normal to the surface (i.e., $\mathbf{k}_{\parallel} = 0$) are shown in Figure 6. The intensity maxima related to the QWSs are labelled by the quantum numbers m (ARPES has access to the initial states below the Fermi energy E_F, whereas ARIPES probes states above E_F). The energy dispersion $E_m(N)$ as obtained from the spectra is shown in Figure 7. The dependence of the energy position on film thickness follows the theoretically determined one in very good agreement (lines in Fig. 7). These lines correspond to those for $m - N$ as obtained for the simple "rectangular-well" model (dashed lines in Fig. 5). Note that the bulk-band structure of Cu, in particular, the *sp* valence band, plays the same role as the free-electron band in the preceding quantum-well model (cf. Figs. 4 and 5).

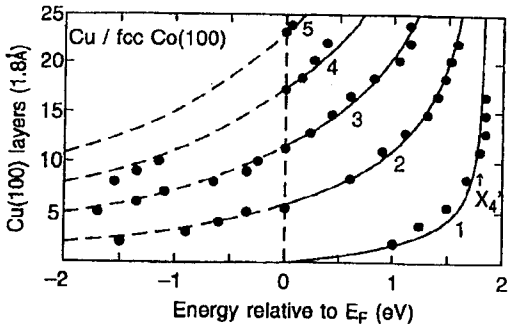

Fig. 7. Quantum-well states of Cu films on fcc Co(100) as obtained by angle-resolved photoelectron spectroscopy for $\mathbf{k}_\parallel = 0$. Shown are energy positions of quantum-well states versus film thickness—as obtained from the spectra in Figure 6 (filled circles). Lines are theoretically predicted values using the bulk-band structure of Cu along the Γ–Δ–X direction (cf. also Fig. 5). Reprinted with permission from J. E. Ortega, F. J. Himpsel, G. J. Mankey, and R. F. Willis, *Phys. Rev. B* 47, 1540 (1993). Copyright 1993, by the American Physical Society.

In the basic theory discussed previously, we assumed a symmetric quantum well, $V(\varrho, z) = V(\varrho, -z)$, thus ignoring any effects of the substrate that would affect the potential of the film at the film–substrate interface. It is straightforward to enhance the model to a different barrier height at the film–substrate boundary with respect to that at the vacuum–film boundary. Further, one can introduce additional potential steps in order to mimic polarization effects due to the substrate.

2.2.2. *Envelope Picture of Quantum-Well States*

In the preceding section, we employed a description of quantum-well states based on plane waves; for example, we assumed free electrons in the three regions of the system and neglected any "internal structure" of the potential in the film region. Now we take into account the crystal potential in an approximation, which was originally introduced for semiconductor superlattices [18, 19].

We start with the Schrödinger equation (8) for the infinitely extended system, the so-called bulk system, where $V(\mathbf{r})$ is now the potential of the bulk. The latter can be written as a sum over site, potentials $V(\mathbf{r}) = \sum_i V(\mathbf{r} - \mathbf{R}_i)$, where the vectors $\mathbf{R}_i$ form a lattice; that is they can be expressed in terms of basic translation vectors $\mathbf{a}_j$, $j = 1, 2, 3$: $\mathbf{R}_i = \sum_{j=1}^{3} n_{ij}\mathbf{a}_j$, $n_{ij} \in \mathbb{Z}$ (cf. Section 2.1.1). Therefore, the crystal potential is translationally invariant with respect to lattice vectors $\mathbf{R}$, $V(\mathbf{r}) = V(\mathbf{r}+\mathbf{R})$. Following the argumentation in Section 2.2.1 [Floquet's theorem; cf. also Eq. (7)], the wave functions fulfill the Bloch condition

$$\Psi(\mathbf{r} + \mathbf{R}; \mathbf{k}) = \exp(i\mathbf{k} \cdot \mathbf{R})\Psi(\mathbf{r}; \mathbf{k}) \tag{24}$$

Because the wave functions have to be square integrable, the wave vector $\mathbf{k}$ has to be real. These wave functions are called Bloch states and can be classified with respect to $\mathbf{k}$. Their energy eigenvalues, the bulk-band structure, are denoted $E(\mathbf{k})$.

The electrons have to be confined to the film, which is again considered as infinitely extended in the xy plane. We therefore introduce two boundaries, the vacuum–film interface (i) and the film–substrate interface (s). The interfaces are assumed only to change the boundary conditions with respect to the bulk case but to leave the potential in the film region unaltered; that is, effects due to the substrate or the vacuum region are ignored. Therefore, the effect of the interfaces on the wave functions can be described by reflectivities R_s and R_i as well as phase shifts ϕ_i and ϕ_s ($R_s, R_i, \phi_s, \phi_i \in \mathbb{R}$). For $\mathbf{k}_\parallel = 0$, fixed ϱ, and a film of thickness Nd (d being the interlayer distance), a 'round trip' of a Bloch wave in the film region yields a total interference factor of

$$I = R_s R_i \exp\left[i(2k_\perp Nd + \phi_s + \phi_i)\right] \tag{25}$$

Assuming complete reflection at the interfaces, $R_s R_i = 1$, constructive interference requires that the exponential factor in the preceding equation be equal unity. Or, equivalently,

$$2k_\perp Nd + \phi_s + \phi_i = 2n\pi \qquad n \in \mathbb{Z} \tag{26}$$

Introducing $\phi = \phi_s + \phi_i$, one arrives at the condition

$$k_\perp = \frac{2n\pi - \phi}{2Nd} \qquad n \in \mathbb{Z} \tag{27}$$

In conclusion, the boundary conditions at the interface restrict the allowed values of $k_\perp$ to those compatible with the "round-trip" criterion. The energies of the QWSs are therefore given by $E(k_\perp)$ with $k_\perp$ from Eq. (27). For a rectangular well with infinitely high barriers, the phase shift ϕ is either 0 (odd parity, $\phi_s = \phi_i = 0$) or 2π (even parity, $\phi_s = \phi_i = \pi$), which immediately yields Eq. (22).

The preceding $k_\perp$ quantization allows for an accurate determination of the bulk-band structure $E(k_\perp)$ by ARPES [20–22]. For fixed $\mathbf{k}_\parallel$, one measures photoemission intensities for films with different numbers of layers N and thus determines $E(k_\perp)$. For semi-infinite systems, this method does not work because there is no restriction for $k_\perp$; that is, it is not conserved in the photoemission process and therefore remains unknown.

Now consider a Bloch state with energy $E(k_\perp)$ in the range of a bulk band. Its wave function can be written as

$$\Psi(z; k_\perp) = \exp(ik_\perp z)u(z) \tag{28}$$

where $u(z)$ is periodic with the interlayer distance, $u(z + d) = u(d)$, which follows immediately, from Eq. (24). We now assume that $k_\perp$ takes a value $k_\perp^{\text{edge}}$ close to a band edge; for example, $k_\perp^{\text{edge}} = 0$ or π/d. A wave function at another energy than the bulk-band edge but within the bulk-band range, and therefore $k_\perp \neq k_\perp^{\text{edge}}$, can be approximated by

$$\Psi(z; k_\perp) \sim F(z)\Psi\left(z; k_\perp^{\text{edge}}\right) \tag{29}$$

where $F(z)$ is slowly varying: The wave function Ψ is given by $\Psi(k_\perp^{\text{edge}})$ but modulated by the envelope $F(z)$. According to the previous consideration on interference within a film, the envelope is given by $\exp(ik_\perp^{\text{env}}z)$. Thus, the total wave number $k_\perp$ reads $k_\perp = k_\perp^{\text{env}} + k_\perp^{\text{edge}}$. Note that, a Bloch state with $k_\perp^{\text{edge}}$ can occur as QWS if it fulfills the boundary conditions, that is, $k_\perp^{\text{edge}} = k_\perp$. In this case, $F(z) = 1$. Further, the envelope

accounts for the correct boundary condition at the interfaces and obviously, according to Eq. (27), $k_\perp^{\text{env}}$ depends on the phase shift ϕ. If $k_\perp^{\text{edge}}$ is given by π/d, we have

$$k_\perp^{\text{env}} = \frac{2(n-N)\pi - \phi}{2Nd} \qquad n \in \mathbb{Z} \tag{30}$$

It is worth noting again that the microscopic details at the interfaces are "smeared out" in the preceding envelope approximation. Therefore, it should be applied only in cases of thick films in which there is a bulklike potential of considerable spatial extent. In very thin films, for example, those in which the interfaces are very close, the previous approximation becomes questionable.

2.2.3. *Tight-Binding Description of Quantum-Well States: Rare-Gas Films on a Metallic Substrate*

We now address a description of quantum-well states based on the envelope theory. This model has been introduced by Grüne and co-workers in order to describe photoemission experiments of rare-gas films on metallic substrates [22]. Due to the inert behavior of the rare gases, bulk- as well as surface-band structures can be described very well within tight-binding theory. For example, the Xe $5p$ states are split due to spin-orbit coupling (SOC) into $5p_{j=1/2}$ and $5p_{j=3/2}$ states, j denoting the total angular momentum. In layered structures (as well as in the bulk of fcc-Xe), the $5p_{j=3/2}$ states are further split due to lateral interactions, for example, the overlap of orbitals located at different Xe sites [23–25]. Tight-binding models have proven to reproduce the experimentally determined energy dispersions very well [26, 27].

The main problem in describing the energy dispersion of Xe states on a metal substrate measured by means of ARPES is to account for the change in the Xe binding energy in dependence on the amount of adsorbed Xe. In particular, the binding energies of states located at the Xe–metal interface are substantially smaller than those of states in the other Xe layers. This behavior can be attributed either to a change in the work function,[9] which is due to the adsorption of Xe, or to the image force acting on the hole, which has been created in the photoemission process (cf. Section 4). The first effect is a so-called initial-state effect because it is present in the ground state of the system. The second is a final-state effect because it occurs in the excited system, that is, in the state with the photoelectron missing. To account for these effects, the simple rectangular well has to be extended as shown in Figure 8. Instead of three regions (I, II, and III), we now have four (A, B, C, and D). In the initial-state model, the change of the work function is V_B, which is known from experiment. The Fermi energy E_F is fixed by the substrate. The binding energies are $E = V_D + V_B - \Phi_M - E_F$ and $E = V_D + \Phi_M - E_F$ in the initial-state and the final-state model, respectively.

[9]The work function is the energy difference between the vacuum level and the Fermi level.

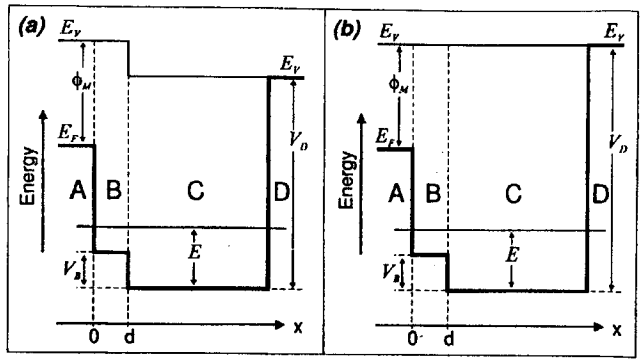

Fig. 8. Quantum-well models for rare-gas films on a metallic substrate (left, initial-state model; right, final-state model). E is the electron energy and Φ_M the work function of the substrate (no film present). The four regions A, B, C, and D are the substrate, the rare-gas layer next to the substrate, the remaining rare-gas layers, and the vacuum, respectively. Reprinted with permission from M. Grüne, T. Pelzer, K. Wandelt, and I. T. Steinberger, *J. Electron Spectrosc. Relat. Phenom.* 98–99, 121 (1999). Copyright 1999, by Elsevier Science.

Due to the confinement of the electrons to the Xe film, one assumes exponentially decaying plane waves in regions A (substrate) and D (vacuum) with constants κ_A and κ_D [cf. Eq. (16)]. The latter are given by

$$\kappa_A = \sqrt{2(V_D + V_B - \Phi_M - E)} \tag{31a}$$

$$\kappa_D = \sqrt{2(V_D - E)} \tag{31b}$$

in the initial-state model, which we focus on in the following discussion. In region C, the Xe film, one writes the wave function according to the envelope theory as

$$\Psi_C(z) = C \sin(k_C z + \delta_C) u(z) \tag{32}$$

where $\sin(k_C z + \delta_C)$ is the envelope and $u(z)$ is periodic with respect to the interlayer spacing d: $u(z) = u(z + d)$. One further assumes that u is symmetric with respect to the Xe layers, $\partial_z u(z) = 0$ at $z = nd$, $n = 0, \ldots, N$, where N is the number of Xe layers. In region B, the wave function takes the same form as in Eq. (32) but with labels B. Note that $u(z)$ need not be explicitly specified. The band structure $E(k)$ of bulk Xe is approximated by

$$E(k_B) = -\gamma_B\left[1 + \cos(k_B d)\right] + V_B - 2(\gamma_B - \gamma_C) \tag{33a}$$

$$E(k_C) = -\gamma_C\left[1 + \cos(k_C d)\right] \tag{33b}$$

that is, one uses the energy dispersion of a simple tight-binding model. Note that γ_B and γ_C are allowed to differ. As in the case of a rectangular quantum well, the dispersion relation is obtained via matching the wave functions at the interfaces. This yields the transcendental equation

$$k_C \tan\left[k_B d + \arctan(k_B/\kappa_A)\right] = -k_B \tan\left[(N-1)k_C d + \arctan(k_C/\kappa_D)\right] \tag{34}$$

which is used to determine the energies of the QWSs. After eliminating κ_A, κ_D, and k_B, one eventually obtains an equation in k_C with adjustable parameters γ_B, γ_C, and V_D that have to be determined by comparing the experimental QWS energies with

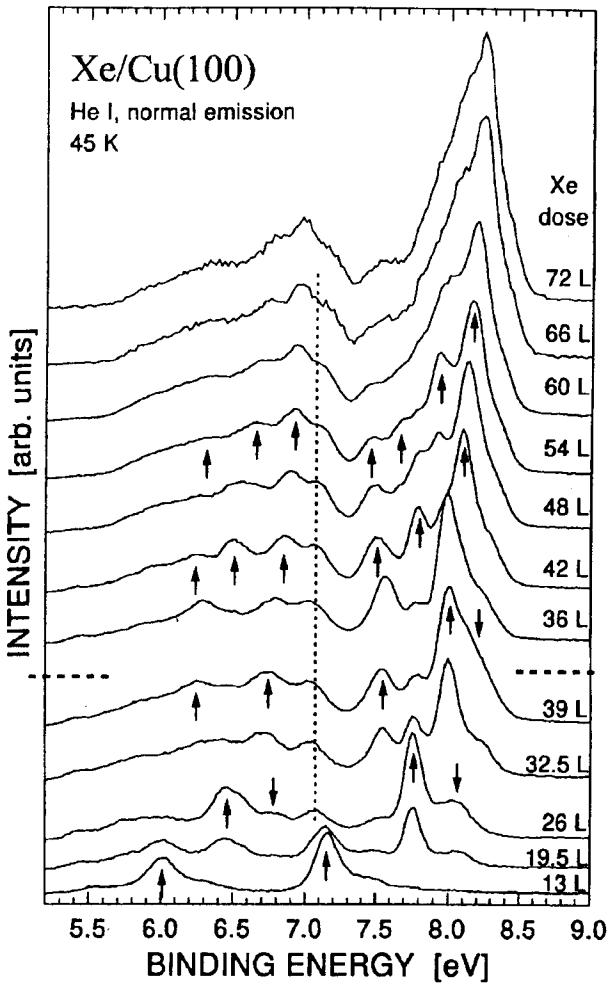

Fig. 9. Experimental photoelectron spectroscopy from Xe films on Cu(100) in normal emission ($\mathbf{k}_\parallel = 0$) and unpolarized light with 21.22 eV photon energy He(I). The Xe dose in langmuirs (L) is denoted on the right of each spectrum. Arrows indicate intensity maxima attributed to spin-orbit split $5p_{j=1/2}$ and $5p_{j=3/2}$ quantum-well states. Reprinted with permission from M. Grüne, T. Pelzer, K. Wandelt, and I. T. Steinberger, *J. Electron Spectrosc. Relat. Phenom.* 98–99, 121 (1999). Copyright 1999, by Elsevier Science.

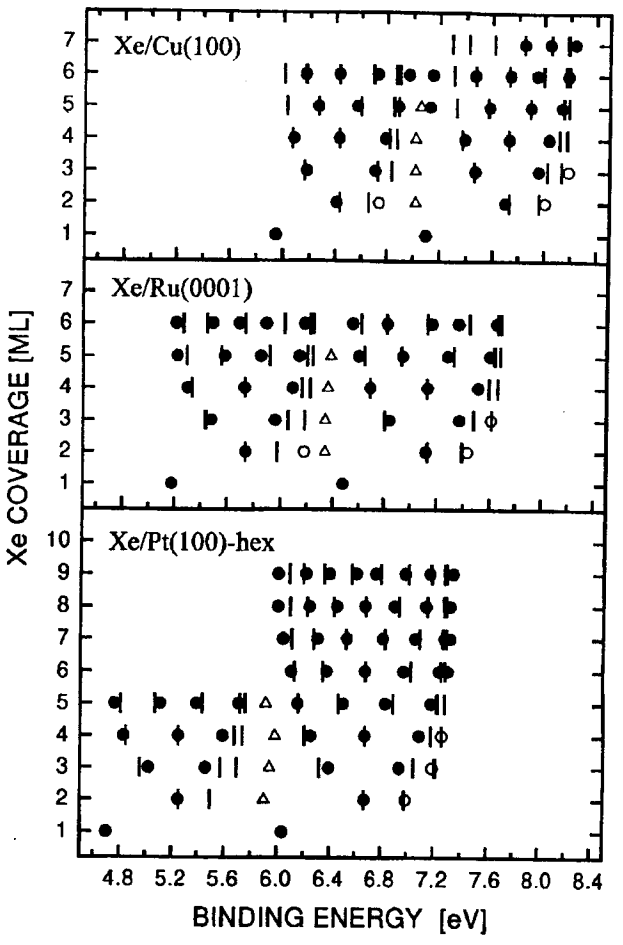

Fig. 10. Energies of quantum-well states of Xe films on metallic substrates [from bottom to top, Xe/Pt(100), Xe/Ru(0001), and Xe/Cu(100)]. Circles and triangles indicate experimentally determined values [for Xe/Cu(100), cf. Fig. 9]. Vertical lines mark values obtained from the theory of Section 2.2.3. Reprinted with permission from M. Grüne, T. Pelzer, K. Wandelt, and I. T. Steinberger, *J. Electron Spectrosc. Relat. Phenom.* 98–99, 121 (1999). Copyright 1999, by Elsevier Science.

that obtained by theory for all film thicknesses. Note that the adjustable parameters do not depend on the number of layers N.

The experimental photoelectron spectra for Xe films on Cu(100) are shown in Figure 9. For very low Xe coverage (cf. the lowest spectrum), one observes two Xe-derived maxima with binding energies that differ considerably from those at higher coverages. This can be attributed to the different potentials in regions B and C. At higher Xe coverages, the number of QWSs increases, as can be seen in Figure 10. For all three substrates, the pattern of energy positions is similar except for the specific binding energies. Each pattern can be divided into two groups, one for the $5p_{j=1/2}$ states, the other for the $5p_{j=3/2}$ states. This separation accomplishes the fitting procedure because each group can be fitted separately. For film thicknesses $N \geq 2$, each pattern is almost symmetric in energy, which can be attributed to the underlying tight-binding band-structure of Xe, Eq. (33) (see also Section 4.2.4). However, distinct deviations from the symmetry occur: Open circles in Figure 10 denote so-called extra peaks. For a film N layers thick, $N - 1$ energy positions follow closely that of a quantum well with infinitely high barriers and tight-binding band structure [cf. Eq. (27)]. The behavior of the Nth value can also be attributed to the potential difference between regions B and C. In conclusion, the sophisticated quantum-well model presented before is able to reproduce and to explain most, if not all, of the features found in experiment. Finally, it should be noted that initial-state and final-state models yield almost identical QWS dispersions. Therefore, one cannot judge from the preceding analysis whether the effects appear in the ground state or in the final state.

3. LOW-ENERGY ELECTRON DIFFRACTION

3.1. Introduction and History

Scattering of electrons from solid surfaces is one of the paradigms of quantum physics. The pioneering experiments

were performed by Davisson and Germer [28, 29] on a Ni single crystal with (111) orientation and confirmed de Broglie's concept of the wave nature of particles [30–32], a concept at the very heart of quantum mechanics (wave-particle dualism). Already in these early works they recognized the potential of low-energy electron diffraction (LEED) as a tool for the determination of surface structures [33, 34] and applied it to gas-adsorbate layers on Ni(111) [35]. This success was only possible due to two important properties of LEED: surface sensitivity and interference.

The schematical setup of a LEED experiment is shown in Figure 11. A monoenergetic beam of electrons with kinetic energy E impinges on the sample. The reflected electron beams are detected and analyzed with respect to their direction and energy. Usually, one detects only elastically reflected electrons (for which the energy is conserved) and uses incidence normal to the surface. Therefore, set of LEED spectra—or $I(E)$ curves—represents the current I of each reflected beam versus the initial energy E. Note that the reflected intensities are roughly as large as 1/1000 of the incoming intensity.

Surface Sensitivity. In 1928, Davisson and Germer observed an attenuation of the electron-beam intensity with sample thickness [36]. Electrons in a LEED experiment have a typical kinetic energy in the range of 20 to 500 eV.[10] Due to the interaction of the incoming electron with the electrons in the sample, the former penetrates into the solid only a few angstroms. Typical penetration lengths taken from the "universal curve" (see, e.g., Fig. 12) range from 5 to 10 Å [38, 39]. Therefore, LEED spectra usually carry less information about the geometrical structure of the volume of the solid, that is, the bulk, than of the solid's surface region.

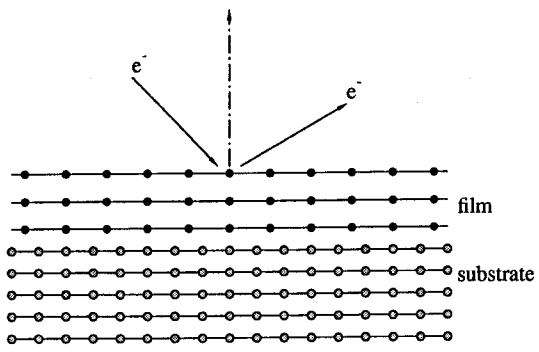

Fig. 11. Scheme of the LEED setup. An incoming beam of electrons e^- is elastically scattered by the solid. The latter is considered as a compound of the substrate (gray circles) and a thin film (black circles). A reflected electron beam is detected. The dashed–dotted arrow represents the surface normal.

[10]Experiments with energies below this range are called very low energy electron diffraction (VLEED), those with higher energies medium-energy electron diffraction (MEED). At even higher energies, one uses gracing electron incidence and emission to obtain surface sensitivity, that is, reflecting high-energy electron diffraction (RHEED).

Interference. De Broglie showed that a particle with momentum $\mathbf{p}$ can be associated with a wave with wavelength $\lambda = 2\pi/p$ ($p = |\mathbf{p}|$). For example, an electron in vacuum can be described by a plane wave

$$\Psi(\mathbf{r}, t) = \exp[i(\mathbf{k} \cdot \mathbf{r} - \omega t)] \tag{35}$$

with wave number $k = 2\pi/\lambda$ and energy $E = \omega = k^2/2$. De Broglie's picture of electrons as waves and the interpretation of the Davisson–Germer LEED experiments lead to the question: *Are electrons waves?* [40]. Comparison was made to X-ray scattering in view of the determination of structural information and Davisson came to the conclusion that if X-rays are waves then electrons are, too. However, he admitted that the picture of electrons as particles is better suited for the explanation of the Compton effect or the photoelectric effect (cf. Section 4 on angle-resolved photoelectron spectroscopy).

In the wave picture of electrons, the LEED experiment can be regarded as follows. An incoming plane wave, the incident beam, is scattered at each site and the outgoing plane waves, the outgoing beams, are measured. Both amplitude and phase of each outgoing wave are determined by the scattering properties and the position of each scatterer. For example, a change in the position of a scatterer will change the wave pattern in the solid and, therefore, will affect both amplitudes and phases of the outgoing waves. Because the LEED current of a beam is given by the wave amplitude, it carries information on both positions and scattering properties of the sites. This mechanism can be used, for instance, to obtain images of the geometrical structure in configuration space by LEED holography [41].

Although LEED is sensitive to the outermost region of the sample, it is capable of detecting fingerprints of the electronic states of the film–substrate system. As mentioned previously,

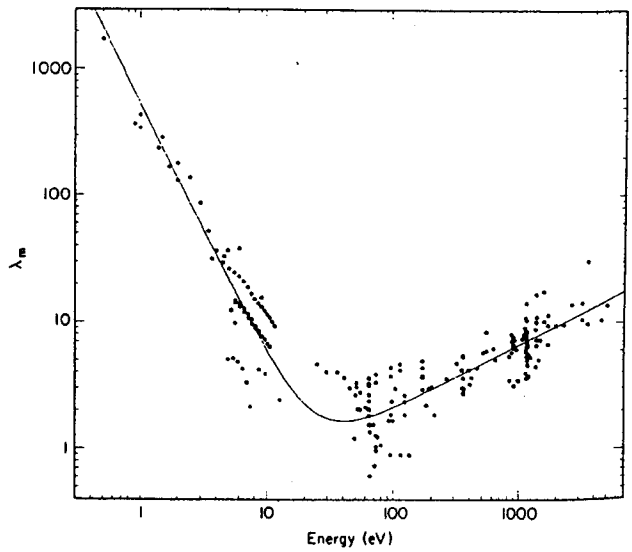

Fig. 12. Compilation for elements of the inelastic mean free path λ_m (dots) in monolayers as a function of energy above the Fermi level. This "universal curve" is almost independent of the solid, for example, surface orientation or elemental composition. The solid line serves as a guide to the eye. For details, see [37]. Reprinted with permission from M. P. Seah and W. A. Dench, *Surf. Interface Anal.* 1, 2 (1979). Copyright 1979, by John Wiley & Sons.

the LEED intensities depend on the electronic structure of the sample above the vacuum level and, therefore, contain information of the electronic structure of the entire film. In particular, quantized states that are confined to the film have a pronounced effect on the LEED spectra.

It took considerable time to develop theories that include multiple scattering of the LEED electron [42–44], which obviously is necessary for a proper description of LEED spectra. Textbooks that introduce to the field and present computer codes for the calculation of $I(E)$ spectra were written by Pendry [45] as well as van Hove et al. [46]. Van Hove and Tong also provide review articles [47, 48].

Additional information can be obtained if one uses a spin-polarized beam of incoming electrons, that is, spin-polarized low-energy electron diffraction (SPLEED), and uses a spin-sensitive detector, for example a Mott detector or a SPLEED detector. Interestingly, the latter exploits the LEED mechanism itself for a spin resolution in the experiment. Pioneering works were made by Feder [49–51] on the theoretical and by Kirschner [52] on the experimental side.

3.2. Theories

In the following, a theoretical description of LEED from semi-infinite solids covered by thin films (cf. Fig. 11) is presented. The kinematical theory focuses mainly on interference effects (Section 3.2.1), whereas in the pseudopotential theory a close connection of LEED intensities to the electronic structure is established (Section 3.2.2). The multiple-scattering theory gives an introduction to state-of-the-art calculations of LEED from layered systems (Section 3.2.3).

3.2.1. Kinematical Theory

According to de Broglie's wave picture of electrons, we consider as an introduction elastic scattering of a plane wave by a one-dimensional periodic structure (cf. Fig. 13). Constructive interference occurs if the phase difference between outgoing beams scattered from neighboring sites is an integer multiple of the wavelength λ,

$$a(\sin\varphi - \sin\varphi_0) = h\lambda \qquad h \in \mathbb{Z} \tag{36}$$

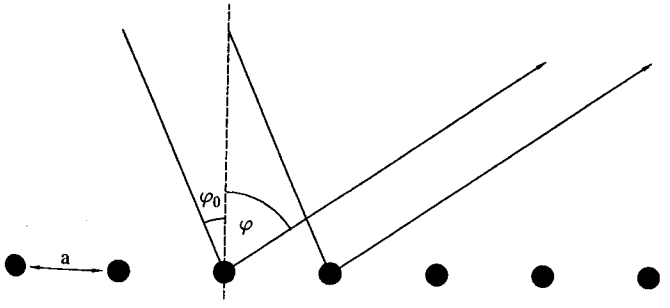

Fig. 13. Scattering from a one-dimensional periodic structure with lattice constant a. The incoming plane wave impinges with a polar angle of φ_0 relative to the normal axis (dashed line). The diffracted wave is outgoing with an angle φ.

This is the so-called Laue condition, and h is the order of diffraction. Note that the hth order of diffraction corresponds to the nhth order of the same periodic structure but with lattice constant na.

The preceding consideration can easily be applied to two-dimensional periodic structures, that is, a two-dimensional lattice with basis vectors $\mathbf{a}_1$ and $\mathbf{a}_2$; cf. Section 2.1.1. The Laue condition then reads

$$\sin\varphi - \sin\varphi_0 = \lambda/d_{hk} \tag{37}$$

with $d_{hk} = |h\mathbf{a}_1 + k\mathbf{a}_2|$ denoting the length of a vector of the direct (covariant) lattice. In other words, the diffraction pattern, that is, the set of angles φ and φ_0 for which there is constructive interference, yields the geometry of the direct lattice. h and k are referred to as the Miller indices. The Laue conditions can further be written as

$$(\mathbf{s} - \mathbf{s}_0)\cdot\mathbf{a}_i = h_i\lambda \qquad i = 1, 2,\ h_i \in \mathbb{Z} \tag{38}$$

where the vectors $\mathbf{s}$ and $\mathbf{s}_0$ specify the directions of the incoming beam and the diffracted beams, respectively. Expanding $\Delta\mathbf{s} = \mathbf{s} - \mathbf{s}_0$ in the basis of the reciprocal lattice, $\Delta\mathbf{s} = \mathbf{g}_1\zeta_1 + \mathbf{g}_2\zeta_2$, one sees immediately that $\Delta\mathbf{s} = (\mathbf{g}_1h_1 + \mathbf{g}_2h_2)\lambda$. Or, in other words, the diffraction pattern is directly a representation of the reciprocal (contravariant) lattice. Because the Laue conditions pick out discrete directions of reflection, each of which is associated with a pair of Miller indices (h, k), one usually calls the reflected wave functions LEED beams and indicates them by (h, k). The results obtained so far can be cast into the sketch of a LEED experiment as shown in Figure 14.

Up to now, only the diffraction pattern has been considered; intensities of the diffracted beams have been ignored. A first approach for calculating intensities is the kinematical theory,

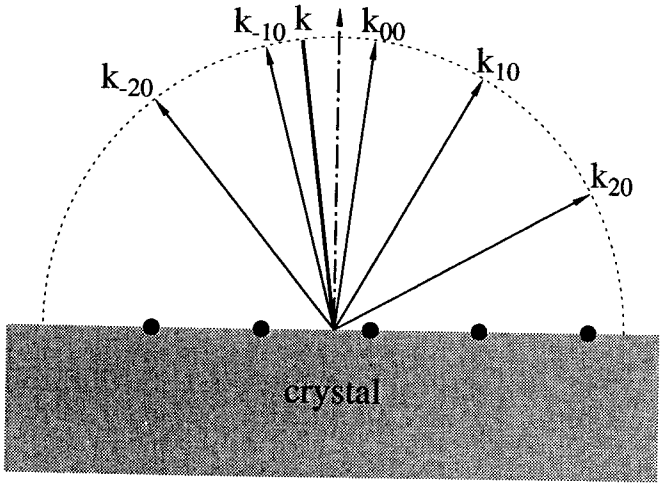

Fig. 14. Scheme of a LEED experiment. An incoming beam of electrons specified by its wave vector $\mathbf{k}$ (incoming arrow) is scattered by the solid (gray area). The elastically reflected electron beams are indicated by their Miller indices h and k of the surface-reciprocal lattice vectors, their wave vector denoted as $\mathbf{k}_{hk}$ (outgoing arrows). Filled circles represent atoms at the surface. The surface normal is given by the dashed–dotted arrow. Because the electrons are reflected elastically, the lengths of the individual wave vectors are identical (cf. the dotted semicircle).

which assumes that the interaction of the LEED electron with the solid is weak. Therefore, only single-scattering events have to be considered; multiple scattering is neglected. This approximation gives reasonable results for scattering of X-rays and fast electrons (e.g., for Compton profiles), but worse results for slow electrons (e.g., for LEED or VLEED). However, the basic idea can be regarded as the starting point for a dynamical theory, that is, a theory that takes into account multiple scattering.

Consider a LEED experiment from a semi-infinite solid that consists of a substrate covered by a thin film (cf. Fig. 11). The incoming LEED beam with incidence direction $\mathbf{s}_0$ is represented by the plane wave $\Psi_{\text{inc}} = \Psi_0 \exp(i\mathbf{k}_0 \cdot \mathbf{r})$, where the momentum $\mathbf{k}_0 = 2\pi\mathbf{s}_0/\lambda$. An outgoing wave scattered from site $\mathbf{R}'$ and detected at $\mathbf{R}$ is given by

$$\Psi_{\mathbf{R}'} = \underbrace{\Psi_0 \frac{\exp(i\mathbf{k}\cdot\mathbf{R})}{R}}_{1} \underbrace{f(\mathbf{k}, \mathbf{k}_0; \mathbf{R}')}_{2} \underbrace{\exp\left[i(\mathbf{k}-\mathbf{k}_0)\cdot\mathbf{R}'\right]}_{3} \quad (39)$$

The first term [denoted 1 in Eq. (39)] is a spherical wave; the second is the atomic structure factor and describes scattering of plane waves at site $\mathbf{R}'$. In a dynamical theory, it depends on both directions $\mathbf{k}$ and $\mathbf{k}_0$, whereas in the kinematical theory it is assumed to depend only on $\mathbf{k}-\mathbf{k}_0$: $f(\mathbf{k}, \mathbf{k}_0; \mathbf{R}') = f(\mathbf{k}-\mathbf{k}_0; \mathbf{R}')$. The third term takes care of the phase difference relative to the origin of the coordinate system. Note that the detector is assumed to be positioned at a large distance away from the sample. Therefore, the spherical waves outgoing from each scatterer can be replaced in good approximation by plane waves at the detector position.

Because only single scattering is considered, the total outgoing wave function is the sum of those outgoing from the substrate and those from the film, $\Psi_{\text{out}} = \Psi_{\text{out}}^{\text{sub}} + \Psi_{\text{out}}^{\text{film}}$. We first consider the substrate, the lattice of which is defined by the basis vectors $\mathbf{a}_1$, $\mathbf{a}_2$, and $\mathbf{a}_3$. The first two are parallel to the surface ($a_{1z} = a_{2z} = 0$), and the latter points from one layer to the neighboring one ($a_{3z} \neq 0$; $\mathbf{a}_3$ corresponds to the interlayer vector $\mathbf{d}$ introduced previously). Further, the structure factor is assumed as identical for all sites: $f^{\text{sub}}(\mathbf{k}-\mathbf{k}_0; \mathbf{R}') = f^{\text{sub}}(\mathbf{k}-\mathbf{k}_0)$. The outgoing wave then reads

$$\Psi_{\text{out}}^{\text{sub}} \sim f^{\text{sub}}(\mathbf{k}-\mathbf{k}_0) \sum_{n_1 n_2 n_3} \exp\left[i(\mathbf{k}-\mathbf{k}_0)\cdot(n_1\mathbf{a}_1+n_2\mathbf{a}_2+n_3\mathbf{a}_3)\right] \quad (40)$$

and is the product of a single-site structure factor (f^{sub}) and a geometrical part that depends only on the lattice structure. This feature—the separation of scattering properties and the geometrical arrangement of the scatterers—is also present in the Korringa–Kohn–Rostoker (KKR) multiple-scattering approach presented in Section 3.2.3. With the definitions

$$S_i^{\text{sub}}(\mathbf{k}-\mathbf{k}_0) = \sum_{n_i} \exp\left[in_i(\mathbf{k}-\mathbf{k}_0)\cdot\mathbf{a}_i\right] \qquad i = 1, 2, 3 \quad (41)$$

the intensity I^{sub} at the detector position $\mathbf{R}$ solely from the substrate reads

$$I^{\text{sub}} \sim |\Psi_{\text{out}}^{\text{sub}}|^2 \sim \left|f^{\text{sub}}(\mathbf{k}-\mathbf{k}_0)\right|^2 \prod_{i=1}^{3} \left|S_i^{\text{sub}}(\mathbf{k}-\mathbf{k}_0)\right|^2 \quad (42)$$

One now has to consider the sums S_i^{sub}, $i = 1, 2, 3$. As Davisson and Germer observed [36], the electron beams are attenuated in a direction normal to the surface. Thus, an empirical attenuation factor μ is introduced, which takes care of the surface sensitivity of the LEED experiment (see Fig 12). Then S_3^{sub} reads

$$S_3^{\text{sub}}(\mathbf{k}-\mathbf{k}_0) = \sum_{j=0}^{\infty} \exp\left[ij(\mathbf{k}-\mathbf{k}_0)\cdot\mathbf{a}_3 - j\mu\right] \quad (43)$$

Summing up the geometrical series yields

$$\left|S_3^{\text{sub}}(\mathbf{k}-\mathbf{k}_0)\right|^2 = \Big\{1 - 2\exp(-\mu)\cos\left[(\mathbf{k}-\mathbf{k}_0)\cdot\mathbf{a}_3\right] + \exp(-2\mu)\Big\}^{-1} \quad (44)$$

which is maximal if $\cos[(\mathbf{k}-\mathbf{k}_0)\cdot\mathbf{a}_3] = 1$ or, equivalently, if $(\mathbf{k}-\mathbf{k}_0)\cdot\mathbf{a}_3 = 2\pi h_3$ with integer h_3. This establishes the third Laue condition; cf. Eq. (38). Analogously, the sums S_1 and S_2 give the two Laue conditions for planar diffraction.

The effect of the attenuation on the third Laue condition is shown in Figure 15a, where $|S_3(\mathbf{k}-\mathbf{k}_0)|^2$ is presented for several values of μ. An increase of the latter reduces the ratio of the maxima at $2\pi h_3$ to the minima at πh_3. In other words, strong attenuation weakens the third Laue condition.

Now we consider the effect of the film on the electron diffraction. For a film with N_3 layers, the outgoing wave func-

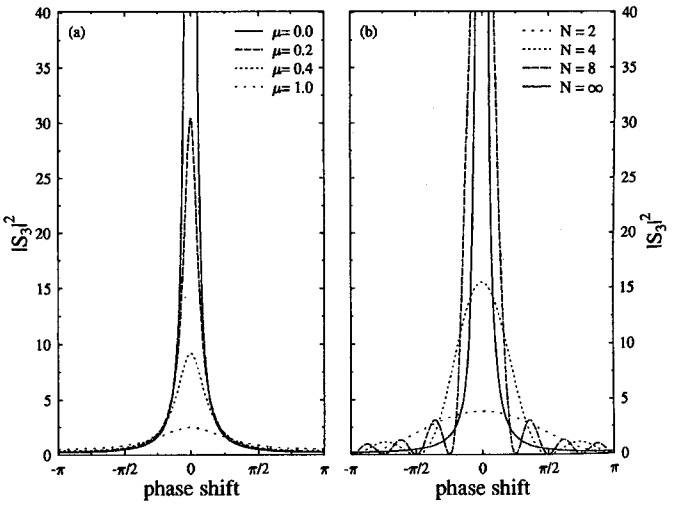

Fig. 15. Weakening of Laue conditions. (a) Effect of attenuation on the Laue condition. The lattice factor $|S_3|^2$, cf. Eq. (44), is shown for attenuation factors $\mu = 0.0$, 0.2, 0.4, and 1.0 versus the phase shift $(\mathbf{k}-\mathbf{k}_0)\cdot\mathbf{a}_3$. The lattice factor is maximal at multiples of 2π, in accordance with the third Laue condition. An increase in μ leads to weakening of the latter. (b) Effect of a finite number of layers on the Laue condition. The lattice factor $|S_3|^2$, cf. Eq. (47), is shown for $N = 2$, 4, 8, and ∞ layers versus the phase shift $(\mathbf{k}-\mathbf{k}_0)\cdot\mathbf{b}_3$. The lattice factor is maximal at multiples of 2π, in accordance with the third Laue condition but additional maxima occur for finite N. A decrease in N leads to weakening of the Laue condition. The attenuation factor chosen is $\mu = 0.01$.

tion is

$$\Psi_{\text{out}}^{\text{film}} \sim f^{\text{film}}(\mathbf{k}-\mathbf{k}_0)\prod_{i=1}^{3} S_i^{\text{film}} \tag{45}$$

with the definition

$$S_i^{\text{film}}(\mathbf{k}-\mathbf{k}_0) = \sum_{n_i} \exp\left[i n_i (\mathbf{k}-\mathbf{k}_0)\cdot\mathbf{b}_i\right] \qquad i = 1,2,3 \tag{46}$$

The lattice factors S_1^{film} and S_2^{film} establish the first two Laue conditions for the film structure, $(\mathbf{k}-\mathbf{k}_0)\cdot\mathbf{b}_i = 2\pi h_i$, h_i integer. In S_3^{film}, one has to sum over the finite number N_3 of film layers, which yields

$$\left|S_3^{\text{film}}(\mathbf{k}-\mathbf{k}_0)\right|^2 = \frac{1-2\exp(-\mu N_3)\cos\left[N_3(\mathbf{k}-\mathbf{k}_0)\cdot\mathbf{b}_3\right]+\exp(-2\mu N_3)}{1-2\exp(-\mu)\cos\left[(\mathbf{k}-\mathbf{k}_0)\cdot\mathbf{b}_3\right]+\exp(-2\mu)} \tag{47}$$

Obviously, for $N_3 = 1$ there is no third Laue condition [$|S_3^{\text{film}}(\mathbf{k}-\mathbf{k}_0)|^2 = 1$] because there is no interference in the direction normal to the film. The effect of finite N_3 on $|S_3|^2$ is shown in Figure 15b. A large number of layers leads to sharp global maxima in the lattice factor (compare the cases $N_3 = 8$ and $N_3 = \infty$); however, $N_3 - 2$ additional maxima occur in $[0, 2\pi]$. A decrease of N_3 weakens the third Laue condition considerably (cf. the case $N_3 = 2$). In the LEED $I(E)$ spectra, this would lead to broad maxima of the "kinematical peaks".

Finally, consider the total intensity I^{tot} of the entire film–substrate system. Because the outgoing wave function is the sum of that arising from the substrate and that of the film, $\Psi_{\text{out}} = \Psi_{\text{out}}^{\text{sub}} + \Psi_{\text{out}}^{\text{film}}$, the intensity reads

$$I^{\text{tot}} \sim |\Psi_{\text{out}}^{\text{sub}} + \Psi_{\text{out}}^{\text{film}}|^2 \tag{48a}$$

$$\sim I^{\text{sub}} + I^{\text{film}} + 2\,\text{Re}\left[(\Psi_{\text{out}}^{\text{sub}})^* \Psi_{\text{out}}^{\text{film}}\right] \tag{48b}$$

The third term is due to interference of the electron's wave between the film and the substrate structure. Its effect on the LEED intensity is shown in Figure 16 for a film with $N_3 = 4$ layers and a simply related structure ($b_3 = 3a_3$; cf. panel a). Obviously, the total LEED intensity is not the sum of the film and substrate intensity, as is evident from the maxima at multiples of 2π. If the structures are incoherently related (panel b), the LEED intensity becomes irregular, in particular, that of the substrate-related maxima. In a polar plot (shown as insets in Fig. 16), a simply related structure shows n clubs if $\mathbf{b}_i = n\mathbf{a}_i$, which, for the case shown here, leads to three clubs. If the film and the substrate structure are incoherently related, that is, the ratio n is irrational, the pattern becomes dense in the polar plot. For $n = 2\sqrt{3} \sim 3.4641$, the substrate-related maxima at $2\pi n$ dominate (cf. the club aligned along the x axis in the upper right inset of Fig. 16).

The periodicity at the surface or in the film must not be identical to that of the substrate (cf. Section 2.1.1). But because the periodicity of the latter can easily be recognized in the LEED pattern, it is convenient to use it as the reference [cf. the matrix G in Eq. (5)]. A spot in the surface reciprocal net, which has integer indices n_1 and n_2, can be expressed in the substrate reciprocal net via $(m_1, m_2)G = (n_1, n_2)H$, which yields the indices $(m_1, m_2) = (n_1, n_2)M$.

If there are N scatterers in the unit cell located at τ_j, $j = 1, \ldots, N$, the kinematical structure factor is given by

$$F(\mathbf{k}-\mathbf{k}_0;\mathbf{R}) = \sum_{j=1}^{N} f_j(\mathbf{k}-\mathbf{k}_0;\mathbf{R})\exp\left[i(\mathbf{k}-\mathbf{k}_0)\cdot\tau_j\right] \tag{49}$$

Again, multiple scattering has been neglected, in contrast to a dynamical theory. Therefore, in order to treat several scatterers in the unit cell, one has to replace $f(\mathbf{k}-\mathbf{k}_0;\mathbf{R})$ by $F(\mathbf{k}-\mathbf{k}_0;\mathbf{R})$.

In the kinematical theory, the electronic structure of the sample enters via the atomic form factors, that is, more or less indirectly because these do not provide access to details of the electronic structure of both substrate and sample [e.g., band structure $E(\mathbf{k})$ and density of states (DOS)]. To illustrate the close connection between LEED intensities and electronic structure, we introduce a LEED theory based on empirical pseudopotentials.

3.2.2. *Pseudopotential Description of Low-Energy Electron Diffraction*

The following approach to LEED calculations is based on the considerations that (i) the scattering of the electrons inside the solid can be calculated with well-established band structure methods; (ii) the LEED state inside the sample is expanded into Bloch waves of the infinite solid, taking into account the correct boundary conditions in both the vacuum and the bulk; and (iii) lifetime effects can easily be incorporated via complex energies [53]. Employing the band structure of the solid can help to interpret LEED spectra or—the other way round—to determine the band structure by adjusting the potential parameters used in the calculations in such way that experimental and theoretical LEED, VLEED, or target-current spectra[11] come as close as possible. The latter band structure mapping has been proven to give good results for both metals and layered semiconductors [54] (for a short review, see [55]).

One approach for calculating LEED intensities is based on empirical local pseudopotentials. If the scattering of the electrons is weak, as can be expected because the band structure at typical LEED energies is more or less free-electron-like (cf. also the preceding kinematical treatment), the Coulomb part of the atomic potentials can be neglected, because it is screened by the core-level electrons. In the bulk of the solid, the potential is expanded in a Fourier series with a few reciprocal lattice vectors,

$$V(\mathbf{r}) = \sum_{\mathbf{G}} V_{\mathbf{G}} \exp(-i\mathbf{G}\cdot\mathbf{r}) \tag{50}$$

[11] Target-current spectroscopy (TCS) measures the current flowing through the sample that is due to the incident electron beam. It can therefore be regarded as complementary to LEED because in TCS the *transmitted* current is measured, whereas in LEED it is the *reflected* current.

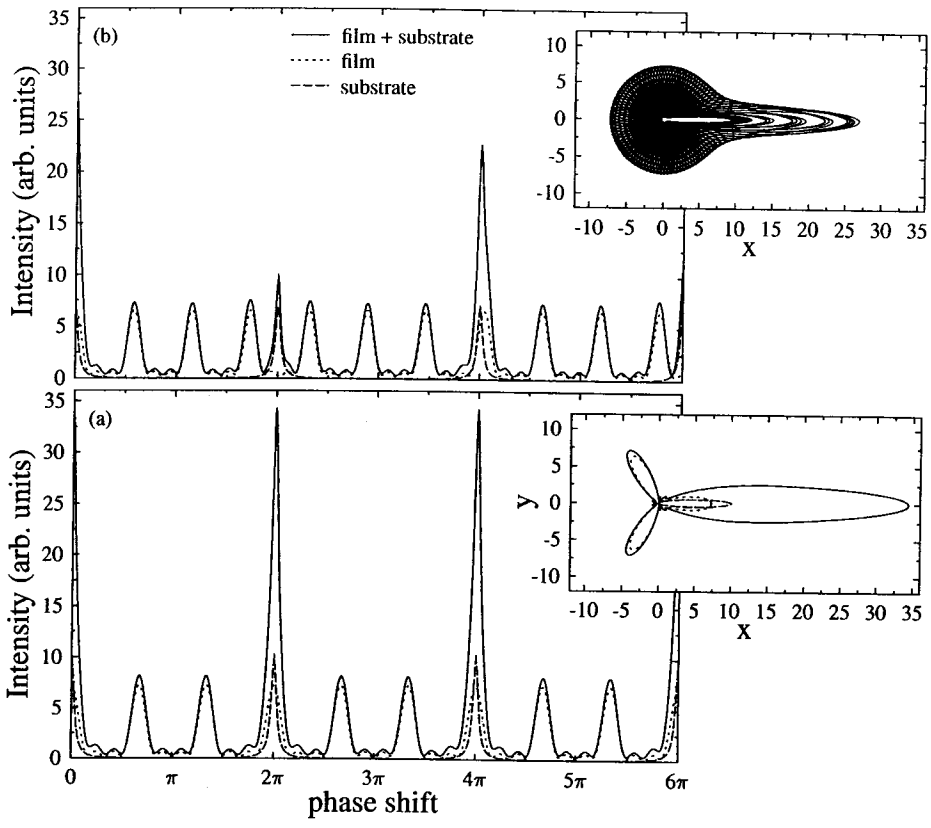

Fig. 16. Interference effect on the LEED intensity from a thin film with $N_3 = 4$ layers. (a) Simply related structure ($b_3 = 3a_3$) and (b) incoherent structure ($b_3 = 2\sqrt{3}a_3$). Shown are the total intensity (I^{tot}, solid line), the film intensity (I^{film}, dotted line), and the substrate intensity (I^{sub}, dashed line) versus the phase factor. Atomic form factors f^{film} and f^{sub} were chosen as identical. The attenuation factor is $\mu = 0.1$. The insets on the right show the same data as in (a) and (b) but as polar plots and within an extended range of the phase shift.

where $\mathbf{G}$ is a vector of the bulk reciprocal lattice. For a given wave vector $\mathbf{k}$, the wave function is also expanded in a Fourier series,

$$\Phi(\mathbf{r};\mathbf{k}) = \sum_{\mathbf{G}} \alpha_{\mathbf{G}}(\mathbf{k}) \exp\left[i(\mathbf{k}+\mathbf{G})\cdot\mathbf{r}\right] \tag{51}$$

Inserting $\Phi(\mathbf{r};\mathbf{k})$ and $V(\mathbf{r})$ into the Schrödinger equation, one arrives at the secular equation

$$\sum_{\mathbf{G}} \left\{ \left[(\mathbf{k}+\mathbf{G})^2 - 2E\right]\delta_{\mathbf{G}\mathbf{G}'} + 2V_{\mathbf{G}-\mathbf{G}'} \right\} \alpha_{\mathbf{G}}(\mathbf{k}) = 0 \quad \forall \mathbf{G}' \tag{52}$$

which can be solved numerically using standard eigenproblem routines. The preceding equation is not very well suited for LEED calculations, because in LEED one wants to know the bulk-band structure for given energy E and $\mathbf{k}_\parallel$. In other words, we do not want to compute $E(\mathbf{k}_\parallel, k_\perp)$ but $k_\perp(E, \mathbf{k}_\parallel)$. Rewriting Eq. (52) as

$$\left[(k_\perp + G'_\perp)^2 - 2E\right]\alpha_{\mathbf{G}'} + \sum_{\mathbf{G}} \left[2V_{\mathbf{G}-\mathbf{G}'} + (\mathbf{k}_\parallel + \mathbf{G}_\parallel)^2 \delta_{\mathbf{G}\mathbf{G}'}\right]\alpha_{\mathbf{G}'} = 0 \quad \forall \mathbf{G}' \tag{53}$$

and defining

$$A_{\mathbf{G}\mathbf{G}'} = \left(G_\perp - \sqrt{2E}\right)\delta_{\mathbf{G}\mathbf{G}'} \tag{54a}$$

$$B_{\mathbf{G}\mathbf{G}'} = \left(G_\perp + \sqrt{2E}\right)\delta_{\mathbf{G}\mathbf{G}'} \tag{54b}$$

$$C_{\mathbf{G}\mathbf{G}'} = \left(\mathbf{k}_\parallel + \mathbf{G}_\parallel\right)^2 \delta_{\mathbf{G}\mathbf{G}'} + 2V_{\mathbf{G}-\mathbf{G}'} \tag{54c}$$

one arrives at the matrix equation

$$\begin{pmatrix} -A & -C \\ 1 & -B \end{pmatrix} \begin{pmatrix} \alpha \\ \beta \end{pmatrix} = k_\perp \begin{pmatrix} \alpha \\ \beta \end{pmatrix} \tag{55}$$

Instead of an eigenvalue problem of a hermitian matrix, one eventually is dealing with one that is twice the size and non-hermitian. Therefore, the number of eigenfunctions and eigenvalues is twice the number of vectors $\mathbf{G}$ taken into account.

We now have to consider the boundary conditions. In the bulk, each eigenfunction fulfills Floquet's theorem,

$$\Psi^{(j)}(\mathbf{r}+\mathbf{R}) = \lambda^{(j)}(\mathbf{R})\Psi^{(j)}(\mathbf{r}) \quad \forall \mathbf{R} \tag{56}$$

where $\mathbf{R}$ is a translation vector of the bulk. Because we are interested in the band structure for given $\mathbf{k}_\parallel$, the proportionality factor $\lambda^{(j)}$ can conveniently be written as $\lambda^{(j)}(\mathbf{R}) = \exp(i(\mathbf{k}_\parallel \cdot \mathbf{R}_\parallel + k_\perp^{(j)} R_\perp))$ (cf. Section 2.2.1). And because the eigenvalue problem is no longer hermitian, $k_\perp$ can be complex

even for real energies E. This feature gave rise to Heine's concept of the complex band structure [56].

According to Chang [57], the bands associated with $k_\perp^{(j)}$ can be cast into the following categories:

Real bands correspond to the conventional band structure and have $\mathrm{Im}\, k_\perp^{(j)} = 0$. Thus, $|\lambda^{(j)}| = 1$ and the wave functions $\Psi^{(j)}$ are the Bloch states [13].

Imaginary bands of the first kind have $\mathrm{Re}\, k_\perp^{(j)} = 0$ and $\mathrm{Im}\, k_\perp^{(j)} \neq 0$.

Imaginary bands of the second kind have $\mathrm{Re}\, k_\perp^{(j)} = k_{\perp\max}$ and $\mathrm{Im}\, k_\perp^{(j)} \neq 0$.

Complex bands have $\mathrm{Re}\, k_\perp^{(j)} \neq 0$, $\mathrm{Re}\, k_\perp^{(j)} \neq k_{\perp\max}$, and $\mathrm{Im}\, k_\perp^{(j)} \neq 0$.

Here, $k_{\perp\max}$ refers to the boundary of the (first) Brillouin zone in the z direction. In the infinite solid, all wave functions $\Psi^{(j)}$ have to be square integrable ($\Psi^{(j)} \in \mathcal{L}_2$). That means only Bloch states are proper solutions of the Schrödinger equation. Due to the surface, the integration range can be taken as one half-space, say $z > 0$, and the set of proper wave functions can be extended to those the amplitude of which decays in direction toward the bulk. Thus, all imaginary and complex bands with $\mathrm{Im}\, k_\perp^{(j)} < 0$ have to be considered in addition to the real bands. The wave functions associated with these bands are usually called evanescent states.

The next step is to construct the wave function of the LEED electron, the LEED state. In the vacuum, which is characterized by the fact that the potential is, the incoming beam is represented by an incoming plane wave with surface-parallel wave vector

$$\mathbf{k}_\parallel = \sqrt{2E}\sin\vartheta_e \begin{pmatrix} \cos\varphi_e \\ \sin\varphi_e \end{pmatrix} \tag{57}$$

where E is the kinetic energy of the incident electron. ϑ_e and φ_e are the polar and the azimuthal angles of electron incidence, respectively. The wave function in the vacuum thus reads

$$\Phi(\mathbf{k}_\parallel; E) = \underbrace{\exp\left[i(\mathbf{k}_\parallel \cdot \varrho + \kappa_0 z)\right]}_{\text{incoming}} + \underbrace{\sum_{\mathbf{g}} \varphi_{\mathbf{g}} \exp\left\{i\left[(\mathbf{k}_\parallel + \mathbf{g})\cdot\varrho - \kappa_{\mathbf{g}} z\right]\right\}}_{\text{outgoing}} \tag{58}$$

Here, we have again decomposed the spatial vector $\mathbf{r}$ into a surface-parallel component $\varrho = (x, y)$ and a perpendicular component z. The perpendicular component of the wave vector is given by

$$\kappa_{\mathbf{g}} = \sqrt{2E - (\mathbf{k}_\parallel + \mathbf{g})^2} \tag{59}$$

Note that for beams that cannot escape from the solid into the vacuum $\kappa_{\mathbf{g}}$ is imaginary and their wave functions are damped in direction toward the vacuum. The intensities of the reflected beams, which are indicated by surface-reciprocal lattice vectors $\mathbf{g}$, are proportional to $|\varphi_{\mathbf{g}}|^2$. Inside the solid, proper solutions of the half-space problem can be expanded into Bloch and evanescent states,

$$\Psi(\mathbf{k}_\parallel; E) = \sum_j t^{(j)} \Psi^{(j)}(\mathbf{k}_\parallel, E; k_\perp^{(j)}) \tag{60}$$

To determine the coefficients $\varphi_{\mathbf{g}}$ and $t^{(j)}$, one requires that at a certain coordinate z_0 both the wave function and its derivative with respect to z are continuous. In matrix form, this requirement can be written as a relation between the coefficients of the bulk states ($t^{(j)}$) and those of the incoming ($\varphi_{\mathbf{g}}^+$) and outgoing ($\varphi_{\mathbf{g}}^-$) LEED beams,

$$B\mathbf{t} = A^+\varphi^+ + A^-\varphi^- \tag{61a}$$

$$B'\mathbf{t} = A^{+\prime}\varphi^+ + A^{-\prime}\varphi^- \tag{61b}$$

with

$$B_{\mathbf{g}j} = \sum_{\mathbf{G}} \alpha_{\mathbf{G}}^{(j)} \exp\left[i(k_\perp^{(j)} + G_\perp)z_0\right]\delta_{\mathbf{g}\mathbf{G}_\parallel} \tag{62a}$$

$$A^\pm_{\mathbf{g}\mathbf{g}'} = \exp(\pm i\kappa_{\mathbf{g}} z_0)\delta_{\mathbf{g}\mathbf{g}'} \tag{62b}$$

and analogous expressions for the matrices of the z derivatives, the latter being indicated by a prime ($A^{\pm\prime}$, B'). The incoming amplitudes φ^+ are represented by the vector that contains a 1 at the row of the (0, 0) beam and 0s otherwise. After some manipulation, one arrives at relations between the incoming amplitude φ^+ and the coefficients $\mathbf{t}$ of the solid's eigenfunctions as well as coefficients φ^- of the outgoing beams,

$$\mathbf{t} = \left[(B' - A'(A^-)^{-1}B)\right]^{-1} \times \left[A^{+\prime} - A^{-\prime}(A^-)^{-1}A^+\right]\varphi^+ \tag{63a}$$

$$\varphi^- = \left[(A^{-\prime} - B'(B)^{-1}A^-)\right]^{-1} \times \left[A^{+\prime} - B'(B)^{-1}A^+\right]\varphi^+ \tag{63b}$$

Note that one equation can be obtained by the other by simultaneously replacing A^- with B as well as $A^{-\prime}$ with B'.

With regard to the symmetry of the setup, not all of the wave functions $\Psi^{(j)}$ can couple to the LEED beams. Because the incident plane wave is totally symmetric at the detector [58], it belongs to the trivial representation of the "small group" of $\mathbf{k}_\parallel$ [59]. Thus, only those coefficients $t^{(j)}$ of wave functions $\Psi^{(j)}$ that belong to the same representation are nonzero.[12] This can easily be seen by the matching procedure which involves integration over the surface plane $z = z_0$.

The relation of the coefficients $t^{(j)}$ and the amplitudes of the outgoing beams $\varphi_{\mathbf{g}}$ allows a first interpretation of LEED $I(E)$ spectra. For example, if there is a bandgap at the energy of the incident beam, the latter cannot couple to Bloch states but to evanescent states inside the solid and thus has to be strongly reflected. This leads to a maximum in the $I(E)$ spectrum. In turn, if the incoming beam can couple very well to Bloch states,

[12] For example, if the incident beam impinges in a mirror plane of the solid, its plane wave is even under the associated reflection. Therefore, only wave functions $\Psi^{(j)}$ that are also even have nonvanishing expansion coefficients $t^{(j)}$.

the current is propagating toward the interior of the solid and the reflected intensity drops. This establishes a close connection between LEED intensities and electronic structure.

This method of wave function matching was first applied to LEED by Pendry [60–62]. It can also be applied for the determination of the band structure above the vacuum level, as has been demonstrated for Cu and semiconductors by Strocov and co-workers [63, 64]. Because the LEED wave functions appear also in photoemission as the final state (see Section 4), this method can be used in photoemission calculations [65–67]. On the mathematical problems related to this technique, we refer the reader to [68, 69].

The advantages of this method include the following: (i) In a LEED calculation, one is looking for the intensity for a given primary energy E and wave vector $\mathbf{k}_\parallel$ of the incoming beam. Due to the broken translational symmetry perpendicular to the surface, $k_\perp$ is not a "good quantum number;" that is, it is not conserved. (ii) Inelastic effects can be taken into account by an "optical potential," the imaginary part of which leads to broadening of the maxima in the $I(E)$ spectra (cf. Fig. 15 and Section 3.3).

However, problems occur in cases of ultra-thin films. Due to the confinement of the electronic states, the energy levels can become quantized (quantum-well states) and the description of LEED in terms of the bulk-band structure may not be appropriate. In the next section, we will introduce an approach that is by far better suited to the description of ultra-thin films and their electronic properties.

3.2.3. *Dynamical Theory*

In contrast to a kinematical theory (see Section 3.2.1), a dynamical theory considers multiple scattering of electrons inside the solid. Here, we can only give a brief survey and refer for a comprehensive description to textbooks by Mertig et al. [70], Weinberger [71], and Gonis [72].

The main task of a multiple-scattering theory for LEED is to determine the scattering properties of the whole semi-infinite solid. This is achieved by consecutive calculations of the scattering properties of a single site (sometimes loosely denoted as an "atom"), a single layer, stacks of layers, and eventually the entire solid. This step-by-step procedure gives a great flexibility concerning the actual arrangement of scatterers. Connected with these steps is a change of the basis in which the calculations are performed. For example, scattering from a single site is conveniently formulated in an angular-momentum basis that gives rise to so-called partial waves. Or scattering from layers is conveniently formulated in a plane wave basis.

The multiple-scattering theory as formulated in the following can be traced back to the original work of Korringa [73] as well as that of Kohn and Rostoker [74] who formulated it for three-dimensional systems. Because for surface problems a formulation in terms of layers is often more appropriate, the method that uses layers as an essential object is known as layer-KKR (see, e.g., [75]), where KKR stands for the initials of the inventors, Korringa, Kohn, and Rostoker.

Angular Momenta. Before turning to the multiple-scattering theory, a brief review of the basic properties of the angular-momentum operator $\mathbf{l} = (l_x, l_y, l_z)$ and the spin operator $\mathbf{s} = (s_x, s_y, s_z)$ is given. With the "ladder operators" $l_\pm = l_x \pm i l_y$, $s_\pm = s_x \pm i s_y$, and the total angular momentum $\mathbf{j} = \mathbf{l} + \mathbf{s}$, one has $2\mathbf{l}\cdot\mathbf{s} = 2l_z s_z + l_+ s_- + l_- s_+$ and the commutational rules $[j_z, \mathbf{s}\cdot\mathbf{l}] = 0$, $[\mathbf{j}^2, \mathbf{s}\cdot\mathbf{l}] = 0$, and $[s_z, \mathbf{s}\cdot\mathbf{l}] = -[l_z, \mathbf{s}\cdot\mathbf{l}]$.

Spherical harmonics are eigenfunctions of $\mathbf{l}^2$ and l_z, $\mathbf{l}^2 Y_l^m = l(l+1)Y_l^m$ and $l_z Y_l^m = m Y_l^m$. They obey the relation $(Y_l^m)^* = (-1)^m Y_l^{-m}$. Further, one has

$$l_z s_z Y_l^{\mu-\tau}\chi^\tau = (\mu-\tau)\tau Y_l^{\mu-\tau}\chi^\tau \tag{64a}$$

$$l_+ s_- Y_l^{\mu-\tau}\chi^\tau = \sqrt{l(l+1) - \left(\mu+\frac{1}{2}\right)\left(\mu+\frac{3}{2}\right)} \times Y_l^{\mu+1/2}\chi^- \delta_{\tau+} \tag{64b}$$

$$l_- s_+ Y_l^{\mu-\tau}\chi^\tau = \sqrt{l(l+1) - \left(\mu+\frac{1}{2}\right)\left(\mu-\frac{1}{2}\right)} \times Y_l^{\mu-1/2}\chi^+ \delta_{\tau-} \tag{64c}$$

with the Pauli spinors

$$\chi^+ = \begin{pmatrix} 1 \\ 0 \end{pmatrix} \tag{65a}$$

$$\chi^- = \begin{pmatrix} 0 \\ 1 \end{pmatrix} \tag{65b}$$

The latter are quantized with respect to the z direction; that is, they obey $\sigma_z \chi^\tau = \tau\chi^\tau$, $\tau = \pm$. μ is half-integer and runs from $-l - 1/2$ to $l + 1/2$. The Pauli matrices σ_i, $i = x, y, z$, read

$$\sigma_x = \begin{pmatrix} 0 & 1 \\ 1 & 0 \end{pmatrix} \tag{66a}$$

$$\sigma_y = \begin{pmatrix} 0 & -i \\ i & 0 \end{pmatrix} \tag{66b}$$

$$\sigma_z = \begin{pmatrix} 1 & 0 \\ 0 & -1 \end{pmatrix} \tag{66c}$$

The relativistic "companions" of the spherical harmonics are obtained by coupling $\mathbf{l}$ and $\sigma = 2\mathbf{s}$ and are given by [76]

$$\chi_\kappa^\mu = \sum_\tau C\left(l\tfrac{1}{2}j; \mu-\tau, \tau\right) Y_l^{\mu-\tau}\chi^\tau \tag{67}$$

They are eigenfunctions of $\sigma\cdot\mathbf{l} + 1$ with eigenvalues $\kappa = (j + 1/2)^2 - l(l+1)$. The coefficients C are the well-known Clebsch–Gordan coefficients,

$$C\left(l\tfrac{1}{2}j; \mu-\tau, \tau\right) = \frac{1}{\sqrt{2l+1}} \begin{cases} \tau = + & \tau = - \\ \sqrt{l+\mu+\frac{1}{2}} & \sqrt{l-\mu+\frac{1}{2}} \\ j = l+\frac{1}{2} & \\ -\sqrt{l-\mu+\frac{1}{2}} & \sqrt{l+\mu+\frac{1}{2}} \\ j = l-\frac{1}{2} & \end{cases} \tag{68}$$

Table I. Relationship between Relativistic Quantum Numbers κ and Nonrelativistic Ones l and j

κ	-5	-4	-3	-2	-1	$+1$	$+2$	$+3$	$+4$
l	4	3	2	1	0	1	2	3	4
$\bar{l}$	5	4	3	2	1	0	1	2	3
j	$\frac{9}{2}$	$\frac{7}{2}$	$\frac{5}{2}$	$\frac{3}{2}$	$\frac{1}{2}$	$\frac{1}{2}$	$\frac{3}{2}$	$\frac{5}{2}$	$\frac{7}{2}$

Note:Positive values of κ correspond to $j = l-(1/2)$, negative to $j = l+(1/2)$.

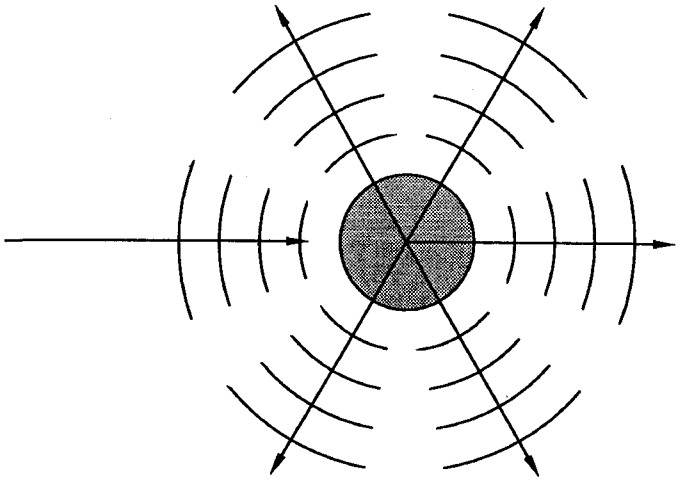

Fig. 17. Schematic view of scattering by a single potential (gray circle). The incoming and the outgoing partial waves are visualized by arrows and arcs.

For $j = l + (1/2)$ ($j = l - (1/2)$), one has $\kappa = -l - 1$ ($\kappa = l$); cf. Table I. With $r\sigma_r = \sum_{i=x,y,z} r_i\sigma_i$, it is $\sigma_r \chi_\kappa^\mu = -\chi_{-\kappa}^\mu$. Where possible, angular-momentum quantum numbers are combined to give a compound quantum number, in the nonrelativistic case $L = (l, m)$, in the relativistic case $\Lambda = (\kappa, \mu)$. Finally, we define $S_\kappa = \kappa/|\kappa|$, $\bar{l} = l - S_\kappa$, and $\bar{\Lambda} = (-\kappa, \mu)$.

Scattering by a Single Site. The first step in a multiple-scattering calculation is to determine the scattering properties of a single site. The basic idea is to expand both the incoming wave function and the scattered wave function with respect to angular momentum. For spherical potentials, the scattering problem is then solved for each angular momentum separately, giving rise to partial waves (cf. Fig. 17).

We assume that the potential inside the solid V_{solid} can be written as a sum over site-dependent potentials V_i,

$$V_{\text{solid}}(\mathbf{r}) = \sum_i V_i(\mathbf{r} - \mathbf{R}_i) \tag{69}$$

where the sum is over all sites. Usually, the site potentials are considered to be muffin-tin shape; that is, they are nonzero inside a sphere, spherically symmetric,

$$V_i(\mathbf{r}_i) = \begin{cases} V_i(r) & r \le r_{\text{mt}i} \\ 0 & \text{otherwise} \end{cases} \tag{70}$$

and the spheres of different sites do not overlap. Here, r_{mt} is the muffin-tin radius. Further, we assume that $\lim_{r\to 0} r^2 V(r) = 0$ [71]. Of course, generalizations to nonspherical as well as space-filling potentials have been developed (see, e.g., [77, 78]). In particular, the effect of nonspherical potentials on SPLEED intensities has been investigated by Krewer and Feder [79, 80].

Now the calculation of scattering phase shifts and of the single-site scattering matrix, which is a central quantity in multiple-scattering theory, is presented for the nonrelativistic case; that is, the radial Schrödinger equation is solved. For a free particle, the potential function vanishes in the whole space, $V(\mathbf{r}) = 0$. Because the potential is obviously spherically symmetric, the angular momentum l is conserved, l being a "good" quantum number. Therefore, the solutions of the radial Schrödinger equation can be characterized and indexed by l. For a particular value of l, the radial Schrödinger equation reads

$$\left(\partial_r^2 - \frac{l(l+1)}{r^2} + p^2\right) P_l(r) = 0 \tag{71}$$

where $p^2 = 2E$, $E > 0$. P_l is connected to the radial solution R_l by $P_l = rR_l$. Thus, the differential equation for R_l reads

$$\left(\partial_r^2 + \frac{2}{r}\partial_r + p^2 - \frac{l(l+1)}{r^2}\right) R_l(r) = 0 \tag{72}$$

The solutions $R_l(r)$ can be characterized as follows:

Regular solutions are finite in the limit $r \to 0$. For example, R_l, being proportional to a spherical Bessel function $j_l(pr)$ (discucced later), is regular. In other words, for $r \to 0$, R_l behaves like r^l and P_l correspondingly like r^{l+1}.

Irregular solutions diverge for $r \to 0$. R_l, which is proportional to a spherical Neumann function $n_l(pr)$ (discussed later), is irregular; that is, for $r \to 0$, R_l behaves like r^{-l-1} and P_l like r^{-l}.

Incoming and outgoing solutions. For large r, the "centrifugal" term $l(l+1)/r^2$ vanishes. Therefore, solutions should behave asymptotically as plane waves $\exp(\pm ipr)$. By linear combination of regular and irregular solutions, the required asymptotical behavior can be obtained. Spherical Hankel functions (discussed later) are these solutions. The incoming (outgoing) solution is given by zh_l^+ (zh_l^-), $z = pr$. Note that both Hankel functions are irregular.

For negative energy, $E < 0$, p is imaginary. Using the substitution $\tilde{p} = ip$, $\tilde{p} > 0$, the radial Schrödinger equation can be transformed into that for $E > 0$, Eq. (71) or Eq. (72), respectively. The solutions that can be obtained from the preceding but with argument $\tilde{p}r$ are the modified Bessel (i_l), Neumann (m_l), and Hankel functions (k_l). The latter obey the relations $i_l(pr) = (-i)^l j_l(ipr)$, $m_l(pr) = (-i)^{l+1} n_l(ipr)$, and $k_l^+(pr) = (-i)^{-l} h_l^+(ipr)$, respectively [81].

For a nonvanishing potential $V(r)$ of muffin-tin shape, it is convenient to match the solutions inside the sphere to those outside the sphere (free space) at the muffin-tin radius r_{mt}; that is, one requires that both the wave function and its r derivative

should be continuous. For $E > 0$ this yields, at r_{mt},

$$\sum_L R_l(r)Y_L(\hat{\mathbf{r}}) = \sum_L \left[A_l j_l(pr) + B_l n_l(pr)\right]Y_L(\hat{\mathbf{r}}) \quad (73a)$$

$$\sum_L \partial_r R_l(r)Y_L(\hat{\mathbf{r}}) = \sum_L \left[A_l \partial_r j_l(r) + B_l \partial_r n_l(pr)\right]Y_L(\hat{\mathbf{r}}) \quad (73b)$$

with regular R_l and $\hat{\mathbf{r}} = \mathbf{r}/r$. The unknown coefficients A_l and B_l are traditionally chosen as $\cos\delta_l$ and $-\sin\delta_l$. Thus, one has, using the orthonormality of spherical harmonics,

$$R_l(r) = \cos\delta_l j_l(pr) - \sin\delta_l n_l(pr) \quad (74a)$$

$$\partial_r R_l(r) = \cos\delta_l \partial_r j_l(pr) - \sin\delta_l \partial_r n_l(pr) \quad (74b)$$

After some manipulations, one arrives at

$$\tan\delta_l = \frac{(\partial_r R_l) j_l - R_l(\partial_r j_l)}{(\partial_r R_l) n_l - R_l(\partial_r n_l)} \quad (75)$$

δ_l is called the scattering phase shift of angular momentum l.[13] With the Wronskian $W(f, g) = f\partial_r g - g\partial_r f$, the preceding equation can be compactly written as $\tan\delta_l = W(j_l, R_l)/W(n_l, R_l)$. Using incoming Hankel functions instead of Neumann functions, that is,

$$R_l(r) = \left(j_l(pr) - ipt_l h_l^+(pr)\right)\exp(-i\delta_l) \quad (76)$$

one obtains the relation between the scattering phase shifts and the (l-diagonal) single-site scattering matrix t,

$$t_l = -\frac{1}{p}\sin\delta_l \exp(i\delta_l) \quad (77)$$

from which follows the "optical theorem" $\mathrm{Im}(t_l) = -p\, t_l\, t_l^*$. The real and imaginary parts of the t matrix fulfill $\mathrm{Re}(t_l) = -(\sin 2\delta_l)/(2p)$ and $\mathrm{Im}(t_l) = -(\sin^2\delta_l)/p$. Instead of the t matrix, sometimes the scattering amplitude $f_l = -pt_l$ or the reactance $K_l = -(\tan\delta_l)/p$ is used.

Scattering by a Single Site: The Relativistic Case. The Dirac equation for a single site with an effective magnetic field $\mathbf{B}(\mathbf{r})$ included reads

$$\left[c\alpha\cdot\mathbf{p} + \beta mc^2 + v(\mathbf{r}) + \beta\sigma\cdot\mathbf{B}(\mathbf{r})\right]\Psi(\mathbf{r}) = E\Psi(\mathbf{r}) \quad (78)$$

with

$$\alpha = \begin{pmatrix} 0 & \sigma \\ \sigma & 0 \end{pmatrix} \quad (79a)$$

$$\beta = \begin{pmatrix} 1 & 0 \\ 0 & -1 \end{pmatrix} \quad (79b)$$

[13] The required derivatives of the spherical Bessel and Neumann functions can be calculated via the relations

$$\left(\frac{1}{z}\partial_z\right)^m [z^{n+1} f_n] = z^{n-m+1} f_{n-m}$$

$$\left(\frac{1}{z}\partial_z\right)^m [z^{-n} f_n] = (-1)^m z^{-n-m} f_{n+m}$$

for $m = 1$. f_n is one of j_l, n_l, or $h_l^\pm$ [81].

Here, α and β are 4×4 matrices and Ψ is a Dirac spinor (4-spinor). The potential matrix $V(\mathbf{r})$ is defined by

$$V(\mathbf{r}) = \begin{pmatrix} v(\mathbf{r}) + \sigma\cdot\mathbf{B}(\mathbf{r}) & 0 \\ 0 & v(\mathbf{r}) - \sigma\cdot\mathbf{B}(\mathbf{r}) \end{pmatrix} \quad (80)$$

The solution of the Dirac equation for general potentials has been addressed by Tamura [82]. However, we restrict ourselves again to muffin-tin potentials. Thus, the direction of the effective magnetic field can be chosen conveniently along the z axis, that is, $v(\mathbf{r}) = v(r)$ and $\mathbf{B}(\mathbf{r}) = B(r)\mathbf{e}_z$. Because the effective magnetic field is coupled only to the spin, one can introduce spin-dependent potentials, $v_\pm(r) = v(r) \pm B(r)$. The potential matrix then reads

$$V(\mathbf{r}) = \begin{pmatrix} v_+(r) & 0 \\ 0 & v_-(r) \end{pmatrix} \quad (81)$$

For the wave function, we make the ansatz

$$\langle\mathbf{r}|\Psi\rangle = \frac{1}{r}\sum_\Lambda \begin{pmatrix} f_\Lambda(r)\langle\hat{\mathbf{r}}|\chi_\Lambda\rangle \\ ig_\Lambda(r)\langle\hat{\mathbf{r}}|\chi_{\bar{\Lambda}}\rangle \end{pmatrix} = \sum_\Lambda \begin{pmatrix} \Psi_\Lambda(r)\langle\hat{\mathbf{r}}|\chi_\Lambda\rangle \\ i\Phi_\Lambda(r)\langle\hat{\mathbf{r}}|\chi_{\bar{\Lambda}}\rangle \end{pmatrix} \quad (82)$$

that is, $\Psi_\Lambda(r) = f_\Lambda(r)/r$ and $\Phi_\Lambda(r) = g_\Lambda(r)/r$. The index Λ combines the relativistic angular-momentum quantum numbers κ and μ, $\Lambda = (\kappa, \mu)$ and $\bar{\Lambda} = (-\kappa, \mu)$ (discussed previously). Inserting the preceding ansatz into the Dirac equation yields a set of coupled equations for f_Λ and g_Λ,

$$c\partial_r f_\Lambda = -c\frac{\kappa}{r} f_\Lambda + (E + c^2 - v)g_\Lambda + B\sum_{\Lambda'}\langle\chi_{\bar{\Lambda}}|\sigma_z|\chi_{\bar{\Lambda}'}\rangle g_{\Lambda'} \quad (83a)$$

$$c\partial_r g_\Lambda = c\frac{\kappa}{r} g_\Lambda - (E - c^2 - v)f_\Lambda + B\sum_{\Lambda'}\langle\chi_\Lambda|\sigma_z|\chi_{\Lambda'}\rangle f_{\Lambda'} \quad (83b)$$

Note that in the nonmagnetic case ($B = 0$), one has

$$c\partial_r f_\Lambda = -c\frac{\kappa}{r} f_\Lambda + (E + c^2 - v)g_\Lambda \quad (84a)$$

$$c\partial_r g_\Lambda = c\frac{\kappa}{r} g_\Lambda - (E - c^2 - v)f_\Lambda \quad (84b)$$

that is, the solutions f_Λ and g_Λ are independent of the magnetic quantum number μ.

The matrix elements of σ_z can easily be obtained from the definition of χ_Λ. From the restriction $l' = l$, one has two cases, $\kappa' = \kappa$ and $\kappa' = -\kappa - 1$, which give

$$\langle\chi_\Lambda|\sigma_z|\chi_{\Lambda'}\rangle = \begin{cases} -\dfrac{2\mu}{2\kappa+1} & \text{for } \kappa' = \kappa \\ \sqrt{1 - \left(\dfrac{2\mu}{2\kappa+1}\right)^2} & \text{for } \kappa' = -\kappa - 1 \\ 0 & \text{otherwise} \end{cases} \quad (85)$$

Inserting Eq. (85) into Eq. (83), one finds terms that couple angular momenta l and $l+2$. As Ackermann has shown [83], these can be neglected due to the missing singularity of $B(r)$ at the origin. Thus, only partial waves with total angular momentum

$j = l + (1/2)$ and $j = l - (1/2)$ are coupled. Eventually, one arrives at a system of four coupled differential equations of first order,

$$c\partial_r f_{\kappa\mu} = -c\frac{\kappa}{r} f_{\kappa\mu} + \left(E + c^2 - v + B\frac{2\mu}{2\kappa - 1}\right) g_{\kappa\mu} \tag{86a}$$

$$c\partial_r g_{\kappa\mu} = c\frac{\kappa}{r} g_{\kappa\mu} - \left(E - c^2 - v - B\frac{2\mu}{2\kappa + 1}\right) f_{\kappa\mu} - B\sqrt{1 - \left(\frac{2\mu}{2\kappa - 1}\right)^2} f_{-\kappa-1,\mu} \tag{86b}$$

$$c\partial_r f_{-\kappa-1,\mu} = -c\frac{\kappa + 1}{r} f_{-\kappa-1,\mu} + \left(E + c^2 - v - B\frac{2\mu}{2\kappa + 3}\right) g_{-\kappa-1,\mu} \tag{86c}$$

$$c\partial_r g_{-\kappa-1,\mu} = -c\frac{\kappa + 1}{r} g_{-\kappa-1,\mu} - \left(E - c^2 - v + B\frac{2\mu}{2\kappa + 1}\right) f_{-\kappa-1,\mu} - B\sqrt{1 - \left(\frac{2\mu}{2\kappa + 1}\right)^2} f_{\kappa,\mu} \tag{86d}$$

As in the nonrelativistic case, two types of solutions can be distinguished due to their behavior in the vicinity of the origin, that is, regular and irregular solutions. Regular and irregular partial waves can be written as

$$\langle \mathbf{r}|\Psi^{\mathrm{x}}_{\Lambda}\rangle = \sum_{\Lambda'} \begin{pmatrix} \Psi^{\mathrm{x}}_{\Lambda'\Lambda}(r)\langle\hat{\mathbf{r}}|\chi_{\Lambda'}\rangle \\ i\Phi^{\mathrm{x}}_{\Lambda'\Lambda}(r)\langle\hat{\mathbf{r}}|\chi_{\overline{\Lambda'}}\rangle \end{pmatrix} \qquad \mathrm{x} = \mathrm{reg, irr} \tag{87}$$

and show the asymptotics

$$\langle \mathbf{r}|\Psi^{\mathrm{reg}}_{\Lambda}\rangle \to \sum_{\Lambda'} \begin{pmatrix} [j_l(kr)\delta_{\Lambda'\Lambda} + h^+_{l'}(kr)t_{\Lambda'\Lambda}]\langle\hat{\mathbf{r}}|\chi_{\Lambda'}\rangle \\ iS_{\kappa'}\dfrac{ck}{E + c^2}[j_{\bar{l}}(kr)\delta_{\Lambda'\Lambda} + h^+_{\bar{l}'}(kr)t_{\Lambda'\Lambda}]\langle\hat{\mathbf{r}}|\chi_{\overline{\Lambda'}}\rangle \end{pmatrix} \tag{88a}$$

$$\langle \mathbf{r}|\Psi^{\mathrm{irr}}_{\Lambda}\rangle \to \sum_{\Lambda'} \begin{pmatrix} h^+_{l'}(kr)\delta_{\Lambda'\Lambda}\langle\hat{\mathbf{r}}|\chi_{\Lambda'}\rangle \\ iS_{\kappa'}\dfrac{ck}{E + c^2}h^+_{\bar{l}'}(kr)\delta_{\Lambda'\Lambda}\langle\hat{\mathbf{r}}|\chi_{\overline{\Lambda'}}\rangle \end{pmatrix} \tag{88b}$$

for $r \to \infty$. The Wronskian is given by

$$\{\langle\Psi^{\mathrm{reg}}_{\Lambda}|, |\Psi^{\mathrm{irr}}_{\Lambda'}\rangle\} = \sum_{\Lambda''} cr^2\left(\Psi^{\mathrm{reg}}_{\Lambda''\Lambda}(r)\Phi^{\mathrm{irr}}_{\Lambda''\Lambda'}(r) - \Phi^{\mathrm{reg}}_{\Lambda''\Lambda}(r)\Psi^{\mathrm{irr}}_{\Lambda''\Lambda'}(r)\right) \tag{89a}$$

$$= \frac{ic^2}{k(E + c^2)}\delta_{\Lambda\Lambda'} \tag{89b}$$

which is independent of r.

Now one can calculate the single-site t matrix. The incoming partial wave is given by

$$\langle \mathbf{r}|J_{\Lambda}\rangle = \begin{pmatrix} j_l(kr)\langle\hat{\mathbf{r}}|\chi_{\Lambda}\rangle \\ iS_{\kappa}\dfrac{ck}{E + c^2}j_{\bar{l}}(kr)\langle\hat{\mathbf{r}}|\chi_{\overline{\Lambda}}\rangle \end{pmatrix} \tag{90}$$

With

$$\langle \mathbf{r}|H^{(i)}_{\Lambda}\rangle = \begin{pmatrix} h^i_l(kr)\langle\hat{\mathbf{r}}|\chi_{\Lambda}\rangle \\ iS_{\kappa}\dfrac{ck}{E + c^2}h^i_{\bar{l}}(kr)\langle\hat{\mathbf{r}}|\chi_{\overline{\Lambda}}\rangle \end{pmatrix} \qquad i = \pm \tag{91}$$

the total wave function is given by

$$\langle \mathbf{r}|\Psi\rangle = \sum_{\Lambda}\left(A_{\Lambda}\langle \mathbf{r}|J_{\Lambda}\rangle + B_{\Lambda}\langle \mathbf{r}|H^{(+)}_{\Lambda}\rangle\right) \tag{92}$$

The coefficients A_Λ (incoming) and B_Λ (outgoing) are connected by the single-site t matrix,

$$B_{\Lambda} = \sum_{\Lambda'} t_{\Lambda\Lambda'}A_{\Lambda'} \tag{93}$$

and can be obtained either by wave function matching [71] or by exploiting the Wronskians [82]. Due to the potential considered here, only those elements of t that belong to partial waves coupled by the radial Dirac equation are nonzero; that is, $t_{\Lambda\Lambda'} = 0$ if $\kappa' \notin \{\kappa, -\kappa - 1\}$ or $\mu' \neq \mu$. In the nonmagnetic case, the t matrix is diagonal in κ.

Many effects in electron spectroscopies of magnetic systems rely on the simultaneous presence of magnetization and spin-orbit coupling (SOC). For some purposes (e.g., testing and model calculations), it is desirable to vary the strengths of these. In nonrelativistic theories that include SOC as a perturbation, its strength can easily be changed by scaling the respective coupling constant. In relativistic theories, one usually sets the speed of light c to a rather large value, with the drawback that all relativistic effects (mass term, Darwin term) are changed, too. However, based on the scalar-relativistic approximation [84–86], one can derive an equation that interpolates between the fully relativistic (Dirac) and the scalar-relativistic Schrödinger equation [87–89].

Scattering by a Single Layer. After having solved the single-site problem, for example, having obtained the single-site t matrix, we now have to calculate the scattering properties of a single layer, the essential object in layer-KKR. In the following, only the case of one site per layer unit cell will be addressed. For each beam that is characterized by the reciprocal lattice vector $\mathbf{g}$, define the wave vector $\mathbf{k}^{\pm}_{\mathbf{g}}$ by

$$\mathbf{k}^{\pm}_{\mathbf{g}} = \begin{pmatrix} \mathbf{k}_{\parallel} + \mathbf{g} \\ \pm\sqrt{k^2 - (\mathbf{k}_{\parallel} + \mathbf{g})^2} \end{pmatrix} \tag{94}$$

with $c^2k^2 = E^2 - c^4$. The + (−) sign refers to plane waves propagating or decaying in the $+z$ ($-z$) direction. The wave fields incident on (Ψ_{inc}) and outgoing from (Ψ_{out}) the layer can

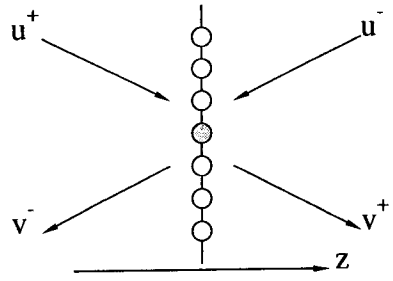

Fig. 18. Schematic view of scattering by a layer, that is, a two-dimensional periodic arrangement of scatterers (circles). The reference scatterer is represented as a gray circle. Incoming (outgoing) beams are labeled $u^{\pm}$ ($v^{\pm}$) with respect to the propagation direction ($\pm z$).

be written as

$$\Psi_{\text{inc}}(\mathbf{r}) = \sum_{g\tau}\left[u^{+}_{g\tau}\exp(i\mathbf{k}^{+}_{g}\cdot\mathbf{r}) + u^{-}_{g\tau}\exp(i\mathbf{k}^{-}_{g}\cdot\mathbf{r})\right]\chi^{\tau} \quad (95a)$$

$$\Psi_{\text{out}}(\mathbf{r}) = \sum_{g\tau}\left[v^{+}_{g\tau}\exp(i\mathbf{k}^{+}_{g}\cdot\mathbf{r}) + v^{-}_{g\tau}\exp(i\mathbf{k}^{-}_{g}\cdot\mathbf{r})\right]\chi^{\tau} \quad (95b)$$

Arranging the coefficients $u^{\pm}_{g\tau}$ and $v^{\pm}_{g\tau}$ into column vectors, the connection between these is defined in terms of the scattering matrix M of the layer (see Fig. 18),

$$\begin{pmatrix}\mathbf{v}^{+}\\ \mathbf{v}^{-}\end{pmatrix} = \begin{pmatrix}M^{++} & M^{+-}\\ M^{-+} & M^{--}\end{pmatrix}\begin{pmatrix}\mathbf{u}^{+}\\ \mathbf{u}^{-}\end{pmatrix} \quad (96)$$

Thus, the M matrix corresponds to the single-site t matrix but for an entire layer; cf. Eq. (93).

To calculate the M matrix, one expands the incoming wave into spherical waves. Using

$$\exp(i\mathbf{k}\cdot\mathbf{r})\chi^{\tau} = \sum_{\Lambda} a_{\Lambda\tau}(\hat{\mathbf{k}})j_l(kr)\chi_{\Lambda}(\hat{\mathbf{r}}) \qquad \tau = \pm \quad (97)$$

with coefficients [cf. Eq. (67)]

$$a_{\Lambda\tau}(\hat{\mathbf{k}}) = 4\pi i^{l} C\left(l\tfrac{1}{2}j;\mu-\tau,\tau\right)\left(Y_l^{\mu-\tau}(\hat{\mathbf{k}})\right)^{*} \qquad \tau = \pm \quad (98)$$

one obtains for the wave field

$$\sum_{g} u^{\pm}_{g\tau}\exp(i\mathbf{k}^{\pm}_{g}\cdot\mathbf{r})\chi^{\tau} = \sum_{\Lambda} A^{\pm(0)}_{\Lambda\tau} j_l(kr)\chi_{\Lambda}(\hat{\mathbf{r}}) \qquad \tau = \pm \quad (99)$$

with $A^{\pm(0)}_{\Lambda\tau} = \sum_{g} a_{\Lambda\tau}(\hat{\mathbf{k}}^{\pm}_{g})u^{\pm}_{g\tau}$ and $k = \sqrt{2E + E^2/c^2}$. The incoming wave is multiply scattered at each site of the layer, which leads to the wave field $\sum_{\Lambda} A_{\Lambda\tau} j_l(kr)\chi_{\Lambda}(\hat{\mathbf{r}})$ incident at the reference atom. The wave field incident at site $\mathbf{R}_j$ is given by

$$\sum_{\Lambda} A_{\Lambda\tau} j_l(kr_j)\chi_{\Lambda}(\hat{\mathbf{r}}_j)\exp(i\mathbf{k}_{\parallel}\cdot\mathbf{R}_j) \quad (100)$$

with $\mathbf{r}_j = \mathbf{r} - \mathbf{R}_j$. The outgoing wave field from this site is

$$\sum_{\Lambda} B_{\Lambda\tau} h_l^{+}(kr_j)\chi_{\Lambda}(\hat{\mathbf{r}}_j)\exp(i\mathbf{k}_{\parallel}\cdot\mathbf{R}_j) \quad (101)$$

and the coefficients $B_{\Lambda'\tau}$ and $A_{\Lambda\tau}$ are connected by the t matrix, Eq. (93). The total incident wave field at the reference atom can be separated into a direct part, which stems from the nonlayer region (incident onto the layer), and a layer part, which is due to multiple scattering within the layer. The latter reads

$$\sum_{\Lambda} A^{\text{layer}}_{\Lambda\tau} j_l(kr)\chi_{\Lambda}(\hat{\mathbf{r}}) = \sum_{j}{}' \exp(i\mathbf{k}_{\parallel}\cdot\mathbf{R}_j)\sum_{\Lambda'} B_{\Lambda'\tau} h_{l'}^{+}(kr_j)\chi_{\Lambda'}(\hat{\mathbf{r}}_j) \quad (102)$$

where the first sum (indicated by a prime) is over all sites within the layer except the reference atom. The coefficients $A^{\text{layer}}_{\Lambda\tau}$ can be obtained with the help of the layer structure constant $G_{\Lambda\Lambda'}(-\mathbf{R}_j)$ (for a detailed discussion, see [42, 72]), which obeys

$$h_l^{+}(kr_j)\chi_{\Lambda}(\hat{\mathbf{r}}_j) = \sum_{\Lambda'} G_{\Lambda\Lambda'}(-\mathbf{R}_j) j_{l'}(kr_j)\chi_{\Lambda'}(\hat{\mathbf{r}}_j) \quad (103)$$

The relativistic structure constant is related to the nonrelativistic one by Clebsch–Gordan coefficients,

$$G_{\Lambda\Lambda'}(-\mathbf{R}_j) = \sum_{\tau} C\left(l\tfrac{1}{2}j;\mu-\tau,\tau\right) G_{l,\mu-\tau;l',\mu'-\tau}(-\mathbf{R}_j) \times C\left(l'\tfrac{1}{2}j';\mu'-\tau,\tau\right) \quad (104)$$

Thus, one has

$$A^{\text{layer}}_{\Lambda\tau} = \sum_{j}{}' \exp(i\mathbf{k}_{\parallel}\cdot\mathbf{R}_j)\sum_{\Lambda'} B_{\Lambda'\tau} G_{\Lambda'\Lambda}(-\mathbf{R}_j) \quad (105)$$

It is convenient to introduce a "multiple-scattering matrix" X by $A^{\text{layer}}_{\Lambda\tau} = \sum_{\Lambda'} A_{\Lambda'\tau} X_{\Lambda'\Lambda}$, which is easily calculated as

$$X_{\Lambda''\Lambda} = \sum_{\Lambda'} t_{\Lambda''\Lambda'} \sum_{j}{}' \exp(i\mathbf{k}_{\parallel}\cdot\mathbf{R}_j) G_{\Lambda'\Lambda}(-\mathbf{R}_j) \quad (106)$$

The total incoming wave field at the reference atom is then given by

$$A_{\Lambda\tau} = A^{+(0)}_{\Lambda\tau} + A^{-(0)}_{\Lambda\tau} + A^{\text{layer}}_{\Lambda\tau} = A^{+(0)}_{\Lambda\tau} + A^{-(0)}_{\Lambda\tau} + \sum_{\Lambda'} A_{\Lambda'\tau} X_{\Lambda'\Lambda} \quad (107)$$

or, in matrix notation, $A = A^{(0)} + AX$, from which one obtains $A = A^{(0)}(1-X)^{-1}$. Eventually, the blocks of the M matrix can be written formally as

$$M^{s,s'} = \delta_{s,s'} + a^{s} t (1-X)^{-1} b^{s'} \qquad s, s' = \pm \quad (108)$$

where $a_{\Lambda\tau}(\hat{\mathbf{k}}^{\pm}_{g})$ transforms from angular-momentum into plane wave representation [cf. Eq. (98)], $b_{\Lambda\tau}(\hat{\mathbf{k}}^{\pm}_{g})$ vice versa.

Scattering by a Double Layer. To calculate the scattering properties of an arbitrary stack of layers, one starts with the M matrix of a double layer, that is, a stack of two layers. By consecutive application of the following computational scheme,

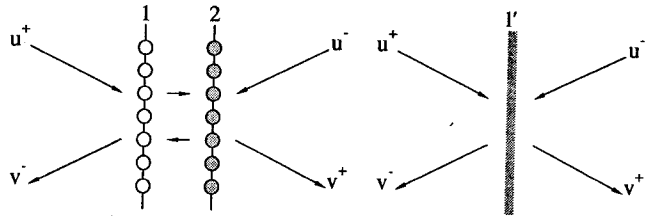

Fig. 19. Schematic view of scattering by a double layer, that is, a stack of two layers (1 and 2, left). The scattering properties can be cast into an effective scatterer (1′, right).

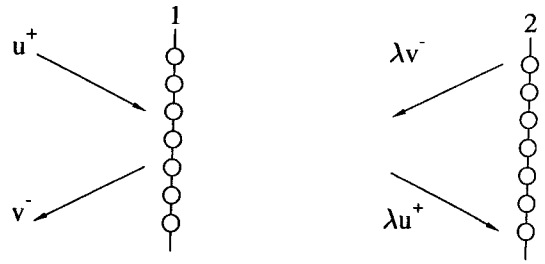

Fig. 20. Bloch waves in multiple-scattering theory. For identical layers (1 and 2), plane waves on the right ($\lambda\mathbf{u}^+$, $\lambda\mathbf{v}^-$) are multiples of those on the left ($\mathbf{u}^+$, $\mathbf{v}^-$) due to Floquet's theorem.

one eventually obtains the M matrix of the stack. The "layer-doubling" algorithm for computation of the bulk reflection matrix (discussed later) is also based on this method.

One starts with a stack consisting of two layers, labeled 1 and 2, which need not be identical; cf. Figure 19. The result is the M matrix of this stack, labeled 1′,

$$\begin{pmatrix}\mathbf{v}^+\\ \mathbf{v}^-\end{pmatrix}=\begin{pmatrix}M_{1'}^{++} & M_{1'}^{+-}\\ M_{1'}^{-+} & M_{1'}^{--}\end{pmatrix}\begin{pmatrix}\mathbf{u}^+\\ \mathbf{u}^-\end{pmatrix} \tag{109}$$

Summing up all multiple-scattering events that are due to reflection at each layer, one obtains for the amplitudes of the plane waves

$$\begin{aligned}\mathbf{v}^+ &= M_2^{++}P^+(1-M_1^{+-}P^-M_2^{-+}P^+)^{-1}M_1^{++}\mathbf{u}^+\\ &\quad+\left[M_2^{+-}+M_2^{++}P^+M_1^{+-}P^-\right.\\ &\quad\left.\times(1-M_2^{-+}P^+M_1^{+-}P^-)^{-1}M_2^{--}\right]\mathbf{u}^- \qquad (110a)\\ \mathbf{v}^- &= \left[M_1^{-+}+M_1^{--}P^-M_2^{-+}P^+\right.\\ &\quad\left.\times(1-M_1^{+-}P^-M_2^{-+}P^+)^{-1}M_1^{++}\right]\mathbf{u}^+\\ &\quad+M_1^{--}P^-(1-M_2^{-+}P^+M_1^{+-}P^-)^{-1}M_2^{--}\mathbf{u}^- \qquad (110b)\end{aligned}$$

where we have used $1+x+x^2+x^3+\cdots=(1-x)^{-1}$. For convenience, matrices $N^{\pm\pm}$ are introduced, that is, $M^{\pm\pm}$ matrices enhanced by plane wave propagators $P^\pm$, $N^{++}=P^+M^{++}$, $N^{+-}=P^+M^{+-}P^-$, $N^{-+}=M^{-+}$, and $N^{--}=M^{--}P^-$, which yields

$$N_{1'}^{++}=N_2^{++}(1-N_1^{+-}N_2^{-+})^{-1}N_1^{++} \tag{111a}$$
$$N_{1'}^{+-}=N_2^{+-}+N_2^{++}N_1^{+-}(1-N_2^{-+}N_1^{+-})^{-1}N_2^{--} \tag{111b}$$
$$N_{1'}^{-+}=N_1^{-+}+N_1^{--}N_2^{-+}(1-N_1^{+-}N_2^{-+})^{-1}N_1^{++} \tag{111c}$$
$$N_{1'}^{--}=N_1^{--}(1-N_2^{-+}N_1^{+-})^{-1}N_2^{--} \tag{111d}$$

The elements of the diagonal matrices $P^\pm$ are defined by

$$P^\pm_{\mathbf{g}\tau,\mathbf{g}'\tau'}=\exp(i\mathbf{k}_\mathbf{g}^\pm\cdot\mathbf{d})\delta_{\mathbf{g}\mathbf{g}'}\delta_{\tau\tau'} \tag{112}$$

where $\mathbf{d}$ is the translation vector from layer 1 to layer 2 (cf. Fig. 1). Note the relation between $N_{1'}^{++}$ and $N_{1'}^{--}$ as well as that between $N_{1'}^{+-}$ and $N_{1'}^{-+}$: By interchanging $+\leftrightarrow-$ and $1\leftrightarrow2$ in one expression, one obtains the other.

The preceding procedure can be used to calculate iteratively the bulk reflection matrix R_{bulk}^{-+}, known as the "layer-doubling" method. The bulk is defined as an infinitely repeated arrangement of identical layers or stacks of layers (principal layers). One first calculates the M matrix of a double layer, subsequently the M matrix of a doubled double layer, which yields M of a stack of four layers, and so on. After n iterations, the M matrix of 2^n layers is obtained. The bulk reflection matrix is eventually given by M^{-+} of the 2^n-layer stack. The "layer-doubling" procedure is repeated until (i) the change of the bulk reflection matrix of the 2^{n-1} stack and the 2^n stack is small enough to be regarded as negligible or (ii) the incoming waves $\mathbf{u}^+$ are absorbed within the stack; that is, M^{++} is close enough to 0. In practical LEED calculations, which take into account the mean free path via an absorptive optical potential, three or four iterations are regarded as sufficient.

Bloch Wave Method. The M matrix of a layer or a stack of layers can be used to compute the bulk-band structure $k_\perp(E,\mathbf{k}_\parallel)$. Consider identical layers 1 and 2, which are connected by a vector $\mathbf{d}$. On the left-hand side of layer 1, we have incoming and outgoing waves $\mathbf{u}^+$ and $\mathbf{v}^-$. Due to Floquet's theorem, the plane waves on the left-hand side of layer 2 are these plane waves but multiplied by a factor (λ in Fig. 20). Thus, the outgoing waves $\lambda\mathbf{u}^+$ and $\mathbf{v}^-$ are related to the incoming waves $\mathbf{u}^+$ and $\lambda\mathbf{v}^-$ by

$$\lambda\mathbf{u}^+=N^{++}\mathbf{u}^++\lambda N^{+-}\mathbf{v}^- \tag{113a}$$
$$\mathbf{v}^-=N^{-+}\mathbf{u}^++\lambda N^{--}\mathbf{v}^- \tag{113b}$$

In matrix notation, the eigenvectors and eigenvalues can be obtained from the generalized eigenproblem

$$\begin{pmatrix}N^{++} & 0\\ -N^{-+} & 1\end{pmatrix}\begin{pmatrix}\mathbf{u}^+\\ \mathbf{v}^-\end{pmatrix}=\lambda\begin{pmatrix}1 & -N^{+-}\\ 0 & N^{--}\end{pmatrix}\begin{pmatrix}\mathbf{u}^+\\ \mathbf{v}^-\end{pmatrix} \tag{114}$$

which can be solved by standard numerical program packages. However, by some algebra the preceding equation can be transformed into standard form, $Q\mathbf{c}_n=\lambda_n\mathbf{c}_n$, with the blocks of the matrix Q given by

$$Q^{++}=N^{++}-N^{+-}(N^{--})^{-1}N^{-+} \tag{115a}$$
$$Q^{+-}=N^{+-}(N^{--})^{-1} \tag{115b}$$
$$Q^{-+}=-(N^{--})^{-1}N^{-+} \tag{115c}$$
$$Q^{--}=(N^{--})^{-1} \tag{115d}$$

Here, the eigenvalue λ_n is in general complex and $\mathbf{c}_n$ is a $4N_\mathbf{g}$ vector, $N_\mathbf{g}$ being the number of reciprocal lattice vectors $\mathbf{g}$ taken into account. The upper (lower) $2N_\mathbf{g}$ components of $\mathbf{c}_n$ describe

waves propagating or decaying in the $+z$ direction ($-z$ direction). The wave vector $\mathbf{k}$ of the Bloch waves can be decomposed into components parallel, $\mathbf{k}_\parallel$, and perpendicular, $k_\perp$, to the layer. Thus, the eigenvalue can be written as $\lambda_n = \exp(i\mathbf{k}_n \cdot \mathbf{d})$ from which $k_{n,\perp}$ is obtained as

$$k_{n,\perp} = \frac{-i}{d_\perp}(\ln \lambda_n - i\mathbf{k}_\parallel \cdot \mathbf{d}_\parallel) \tag{116}$$

In conclusion, the bulk-band structure has been computed as $k_\perp(E, \mathbf{k}_\parallel)$.

Eigenfunctions with $|\lambda_n| = 1$ belong to the real band structure; that is, they fulfill the Bloch condition. But even if the energy is real, the set of eigenvalues $\{\lambda_n\}$ consists of values with modulus greater than or less than 1. In particular, the norms of the corresponding wave functions increase or decrease when propagating across a layer. It is clear that these solutions cannot be normalized in the bulk because only square-integrable functions ($\mathcal{L}_2$ functions) belong to the Hilbert space. If, however, a surface is present the normalization has to be carried out only in the half-space $z > 0$. Thus, in addition to Bloch states solutions with $|\lambda_n| < 1$ are allowed. The latter are the evanescent states, that is, those states with decreasing amplitude when propagating into the interior of the semi-infinite solid.

Once the eigenfunctions and eigenvalues of the Q matrix are known, they can be used to calculate the reflection matrix of the bulk. The $4N_\mathbf{g}$ eigenvectors can be classified into those that (i) decay exponentially in the z direction, (ii) decay in the $-z$ direction, (iii) have positive probability current perpendicular to the layers, and (iv) have negative probability current perpendicular to the layers. The eigenvectors can be arranged such that those $2N_\mathbf{g}$ of them that decay in the $+z$ direction and the current of which is positive comprise the first $2N_\mathbf{g}$ rows of the eigenvector matrix V. The relation between plane waves and eigenvectors then reads

$$\begin{pmatrix} \mathbf{c}^+ \\ \mathbf{c}^- \end{pmatrix} = \begin{pmatrix} V^{++} & V^{+-} \\ V^{-+} & V^{--} \end{pmatrix} \begin{pmatrix} 0 \\ \mathbf{u}^- \end{pmatrix} \tag{117}$$

Here, $\mathbf{u}^+$ equals 0 because the outgoing waves in the $+z$ direction of an infinitely thick slab vanish. In practical calculation, this is assured by adding a small imaginary constant to the energy or to the potential in order to simulate inelastic scattering of the electrons [53]. In this way, there are, strictly speaking, no Bloch states, only evanescent states that decay in either the $+z$ or the $-z$ direction. Eliminating $\mathbf{u}^-$ in the preceding equation yields the bulk reflection matrix R^{-+}_{bulk},

$$\mathbf{c}^- = V^{--}(V^{-+})^{-1}\mathbf{c}^+ = R^{-+}_{\text{bulk}}\mathbf{c}^+ \tag{118}$$

Scattering from the Surface Barrier. At this point, one has to consider the surface region of the solid. In multiple-scattering theory, the surface barrier is treated as an additional layer that enters via its M matrix. For a step barrier, which appears to be sufficient in calculations for typical LEED energies, the latter can easily be calculated as

$$M^{++}_{\mathbf{g}\tau,\mathbf{g}'\tau'} = 2k_{\perp\mathbf{g}}/(k_{\perp\mathbf{g}} + k^{\text{in}}_{\perp\mathbf{g}})\delta_{\mathbf{g}\mathbf{g}'}\delta_{\tau\tau'} \tag{119a}$$

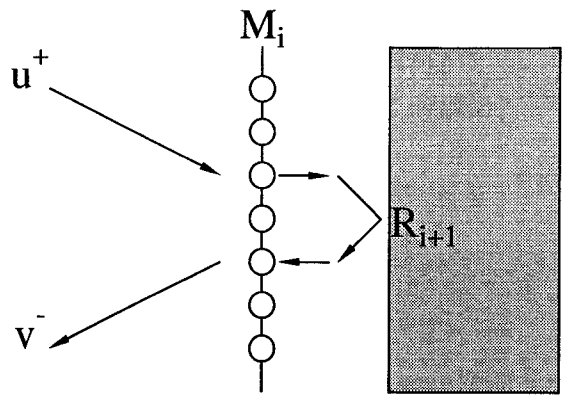

Fig. 21. Reflection of a stack of layers. The incoming wave $\mathbf{u}^+$ is reflected into $\mathbf{v}^-$ by layer i (which is described by its scattering matrices $M_i^{\pm\pm}$) and the stack of layers with index greater than i (which is described by the reflection matrix R^{-+}_{i+1}).

$$M^{+-}_{\mathbf{g}\tau,\mathbf{g}'\tau'} = (k^{\text{in}}_{\perp\mathbf{g}} - k_{\perp\mathbf{g}})/(k_{\perp\mathbf{g}} + k^{\text{in}}_{\perp\mathbf{g}})\delta_{\mathbf{g}\mathbf{g}'}\delta_{\tau\tau'} \tag{119b}$$

$$M^{-+}_{\mathbf{g}\tau,\mathbf{g}'\tau'} = (k_{\perp\mathbf{g}} - k^{\text{in}}_{\perp\mathbf{g}})/(k_{\perp\mathbf{g}} + k^{\text{in}}_{\perp\mathbf{g}})\delta_{\mathbf{g}\mathbf{g}'}\delta_{\tau\tau'} \tag{119c}$$

$$M^{--}_{\mathbf{g}\tau,\mathbf{g}'\tau'} = 2k^{\text{in}}_{\perp\mathbf{g}}/(k_{\perp\mathbf{g}} + k^{\text{in}}_{\perp\mathbf{g}})\delta_{\mathbf{g}\mathbf{g}'}\delta_{\tau\tau'} \tag{119d}$$

with

$$k_{\perp\mathbf{g}} = \sqrt{2E - (\mathbf{k}_\parallel + \mathbf{g})^2} \tag{120a}$$

$$k^{\text{in}}_{\perp\mathbf{g}} = \sqrt{2(E + V_0) - (\mathbf{k}_\parallel + \mathbf{g})^2} \tag{120b}$$

Here, V_0 is the inner potential, that is, the energy shift of the muffin-tin potentials inside the solid relative to the vacuum level, which is chosen as 0 eV for convenience.

In VLEED, however, a barrier with image-potential asymptotics, that is, $V(z) \approx 1/(4z)$, is better suited [90]. The JJJ barrier, which interpolates smoothly between the image potential in the vacuum and the constant inner potential V_0 in the solid, was introduced by Jones, Jennings, and Jepsen [91] (thus the name JJJ) and improved by Tamura and Feder [92]. Besides simple integration of the Schrödinger equation in the surface region with standard numerical methods, highly sophisticated, methods have been proposed that take into account the corrugation, that is, the variation of the potential parallel to the surface [67, 68, 93, 94].

Calculation of the Total Reflection Matrix. To compute the reflected intensities $I_\mathbf{g}(E)$, the reflection matrix of the semi-infinite system has to be calculated. If the scattering matrices of all layers and the bulk reflection matrix have been determined, the total reflection matrix R_{tot} can be calculated step by step. Consider the scattering matrices $M_i^{\pm\pm}$ of layer i and the reflection matrix R^{-+}_{i+1} of the stack of layers with index greater than i (cf. Fig. 21). Then the reflection matrix R_i^{-+} of the stack comprising all layers with index greater than or equal to i is given by

$$R_i^{-+} = M_i^{-+} + M_i^{--}P^- R^{-+}_{i+1}(1 - P^+ M_i^{+-} P^- R^{-+}_{i+1})^{-1} \times P^+ M_i^{++} \tag{121}$$

The first term is solely due to reflection at layer i, whereas the second term takes into account multiple scattering between layer i and the stack of layers on the r.h.s. of layer i.

Starting with the bulk reflection matrix R^{-+}_{bulk} and the scattering matrices $M^{\pm\pm}_n$ of the first non-bulk-like layer n, one calculates the reflection matrix R^{-+}_{n-1} of this stack according to the preceding scheme. For example, from R^{-+}_{n-1} and $M^{\pm\pm}_{n-2}$, one computes R^{-+}_{n-2}, and so forth. Eventually, one obtains the reflection matrix R^{tot} of the entire semi-infinite system.

Spin-Polarized Low-Energy Electron Diffraction. Now we have gathered all ingredients for calculating SPLEED. After computing the single-site t matrices of the scatterers, one computes the M matrices of each layer (including the surface barrier). From these, one calculates the bulk reflection matrix, from which, in turn, the reflection matrix R^{tot} of the entire semi-infinite system can be computed. This step-by-step procedure allows for a great flexibility with respect to the geometrical setup of the solid. Therefore, it is not only suited to semi-infinite systems that are built by a single type of layer, but can handle any arrangement of layers, in particular, ultra-thin films on a substrate [95].

In SPLEED, one uses a spin-polarized incoming electron beam with spin polarization $\mathbf{P}^{\text{in}}$ and measures intensity $I_{\mathbf{g}}$ and spin polarization $P^{\text{out}}_{\mathbf{g}}$ of the reflected beams. The density matrix ϱ^{in} of the incoming electron beam is related to the spin polarization $\mathbf{P}^{\text{in}}$ by $\varrho^{\text{in}} = (1 + \mathbf{P}^{\text{in}} \cdot \sigma)/2$. The density matrix $\varrho^{\text{out}}_{\mathbf{g}}$ of an outgoing beam is therefore given by $\varrho^{\text{out}}_{\mathbf{g}} = \varrho_{\mathbf{g}} \varrho^{\text{in}} \varrho^{\dagger}_{\mathbf{g}}$ [96, 97]. $\varrho_{\mathbf{g}}$ is given by $\varrho_{\mathbf{g}\tau\tau'} = R^{\text{tot}}_{\mathbf{g}\tau,0\tau'}(E_{\perp\mathbf{g}}/E_{\perp 0})^{1/4}$ with the "effective" energies $E_{\perp\mathbf{g}} = 2E - (k_{\parallel} + \mathbf{g})^2$. Intensity and spin polarization of the outgoing LEED beams are obtained from $\varrho^{\text{out}}_{\mathbf{g}}$ by $I_{\mathbf{g}} = \text{tr}(\varrho^{\text{out}}_{\mathbf{g}})$ and $\mathbf{P}^{\text{out}}_{\mathbf{g}} = \text{tr}(\sigma \varrho^{\text{out}}_{\mathbf{g}})/I_{\mathbf{g}}$.

In a typical SPLEED experiment from ferromagnetic systems, one chooses the spin polarization of the incoming beam $\mathbf{P}^{\text{in}}$ either parallel or antiparallel to some direction $\hat{\mathbf{p}}$. The sample magnetization $\mathbf{M}$ can be aligned, for example, via an external magnetic field, parallel or antiparallel to some other direction $\hat{\mathbf{m}}$. Therefore, one can detect for each outgoing beam four intensities $I^{\pm\pm}_{\mathbf{g}}$ where the first (second) superscript refers to $\mathbf{P}^{\text{in}}$ ($\mathbf{M}$). With $I_{\mathbf{g}}$ being the sum of these four intensities, one defines the asymmetries

$$A^{\text{so}}_{\mathbf{g}} = (I^{++}_{\mathbf{g}} + I^{+-}_{\mathbf{g}} - I^{-+}_{\mathbf{g}} - I^{--}_{\mathbf{g}})/I_{\mathbf{g}} \qquad (122a)$$

$$A^{\text{ex}}_{\mathbf{g}} = (I^{++}_{\mathbf{g}} - I^{+-}_{\mathbf{g}} - I^{-+}_{\mathbf{g}} + I^{--}_{\mathbf{g}})/I_{\mathbf{g}} \qquad (122b)$$

$$A^{\text{un}}_{\mathbf{g}} = (I^{++}_{\mathbf{g}} - I^{+-}_{\mathbf{g}} + I^{-+}_{\mathbf{g}} - I^{--}_{\mathbf{g}})/I_{\mathbf{g}} \qquad (122c)$$

where the labels "so," "ex," and "un" are short for spin-orbit coupling, exchange, and unpolarized, respectively. In A^{so}, effects due to the magnetization cancel and thus leave SOC as the main source of the intensity difference. Analogously, SOC effects cancel in A^{ex} but effects due to exchange are kept. A^{un} is the asymmetry of an unpolarized incoming beam due to magnetization reversal (cf. [97]).

As mentioned in Section 3.1, LEED provides information on the geometrical arrangement of the scattering sites. Thus, by comparing experimental with theoretical $I(E)$ spectra, one can determine the geometric structure of a sample by a systematical search; for example, by variation of structural parameters (the positions of the scatterers) and nonstructural parameters (the mean free path), one tries to minimize an objective function, which gives a measure of the agreement between experiment and theory (see, e.g., [6, p. 38]). These objective functions are called reliability factors, or for short R factors, and take into account energy positions and width of intensity maxima [98, 99]. Further, via SPLEED analysis, one is able to determine nongeometrical quantities. For example, the enhancement of the magnetic moment at the (110) surface of Fe has been found by comparing experimental and theoretical $I(E)$ spectra, treating the surface magnetic moment as a fit parameter [100] (for an *ab initio* calculation of magnetic properties of surfaces, see [101] and references therein).

Temperature effects occur prominently as thermal vibrations of the scattering sites that reduce the reflected intensities and increase the background. In LEED, this is approximately taken into account by multiplying the elements of the single-site t matrix by effective Debye–Waller factors [7, 12], thus ignoring the correlation of the motion (e.g., phonons), which might appear important because of multiple scattering (see, e.g., [102]).

3.3. Application: Quantum-Well Resonances in Ferromagnetic Co Films

As a typical example of the manifestation of electron scattering within an ultra-thin film, we address quantum-well resonances (QWRs) (see Fig. 22). As introduced in Section 2, QWSs are quantized electronic states that are confined to an ultra-thin film. Strict confinement on the substrate side of the film is possible if there is a gap in the substrate band structure. On the vacuum side, confinement is achieved by the surface barrier (cf. "QWS" in Fig. 22). At energies above the vacuum level, there is no total reflection at the surface barrier and, therefore, the electronic states in the film are not strictly confined. In other words, they are resonant with the free-electron states in the vacuum (cf. "QWR" in Fig. 22). In a ferromagnetic film on a nonmagnetic substrate, QWRs are characterized as exchange-split pairs of peaks in the $\mathbf{k}_{\parallel}$-resolved and layer-projected density of states (DOS), that is, the Bloch spectral function. Therefore, at the energy of a QWR, LEED electrons incident from the vacuum side have highest probability of entering the film and, consequently, a minimal reflection coefficient; that is, QWRs show up as minima in the SPLEED spectra.

Similar connections exist between the electronic structure of semi-infinite systems and other electron spectroscopies. It is well known that the LEED reflectivity is maximal for energies in bulk-band gaps (see Section 3.2.2) and tends to have minima at energies near band edges [45]. These minima correspond to maxima in the fine structure of secondary electron emission spectra [103]. Likewise, band edges are mirrored by maxima in the target current absorbed by the crystal [104] because the target current is complementary to the LEED reflectivity. Therefore, it could also be used to study QWRs.

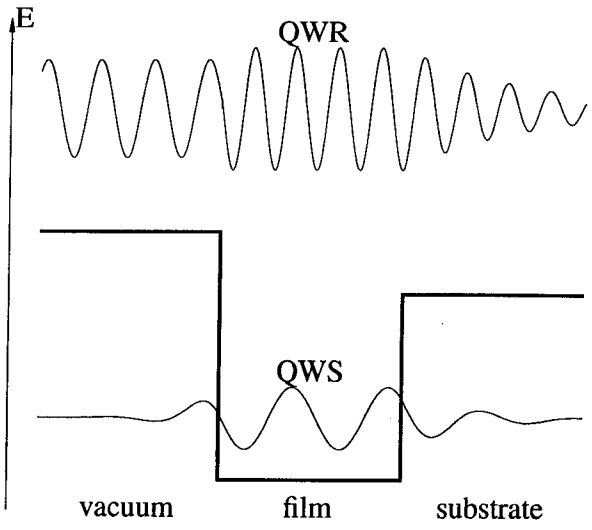

Fig. 22. Quantum-well resonance (QWR) and quantum-well state (QWS) in an ultra-thin film. The film is depicted as a quantum well (thick solid lines; the abscissa is the spatial extent normal to the sample surface, the ordinate is the energy E). The wave functions of a QWS and a QWR are schematically given by thin solid lines.

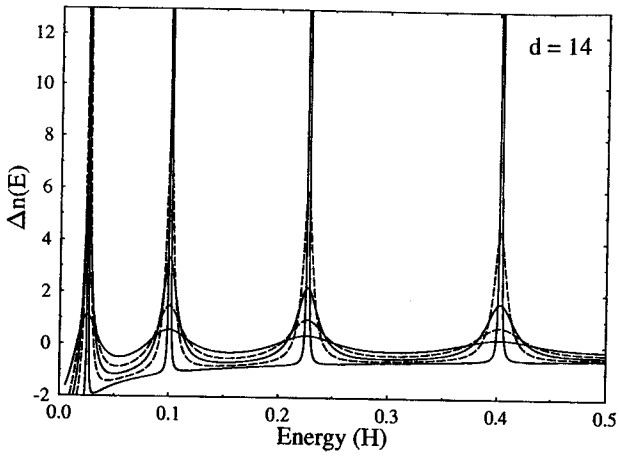

Fig. 23. Change of the density of states $\Delta n(E)$ due to confinement of a free electron to a rectangular quantum well, cf. Eq. (124), versus energy for confinement strengths $R = 0.2$, 0.4, 0.6, 0.8, and 0.99 (alternating solid and dashed lines). For a well thickness of $d = 14$, the maxima correspond to quantum-well states or resonances ($R < 1$).

The change of the DOS due to QWSs or QWRs can easily be computed for a rectangular quantum well [105]. A plane wave with $\mathbf{k}_\parallel = 0$ is reflected at the surface-side and the bulk-side boundary with reflection coefficients $R_s \exp(i\phi_s)$ and $R_i \exp(i\phi_i)$, respectively (R_s, $R_i \in \mathbb{R}$). The accumulated phase along a round trip, that is, reflection at a boundary, propagation, reflection at the other boundary, and once again propagation, is $\Delta\phi = 2kd + \phi_s + \phi_i$, with k being the wave number of the electron and d the thickness of the well. The change of the DOS $\Delta n(E)$ should be proportional to $\cos(\Delta\phi)$, the strength of the confinement $R = R_i R_s$, the thickness of the well d, and the unit DOS $2\partial_E k(E)/\pi$. For j round trips, one has to replace R by R^j and $\Delta\phi$ by $j\Delta\phi$. Thus, $\Delta n(E)$ is given by

$$\Delta n(E) = \frac{2d}{\pi}\left(\partial_E k(E)\right) \sum_{j=1}^{\infty} R^j \cos(j\Delta\phi) \qquad (123)$$

which, after some manipulation, can be written as

$$\Delta n(E) = \frac{2d}{\pi} \frac{R[\cos(\Delta\phi) - R]}{1 - 2R\cos(\Delta\phi) + R^2} \partial_E k(E) \qquad (124)$$

The important factor is the second one, which reflects the interference of the electron. The last term takes into account the electronic structure of the infinitely extended ("bulk") system. In Figure 23, $\Delta n(E)$ is shown for a free electron; that is, $\partial_E k(E) = 1/k(E)$. If the phase shift is a multiple of 2π, constructive interference leads to maxima in $\Delta n(E)$. These maxima are very sharp (quasi δ peaks) if R is close to 1 (cf. $R = 0.99$ in Fig. 23). If R is considerably small, as is expected for a QWR, $\Delta n(E)$ shows smooth oscillations that become broader with increasing energy. This behavior can be attributed to $\partial_E k(E)$.

As a prototypical system, we now address SPLEED from Co films on W(110) (for details, see [106]). Its layer-by-layer growth [107–110] allows for a study of the evolution of QWRs with increasing number n of Co layers. Note that initially a pseudomorphic body-centered cubic (bcc) (110) monolayer is formed, which upon further Co deposition becomes a monolayer with approximate hexagonally closed packed (hcp) structure. Subsequent layers grow in the form of hcp Co(0001). It is further important that the magnetization of the Co film is parallel to the surface for all film thicknesses ($\mathbf{M} \parallel [1\bar{1}00]$ of the hcp Co film).

Experimental. Although this chapter is mainly concerned with theory, some words on the experimental aspects are in order. To estimate the film thickness during the growth process, one monitors the Co evaporation rate, for example, by a quartz crystal oscillator. This procedure gives an accuracy of better than 2% in thickness calibration. Spectra were measured by means of a spin-polarized low-energy electron microscope (SPLEEM), which, for normal incidence ($\mathbf{k}_\parallel = 0$), allows for the observation of the specular reflected beam ($\mathbf{g} = 0$) from single ferromagnetic domains [111]. The illumination system produces an electron beam with spin polarization $\mathbf{P}^{\text{in}}$ perpendicular to the direction $\mathbf{k}$ of the beam, that is, parallel to the surface. Thus, in-plane magnetization $\mathbf{M}$ can be studied. The degree of polarization P^{in} was about 20%. Spectra were taken in remanence because even weak magnetic fields would deflect the low-energy electrons because of the Lorentz force.

Specular SPLEED intensities I_+ and I_- were recorded for $\mathbf{P}^{\text{in}}$ parallel and antiparallel to $\mathbf{M}$. As mentioned previously, minima in I_+ (I_-) directly reflect majority (minority) spin QWRs. The asymmetry $A^{\text{ex}} = (I_+ - I_-)/(I_+ + I_-)$ is identical to the exchange-induced asymmetry A^{ex} [cf. Eq. (122)], because in this highly symmetric setup effects due to SOC do not show up in an asymmetry, although they are present in nature.

Computational and Model Assumptions. Numerical calculations were performed within the framework of spin-polarized relativistic layer-KKR (SPRLKKR) theory for ferromagnetic systems consisting of arbitrary combinations of commensurate atomic monolayers, as briefly described in Section 3.2.3. The spin- and layer-resolved Bloch spectral function was obtained as the imaginary part of the Green function (see Section 4.2.3).

Because hcp Co films are incommensurate with the W(110) substrate, only the specular beam ($\mathbf{g} = 0$) is common to the beam sets of hcp Co(0001) and bcc W(110) [110]. However, the previous layer-KKR (LKKR) approach is applicable only to commensurate systems. Therefore, either the substrate plus pseudomorphic Co layers or a standalone hcp Co film, that is, a Co film without substrate, can be treated. The latter should be a reasonable approximation in the case of thicker films, but the influence of the substrate can certainly not be ignored in the case of a few monolayers (MLs) because of the mean free path (cf. Fig. 12). The effect of the substrate can be included in the following approximation: One calculates the total reflection matrix R^{tot} from semi-infinite W(110) without surface barrier. From this R^{tot}, the specular reflection coefficient R^{tot}_{00} is extracted and taken as the only nonvanishing element of the reflection matrix at the substrate side. To simulate lifetime effects, the imaginary part V_{i} of the optical potential was taken as energy dependent. Because a surface barrier of step shape is not appropriate for VLEED, a smooth JJJ form [91] was chosen.

Theoretical and Experimental Results. Numerical results of QWRs and their manifestation in SPLEED are presented in Figure 24 for 4-ML Co on W(110). First, the bulk-band structure above the vacuum level of hcp Co(0001) along the line Γ–A is addressed. Although in the presence of SOC bands of ferromagnets should be characterized with respect to magnetic double groups (cf. [112]), a classification in terms of nonmagnetic single groups and majority/minority spin remains useful in large parts of the band structure, in particular, those in parts where there are no bandgaps induced by SOC. Between 2.0 and 17.5 eV above the vacuum level (0 eV), there is a rather steep spin-split band that belongs to the Λ^1 representation, separated by a narrow gap at 17.5 eV from a flat band of the same representation. Further, there are fairly flat bands of dominant Λ^3 representation above 21 eV. The spin polarization expectation value for the majority (minority) bands departs from $+1$ (-1) only by a few hundredths, which indicates a negligible influence of SOC.

For each of the four Co monolayers, the Bloch spectral function for $\mathbf{k}_{\parallel} = 0$ (Fig. 24b) is seen to have four widely spaced pairs of majority and minority spin peaks between 2 and 17 eV, and four narrowly spaced pairs between 17 and 20 eV (the pair around 16.5 eV looks more like a shoulder because it is close to the strong peak at 17.5 eV). These two sets of Λ^1 QWRs are related to the steep and to the flat Λ^1 band, respectively. In Figure 24b, the first three pairs of QWRs are indicated by arrows, the $k_\perp$ values of which are shown in panel a. For the majority Λ^1 band, one finds $k_\perp$ values of 0.40 $2\pi/c$, 0.77 $2\pi/c$, and 0.76 $2\pi/c$, whereas for the minority band one finds 0.40 $2\pi/c$,

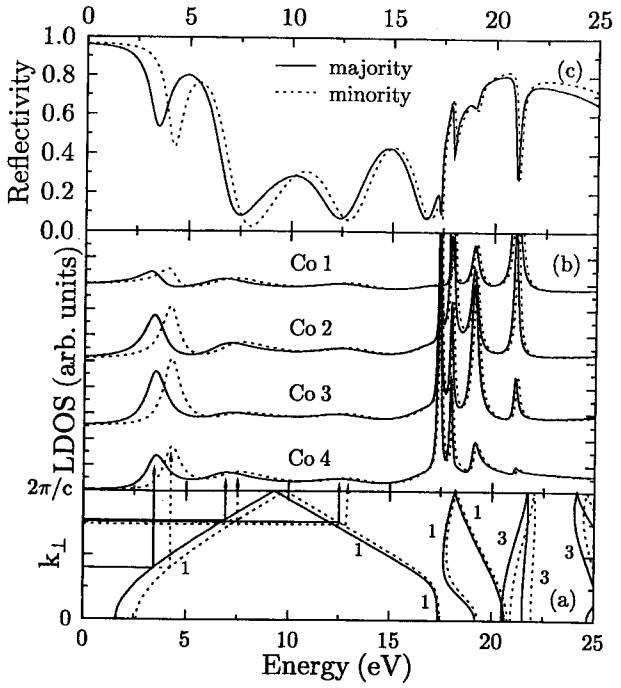

Fig. 24. Ferromagnetic hcp Co. (a) Bulk-band structure along [0001] with bands of mainly majority (solid lines) and minority spin (dashed lines) and dominant spatial representations Λ^1 and Λ^3 indicated by numbers 1 and 3. (b) Λ^1 contributions to the layer- and spin-resolved density of states (LDOS) for $\mathbf{k}_{\parallel} = 0$ of a 4-ML film of Co on W(110); solid and dashed lines indicate majority and minority spin, respectively; the first ML (Co 1) is at the surface, the fourth (Co 4) adjacent to the substrate. (c) SPLEED from 4-ML Co on W(110): spin-dependent intensity versus energy curves I_+ (solid) and I_- (dashed) of the specular beam for normal incidence, calculated with the same lifetime broadening $V_{\text{i}} = 0.05$ eV as in (b). The quantum-well resonances are indicated by arrows in (b); see text. The vacuum level is 0 eV. Reprinted with permission from T. Scheunemann, R. Feder, J. Henk, E. Bauer, T. Duden, H. Pinkvos, H. Poppa, and K. Wurm, *Solid State Commun.* 104, 787 (1999). Copyright 1997, by Elsevier Science.

0.77 $2\pi/c$, and 0.74 $2\pi/c$ (note that all bands are back-folded at the Brillouin zone boundary $k_\perp = 2\pi/c$). According to the theories presented in Section 2.2, these values nicely coincide with those obtained from Eq. (20) with $a = 5c/4$. Because the substrate is nonmagnetic, the reflection properties at the Co/W interface are identical for spin-up and spin-down electrons. Therefore, one would expect the same $k_\perp$ for majority and minority QWRs, as can be observed from Figure 24. The small differences in $k_\perp$ can be attributed to the different energies of majority, and minority QWRs, which are due to the spin-dependent potential within the Co film; cf. Eq. (81).

Decomposition of the Bloch spectral function according to angular momenta reveals that the first set of resonances, that is, those QWRs below 17.5 eV, has comparable s, p, d, and higher contributions, whereas in the second set the d and higher contributions far outweigh the s and p parts. The exchange splitting is largest for the pair around 3 eV and decreases with increasing energy. The difference between the local density of states (LDOS) of the first layer and that of the fourth is due to the fact that the film is bounded by vacuum on one side and by W(110) on the other. Because of their Λ^1 representation, the

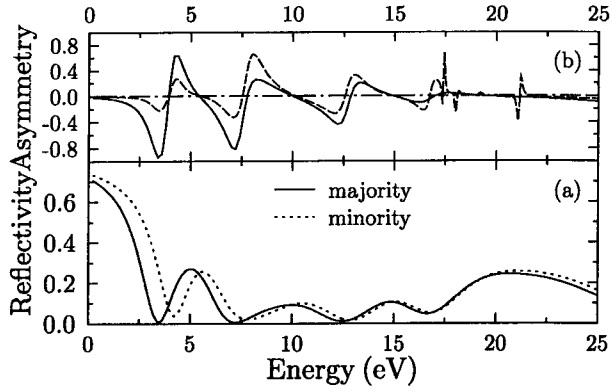

Fig. 25. Ferromagnetic hcp Co: (a) Same as Figure 24c, but calculated with the larger energy-dependent lifetime broadening V_i. (b) SPLEED asymmetry $A = (I_+ - I_-)/(I_+ + I_-)$ obtained from the intensities $I_\pm$ in panels (c) in Figure 24 (dashed line) and (a) (solid line). Reprinted with permission from T. Scheunemann, R. Feder, J. Henk, E. Bauer, T. Duden, H. Pinkvos, H. Poppa, and K. Wurm, *Solid State Commun.* 104, 787 (1997). Copyright 1997, by Elsevier Science.

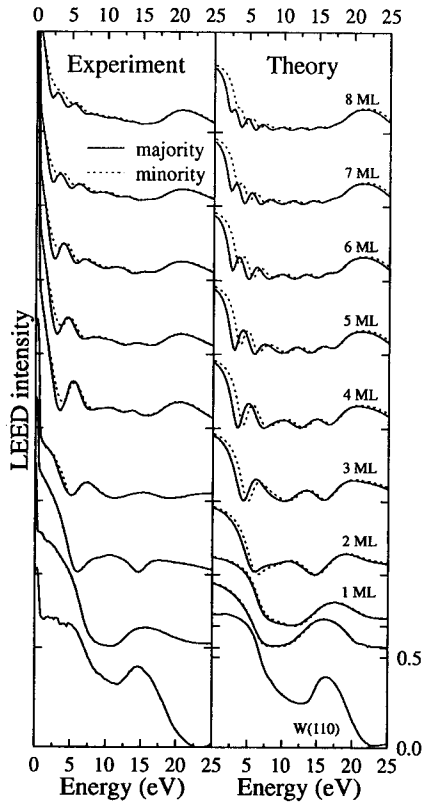

Fig. 26. Spin-polarized low-energy electron diffraction from clean W(110) and from n-ML ferromagnetic Co on W(110) with $n = 1, \ldots, 8$ as indicated: spin-dependent intensity versus energy curves I_+ (solid) and I_- (dashed) of the specular beam for normal incidence. Experiment (left panel) and theory (right panel). For 1-ML Co, the lower pair of curves was obtained for a pseudomorphic overlayer with Co atoms in bulklike W positions, the upper pair for an incommensurate overlayer with the lateral geometry of hcp Co(0001). The tick mark below each curve indicates its zero line. The intensities are normalized to the primary beam intensity, with the distance between 0 and 0.5 at the bottom of the right panel giving the scale. Reprinted with permission from T. Scheunemann, R. Feder, J. Henk, E. Bauer, T. Duden, H. Pinkvos, H. Poppa, and K. Wurm, *Solid State Commun.* 104, 787 (1997). Copyright 1997, by Elsevier Science.

resonances can couple to scattering solutions outside the film and thus become observable by SPLEED, as mentioned previously. In contrast, the two sets of four LDOS peaks associated with the Λ^3 bands above 20 eV correspond to QWRs that cannot be accessed from the vacuum side for $\mathbf{k}_\parallel = 0$.

We now proceed to specular-beam SPLEED spectra I_+ (majority) and I_- (minority) for normal incidence. The incoming electrons are fully polarized parallel and antiparallel to the majority spin direction of the Co film. Figure 24c shows SPLEED spectra that were calculated with the same lifetime broadening as the Bloch spectral function; for example, the imaginary part of the optical potential was chosen as $V_i = 0.05$ eV. The most important features of the I_+/I_- pair are broad valleys between 2 and 17 eV and four pairs of narrow dips between 17 and 22 eV. All these minima occur exactly at the energies of QWRs, which establishes the one-to-one correspondence between SPLEED minima and QWRs.

To come closer to experiment, the lifetime broadening V_i was increased, as shown in Figure 25. The larger energy-dependent V_i, which is on the order of 2 eV, leads to broader maxima in the $I_\pm(E)$ spectra, as has been demonstrated by means of a model calculation (Fig. 15). For example, the sharp minima between 17 and 20 eV are completely smeared out. The fingerprints of the QWRs between 2 and 17 eV are thus preserved, whereas those of the resonances above 17 eV are obscured by lifetime effects. Compared to Figure 24c, the first two valleys are only slightly broader, but significantly deeper. The latter is plausible because, roughly speaking, "more electrons disappear" in inelastic channels inside the solid and are consequently missing in the elastically reflected channel. In the exchange-induced asymmetry $A^{ex} = (I_+ - I_-)/(I_+ + I_-)$, shown in panel b, the exchange-split QWRs manifest themselves as pronounced $-/+$ features.

In Figure 26, experimental and calculated SPLEED spectra Co films on W(110) with 0 ML to 8 ML thickness are shown. Note that the spectra for uncovered W(110) are not spin dependent because of the high symmetry of the normal-incidence geometry and the absence of ferromagnetism. For 1-ML Co on W(110), the measured spectrum is, in contrast to the calculated one, still spin independent. This may be explained by a Curie temperature T_C below room temperature, at which the data were taken. For example, a 2-ML Co film on Cu(001) shows T_C of about 320 K compared to a bulk value of 1388 K [113]. Another reason might be perpendicular magnetization, which cannot be detected by SPLEED with incoming electrons polarized parallel to the surface. The similarity of the measured 1-ML spectrum to the spectrum for uncovered W and its agreement with the 1-ML spectrum calculated for Co in W sites indicates pseudomorphic growth of the first Co monolayer. In the theoretical spectrum for an incommensurate monolayer with the lateral geometry of hcp Co(0001), the second peak is shifted upward by about 2 eV. The rather broad minimum between 7.5 and 12.5 eV is associated with a QWR.

With increasing number n of Co monolayers, the calculated spectra in Figure 26 show a systematic evolution of the minima,

that is, the signatures of the QWRs, the number of the latter being equal to n. Comparing with experiment, one notices good agreement for 2 and 4 ML. For 3 ML, the experimental spectrum duly exhibits three minima but the third one is higher in energy and so is the subsequent peak. On the grounds of the evolution of the calculated spectra with thickness n, the experimental data for 3 ML indicate a surface morphology other than three hcp monolayers. From 5 ML upward, the experimental spectra differ from theory by having only $n-1$ minima instead of n. It is, however, striking that the experimental curves for 6, 7, and 8 ML are in good agreement with the calculated ones for 5, 6, and 7 ML, respectively.

The preceding theoretical and experimental results show that the electronic structure of ultra-thin films at energies above the vacuum level can comprise pairs of exchange-split QWRs. The calculated as well as the experimental SPLEED spectra have minima, which exactly coincide in energy with maxima in the Bloch spectral function of the same spin and the same spatial representation.

4. PHOTOELECTRON SPECTROSCOPY

4.1. Introduction and History

The first publications on the photoelectric effect appeared in the 19th century (for detailed coverage of the history of photoelectron spectroscopy (PES), see [114]). In 1887, Hertz discovered that a discharge between metal plates (electrodes) occurs at a lesser voltage than usual if the cathodes are illuminated by ultraviolet light [115]. One year later, Hallwachs found that a negatively charged metal plate connected to an electroscope becomes discharged if illuminated. A positively charged metal plate, however, remains charged [116]. These findings led to intensive experimental work, for example, by Elster and Geitel [117, 118] as well as Lenard [119]. The latter observed that irradiated metals send electrons into their surroundings. The velocity of the photoelectrons, however, does not depend on the intensity of the incoming radiation, but the number of electrons increases with light intensity. These observations could not be explained within classical theories. In 1905, Einstein explained, following Planck's ideas, the photoelectrical effect by quanta of the electromagnetic radiation, that is, by photons [120]. For this he achieved the Nobel Prize in 1919.

Because of the comparably large experimental effort, it took considerable time to use the photoelectric effect as a spectroscopic method. Siegbahn used X-rays to determine the electronic structure of the inner shells of atoms [121], a method first termed electron spectroscopy for chemical analysis (ESCA) and nowadays better known as X-ray photoelectron spectroscopy (XPS). Using light in the ultraviolet regime, which can be produced by rare-gas discharge lamps, instead of X-rays and using angle-resolved detection of the photoelectrons instead of angle-integrated detection allowed for the determination of the valence-band structure of solids [122]. As in LEED, surface sensitivity plays an important role: The detected photoelectrons

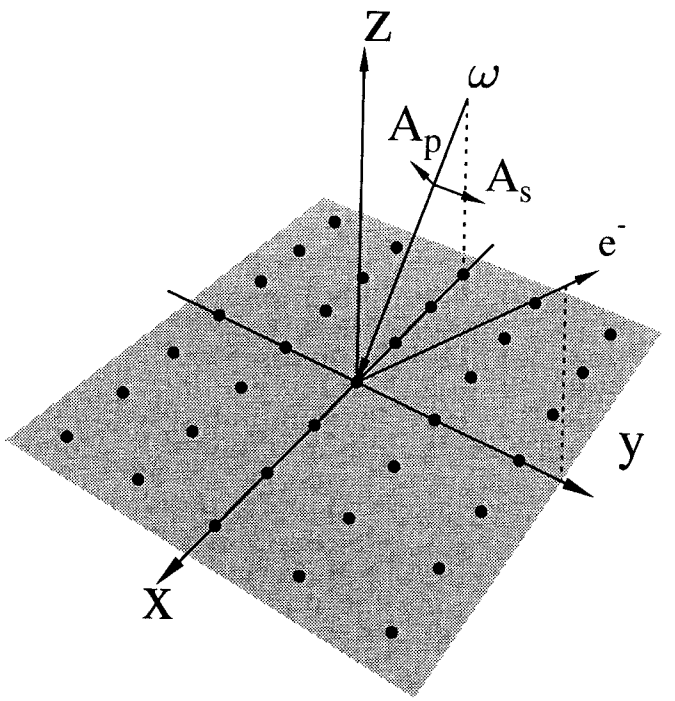

Fig. 27. Setup of photoemission. Light with photon energy ω impinges on the solid surface (gray area, with dots representing surface atoms). Its polarization components are denoted A_s and A_p, the photoelectrons as e^-.

have their origin in the first few layers of the solid and, therefore, the spectra contain contributions from both the surface and the bulk. A considerable impact on the development of angle-resolved photoelectron spectroscopy (ARPES) or, as commonly but less accurately named, photoemission was obtained by synchrotron radiation facilities [123–125]. These allow the use of photon energies from the vacuum-ultraviolet (VUV) to the X-ray regime. Further, they provide both circularly and linearly polarized light, which can be used to determine the symmetry of electronic states via dipole selection rules.

Figure 27 shows a rather typical setup of a photoemission experiment [6, p. 73]. The incoming light is characterized by the incidence direction, the photon energy ω, and its polarization. The latter is described by the components of the electrical-field vector $\mathbf{A}$ with components $\mathbf{A}_p$ and $\mathbf{A}_s$ lying parallel and perpendicular[14] to the plane of incidence, which is spanned by the surface normal and the incidence direction (xz plane in Fig. 27), respectively. A list of commonly used light polarizations is given in Table II. The electrons (e^- in Fig. 27) are detected with respect to their kinetic energy, their outgoing direction (angle-resolved photoemission), and their spin (spin-resolved photoemission).

In an energy diagram (Fig. 28), photoemission can be regarded as a three-step process [126]. In the initial stage, the electronic states are occupied up to the Fermi level E_F. The incoming photon with energy ω excites one electron into an unoccupied state with energy larger than E_F. The latter then propagates toward the surface. If the electron energy is larger

[14] Historically, s stands for German *senkrecht*, that is, perpendicular.

Table II. Light Polarization in Photoemission

Polarization	A_s	A_p	Remark
s	1	0	Linear
p	0	1	Linear
σ_+	1	i	Right-handed circular
σ_-	1	$-i$	Left-handed circular

Note: The components A_s and A_p of the electrical-field vector are given for both linearly and circularly polarized light. Unpolarized light is an incoherent superposition of either s- and p-polarized or left- and right-handed circularly polarized light.

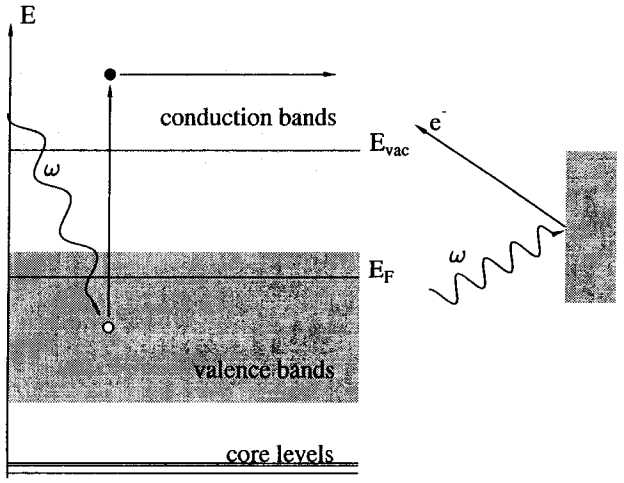

Fig. 28. Energy scheme of photoemission. Right panel: Incident light with photon energy ω, represented by the wavy line, impinges on the solid surface (gray area, right) and outgoing electrons e^- leave the solid. Left panel: An electron (filled circle) is excited into a state above the vacuum level E_{vac}, leaving behind a hole (empty circle) below the Fermi energy E_F. The electron, which stems either from the valence-band (gray area) or from the core-level (horizontal lines) regime, leaves the solid and is subsequently detected.

than the vacuum level E_{vac}, the photoelectron can leave the solid and propagate toward the detector, leaving behind the solid with one hole. The energy difference between E_{vac} and E_F is the work function Φ, typically about 5 eV.

There are three main modes in photoemission: (i) The most commonly used is the energy distribution curve (EDC) mode in which the photon energy is kept constant. Therefore, variation of the kinetic energy of the photoelectrons corresponds to a variation in the initial-state energy (cf. Fig. 29). (ii) In constant initial-state (CIS) mode, both the photon energy and the kinetic energy are varied in such a way that the energy of the initial state remains constant. (iii) In constant final-state (CFS) mode, the kinetic energy is kept fixed and the photon energy is varied. This leads to a variation in the initial-state energy. Because CIS and CFS require variable photon energy, they are not possible with laboratory rare-gas discharge lamps, which provide only fixed photon energies, for example, $\omega = 21.22$ eV from He(I) discharge.

A simple theoretical description of the process uses Fermi's golden rule. The transition probability w_{fi} between the initial state $|\Psi_i\rangle$ with energy E_i and the final state $|\Phi(\mathbf{k}_\parallel, E_f)\rangle$ with

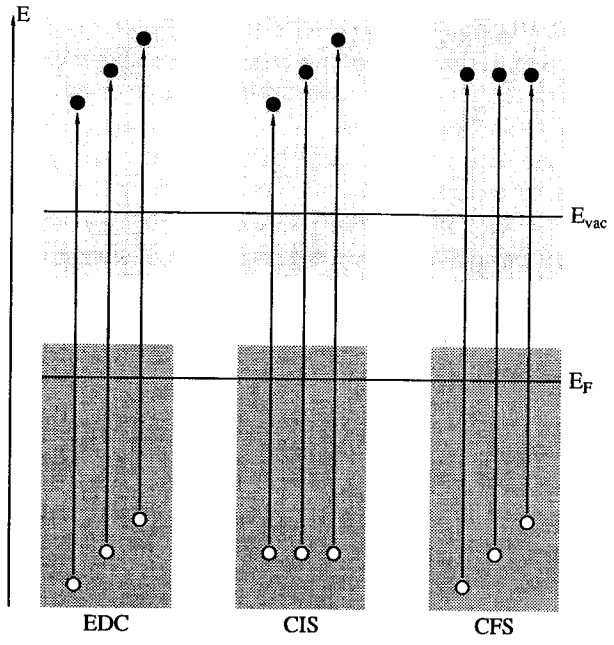

Fig. 29. Energy modes of photoemission. In energy distribution curve (EDC) mode (left), the kinetic energy of the photoelectrons (black circles) is varied while keeping the photonenergy constant. In constant initial-state (CIS) mode (middle), the energy of the initial state (hole, white circles) is kept constant while the photon energy is varied, which, in turn, leads to variable kinetic energies. In constant final-state (CFS) mode (right), the kinetic energy is kept fixed while the photon energy is varied. The Fermi energy is E_F, the vacuum level E_{vac}.

energy $E_f = E_i + \omega$ and surface-parallel momentum $\mathbf{k}_\parallel$ is given by

$$w_{fi} = \left|\langle\Phi(\mathbf{k}_\parallel, E_f)|D|\Psi_i\rangle\right|^2 \delta(E_f - E_i + \omega) \qquad (125)$$

The transition is mediated by the dipole operator D, which can be approximated as $\mathbf{A} \cdot \mathbf{p}$, with $\mathbf{p}$ denoting the momentum operator and $\mathbf{A}$ the vector potential of the incident light. The photocurrent j for kinetic energy E_{kin} and $\mathbf{k}_\parallel$ of the photoelectrons is then given by

$$j \sim \sqrt{E_{kin}} \sum_i w_{fi} \qquad (126)$$

The electron detection angles ϑ_e and φ_e as well as the kinetic energy determine the surface-parallel momentum $\mathbf{k}_\parallel$,

$$\mathbf{k}_\parallel = \sqrt{2E_{kin}} \begin{pmatrix} \cos\varphi_e \\ \sin\varphi_e \end{pmatrix} \sin\vartheta_e \qquad (127)$$

One of the most successful methods for the analysis of electronic states in the valence regime is angle-resolved photoemission using VUV light (for reviews on ARPES, see [114, 127–129]). For fixed photoelectron detection angles, the experimentally obtained intensity maxima disperse in binding energy with photon energy. The interpretation of this behavior is usually based on the very popular and successful direct-transition approximation, which relates the energy position of the intensity maxima to the bulk-band structure $E(\mathbf{k})$. This relies on the assumption that the wave vector $\mathbf{k}$ is conserved in the excitation process. A survey of the theoretical aspects is given next.

4.2. Theory

4.2.1. Historical Sketch

First, a few milestones of photoemission theory will be sketched, without claim of completeness. In 1964, Adawi showed within scattering theory that the final state $|\Phi\rangle$ can be described by an incoming plane wave [130]. Mahan addressed the angular distribution of the photoelectrons and pointed out that the results obtained via Green functions and via quadratic response are equivalent [131, 132]. Regarding surface sensitivity, model calculations by Schaich and Ashcroft yielded that the photoeffect at the surface and in the bulk can be of the same order of magnitude [133]. Langreth determined the scattering of the photoelectrons versus several parameters, in particular, the escape depth [134]. Because of the similarity of some aspects of LEED and photoemission, in particular, the state of the photoelectron, several works based on LEED theory were published. Especially, multiple scattering of the outgoing electrons was treated by Pendry [135]. Taking into account all ingredients of photoemission theory, for example, band structures, transition-matrix elements, scattering, and surface effects, Pendry developed a dynamical theory that eventually led to the PEOVER computer program [136, 137].

Relativistic effects were considered by Ackermann and Feder [83] as well as by Borstel's group [138–140]. The latter addressed, in particular, optical orientation, that is, the alignment of the photoelectron's spin parallel or antiparallel to the helicity of the incoming circularly polarized light [141]. In a series of publications, Feder's group predicted that the photoelectron shows a spin polarization even in the case of linearly polarized light [142–144] (see also [145]). All their predictions were fully confirmed experimentally [146–148].

In addition, multiple-scattering theories for ferromagnets [149] found entrance into the photoemission theories (for an overview, see [51]). Relativistic theories for spin-polarized systems, in particular, spin-polarized relativistic layer-KKR (SPRLKKR), proved to be successful in the explanation of magnetic dichroism in photoemission, that is, the change of the photocurrent due to reversal of the magnetization direction by an otherwise fixed setup [150]. This allowed for a detailed understanding of the electronic structure of ferromagnets, in particular, the delicate interplay of spin-orbit coupling (SOC) and exchange [151–153]. Further, multiple-scattering theory allows for the treatment of disorder, for example, substitutional alloys [154]. This can also be used to describe photoemission from ferromagnets at elevated temperatures [155].

In the following, we portray the photoemission formalism as derived by Feibelman and Eastman [156], which can be seen as the basis of most, if not all, applied photoemission theories today.

4.2.2. Formalism of Photoemission

The nonrelativistic theory of Feibelman and Eastman [156] is based on the work of Caroli et al. [157] who applied Keldysh's Green function formalism for nonequilibrium systems. Consider a semiinfinite solid, the electrons of which are assumed independent. Monochromatic light with vector potential $\mathbf{A}(\mathbf{r}, t) = \mathbf{A}_0(\mathbf{r})\cos(\omega t)$ impinges on this solid. The Hamiltonian of the entire system is then given by

$$H(t) = \frac{1}{2}\left(\mathbf{p} + \frac{1}{c}\mathbf{A}(\mathbf{r}, t)\right)^2 + V(\mathbf{r}) \tag{128}$$

where $V(\mathbf{r})$ is the crystal potential. We separate $H(t)$ into the time-independent reference Hamiltonian H_0 and the time-dependent perturbation $H_1(t)$, $H(t) = H_0 + H_1(t)$ with

$$H_0 = \frac{\mathbf{p}^2}{2} + V(\mathbf{r}) \tag{129a}$$

$$H_1(t) = \frac{1}{2c}[\mathbf{p}\cdot\mathbf{A}(\mathbf{r}, t) + \mathbf{A}(\mathbf{r}, t)\cdot\mathbf{p}] + \frac{\mathbf{A}(\mathbf{r}, t)^2}{2c^2} \tag{129b}$$

The eigenstates of H_0 form a complete set and obey $H_0|n\rangle = E_n|n\rangle$. Our task is to calculate the current density $\mathbf{j}$, which is due to a state $|\Psi\rangle$ at the detector position $\mathbf{R}$,

$$\langle\Psi|\mathbf{j}(\mathbf{R})|\Psi\rangle = \frac{i}{2}(\Psi^*\nabla\Psi - \Psi\nabla\Psi^*)_{\mathbf{R}} \tag{130}$$

where the expectation value is evaluated at $\mathbf{R}$. Following time-dependent perturbation theory, $H_1(t)$ is adiabatically switched on. For the time development of an eigenstate $|n\rangle$, one has in first order

$$|\Psi_{nI}(t)\rangle = |n\rangle - i\int_{-\infty}^{t} H_{1I}(t')|n\rangle\, dt' \tag{131}$$

where the subscript I denotes the interaction picture. The contribution of state $|n\rangle$ to the current density,

$$\langle\mathbf{j}_n(\mathbf{R})\rangle = \langle\Psi_{nI}(t)|\mathbf{j}_I(\mathbf{R}, t)|\Psi_{nI}(t)\rangle \tag{132}$$

is straightforward with the following considerations: (i) The diamagnetic term of the dipole operator, $\mathbf{A}^2/(2c^2)$, is neglected. (ii) Terms in which the current density operator acts on bound states give no contribution to $\mathbf{j}(\mathbf{R})$ because these electrons cannot leave the solid. (iii) Translating the dipole operator from the interaction picture into the Schrödinger picture yields exactly one term, which corresponds to the excitation of $|n\rangle$ into a state with energy $E_n + \omega$. In summary, one arrives at

$$\langle\mathbf{j}_n(\mathbf{R})\rangle = \langle n|OG^a(E_n + \omega)\mathbf{j}(\mathbf{R})G^r(E_n + \omega)O|n\rangle \tag{133}$$

with $O = (\mathbf{p}\cdot\mathbf{A}_0 + \mathbf{A}_0\cdot\mathbf{p})/2c$ and advanced (G^a) as well as retarded (G^r) Green functions

$$G^a(E) = \sum_m \frac{|m\rangle\langle m|}{E - E_m - i\eta} \tag{134a}$$

$$G^r(E) = \sum_m \frac{|m\rangle\langle m|}{E - E_m + i\eta} \tag{134b}$$

($\eta > 0$). Inserting Eq. (130) into Eq. (133) and introducing the nonlocal spectral density

$$G^+(E) = 2\pi i\sum_n |n\rangle\langle n|\delta(E - E_n) \tag{135}$$

one eventually obtains

$$R^2\langle j(\mathbf{R})\rangle = -\frac{K}{32\pi^2 c^2}\langle\Phi^*(E+\omega)|\Delta \operatorname{Im} G^+(E)\Delta^\dagger|\Phi^*(E+\omega)\rangle \tag{136}$$

$K = \sqrt{2(E+\omega)}$ is the momentum of the photoelectron. The time-reversed final state $|\Phi\rangle$ fulfills

$$\Phi(\mathbf{r}, E+\omega) = \exp(i\mathbf{K}\cdot\mathbf{r}) + \int dr' G^r(\mathbf{r}, \mathbf{r}'; E+\omega)V(\mathbf{r}') \times \exp(i\mathbf{K}\cdot\mathbf{r}') \tag{137}$$

which establishes the connection of photoemission with LEED. First, $|\Phi\rangle$ is a superposition of an incoming plane wave, the first term in Eq. (137), and outgoing waves. The latter are represented by the integral in Eq. (137), which gives nonzero contributions only inside the crystal, in particular, where $V(\mathbf{r}') \neq 0$. The retarded Green function propagates electrons from the interior of the solid ($\mathbf{r}'$) to the vacuum region ($\mathbf{r}$). Therefore, the integral can be regarded as giving rise to reflected beams in vacuum. In short, $|\Phi\rangle$ is a state suitable for the description of a LEED experiment. $|\Phi^*\rangle$ is known as a time-reversed LEED state.

As a last step, we observe that the final state can be written as $|\Phi^*\rangle = G^r(E+\omega)|\Phi_0^*\rangle$ where $|\Phi_0^*\rangle$ is the plane wave at the detector position. The expression for the photocurrent then eventually reads

$$j \sim -\langle\Phi_0^*|G^a(E+\omega)\Delta \operatorname{Im} G^+(E)\Delta^\dagger G^r(E+\omega)|\Phi_0^*\rangle \tag{138}$$

Equation (138) can be represented by the Feynman diagram shown in Figure 30. Its interpretation is straightforward if Eq. (138) is read from the right. First, the photoelectron state $|\Phi_0^*\rangle$ with energy $E+\omega$ is propagated by the retarded Green function G^r from the detector to the interior of the solid. Subsequently, the dipole operator $\Delta^\dagger$ mediates a deexcitation to initial states with energy E, which are described by the nonlocal density of states, $\operatorname{Im} G^+$. These are excited into the outgoing photoelectron state $\langle\Phi_0^*|G^a$ by the dipole operator Δ. The diagram in Figure 30 is that of lowest order. Higher order diagrams include, for example, the (screened) Coulomb interaction between the final and the initial states, that is, scattering between the photoelectron and the remaining hole. These terms are, for instance, essential for the description of the resonant behavior of photoemission intensities from Pd [158]. Usually, one neglects higher order terms; that is, one assumes the sudden approximation [159–161].

Applying the Dirac identity,

$$\lim_{\eta\to 0^+}\frac{1}{x \pm i\eta} = \mathcal{P}\left(\frac{1}{x}\right) \mp i\delta(x) \tag{139}$$

which establishes for any state $|\Xi\rangle$ the relation [cf. Eq. (134); $\mathcal{P}$ stands for principal value]

$$\operatorname{Im}\langle\Xi|G(E+i\eta)|\Xi\rangle = -\pi\sum_m |\langle\Xi|m\rangle|^2\delta(E-E_m) \tag{140}$$

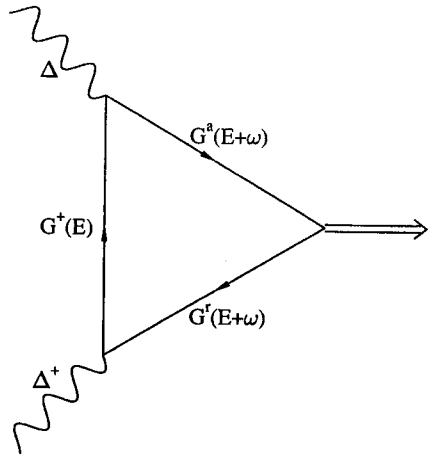

Fig. 30. Feynman diagram of photoemission according to Eq. (138). The double line represents the detected state $|\Phi_0^*\rangle$ with energy $E+\omega$ and surface-parallel momentum $\mathbf{k}_\parallel$. Green functions G^a, G^r, and G^+ are represented by arrow-decorated lines, photons by wavy lines.

the photocurrent can be expressed in golden-rule form,

$$j \sim \sum_m |\langle\Phi^*(E+\omega)|\Delta|m\rangle|^2\delta(E+\omega-E_m) \tag{141}$$

The main difference between the golden-rule and the Green function expression, Eq. (138), is that the former holds only for real energies, whereas the latter can also be applied for complex energies. In other words, the golden rule is only valid for infinite lifetimes, whereas the Green function takes into account finite lifetimes of both photoelectrons and holes.

The description of electron scattering in a many-body theory leads to quasi-particle states and to the self-energy Σ, sometimes denoted optical potential [162]. In the lowest order approximation, the self-energy is local and homogeneous. Its real part gives rise to shifts of the quasi-particle energies. For example, fundamental bandgaps obtained from density-functional calculations for zinc-blende semiconductors are too small with respect to the experimental values; inclusion of Σ in the GW approximation [163] increases the bandgaps considerably. Another example is Ni where the experimental energy shift between spin-split bands is about 0.3 eV, in comparison to 0.6 eV from density-functional calculations [164]. The imaginary part of Σ accounts for the lifetime of the quasi-particles; that is, an increase of $\operatorname{Im}\Sigma$ leads to broader photoemission spectra [165, 166]. This can be attributed to the spectral function $A(E) = -\operatorname{Im}\operatorname{Tr} G(\mathbf{r}, \mathbf{r}; E)/\pi$,

$$A(E) = \sum_m \begin{cases} \delta(E-E_m) \\ \quad \text{real energies} \\ \dfrac{\Gamma}{\pi}\dfrac{1}{(E-E_m)^2+\Gamma^2} \\ \quad \text{complex energies} \\ \dfrac{\operatorname{Im}\Sigma(E_m)}{(E-E_m-\operatorname{Re}\Sigma(E_m))^2+(\operatorname{Im}\Sigma(E_m))^2} \\ \quad \text{general case} \end{cases} \tag{142}$$

4.2.3. *Formulation within Multiple-Scattering Theory*

As we have seen in Section 3, multiple-scattering theory provides an excellent description of the LEED process. In the previous, we have further established a close connection between LEED and photoemission; in particular, the final state in photoemission is a time-reversed LEED state. Guided by these findings, photoemission should also nicely be described in terms of multiple-scattering theory. Instead of sketching Pendry's formulation [136, 167], which provides a very fast algorithm (in terms of computational time) but a rather technical theoretical description, we present a formulation in terms of Green functions. Of course, both methods give identical results.

In the formulation of the LKKR method for LEED, we have obtained the scattering properties of the entire semi-infinite system by consecutively treating the scattering of smaller entities: the single-site t matrix for scattering from atoms, the M and Q matrices for layers, and from these eventually the reflection matrix of the semi-infinite solid. This idea appears again in the calculation of the Green function. We shall start with the Green function of free space, then treat an empty layer embedded in the otherwise occupied system, and eventually treat a full layer.

Before turning to the investigation of the Green function, we sketch the very basis of multiple-scattering theory, the Lippmann–Schwinger equation and the Dyson equation.

Lippmann–Schwinger and Dyson Equations. Consider an eigenstate $|\Phi^0\rangle$ of a reference Hamiltonian H^0, $H^0|\Phi^0\rangle = E|\Phi^0\rangle$. The associated Green function G^0 fulfills $(z - H^0) \times G^0 = 1$, with $z = E + i\eta$, $\eta = 0^+$. The eigenfunction $|\Phi\rangle$ of the Hamiltonian $H = H^0 + V$, V being the perturbation, fulfills $H|\Phi\rangle = E|\Phi\rangle$ and can be obtained via the Lippmann–Schwinger equation

$$|\Phi\rangle = |\Phi^0\rangle + G^0 V|\Phi\rangle \tag{143}$$

Solving for $|\Phi\rangle$ yields formally $|\Phi\rangle = (1 - G^0V)^{-1}|\Phi^0\rangle$. Introducing the transition operator $T = V(1 - G^0V)^{-1}$ gives $V|\Phi\rangle = T|\Phi^0\rangle$, and $|\Phi\rangle = (1 + G^0T)|\Phi^0\rangle$.

The Dyson equation for the Green function G with $(z-H)\times G = 1$ can be obtained from $(z - H^0)G = 1 + VG$,

$$G = G^0 + G^0VG = G^0 + GVG^0 \tag{144}$$

Or, in terms of T, $G = G^0 + G^0TG^0$, which immediately gives $VG = TG^0$. This result can also be used for the wave function $|\Phi\rangle$, $|\Phi\rangle = |\Phi^0\rangle + GV|\Phi^0\rangle$.

Free-Space Solutions. We recall briefly basic properties of the solutions of the free-space Dirac equation for a given complex energy E. Because in this case the Hamiltonian is no longer hermitian, one has to deal with left-hand side (superscript L) and right-hand side (superscript R) wave functions [168]. The former obey $\langle\Psi^L|H = E\langle\Psi^L|$, the latter $H|\Psi^R\rangle = E|\Psi^R\rangle$. In general, the l.h.s. solutions are not the hermitian conjugate of the r.h.s. solutions. In plane wave representation, the free-space solutions [$V(\mathbf{r}) = 0$] read [76]

$$\langle\mathbf{r}|f^R_{\mathbf{k}\tau}\rangle = \sqrt{\frac{E+c^2}{2c^2}}\begin{pmatrix}\chi^\tau \\ \dfrac{c\sigma\cdot\mathbf{k}}{E+c^2}\chi^\tau\end{pmatrix}\exp(i\mathbf{k}\cdot\mathbf{r}) \tag{145}$$

and

$$\langle f^L_{\mathbf{k}\tau}|\mathbf{r}\rangle = \sqrt{\frac{E+c^2}{2c^2}}\left((\chi^\tau)^T, (\chi^\tau)^T\frac{c\sigma\cdot\mathbf{k}}{E+c^2}\right)\exp(-i\mathbf{k}\cdot\mathbf{r}) \tag{146}$$

In angular-momentum representation, they are given by

$$\langle\mathbf{r}|z^R_\Lambda\rangle = \sqrt{\frac{E+c^2}{2c^2}}\begin{pmatrix} z_l(kr)(\hat{\mathbf{r}}|\chi_\Lambda) \\ \dfrac{ickS_\kappa}{E+c^2}z_{\bar{l}}(kr)(\hat{\mathbf{r}}|\chi_{\bar{\Lambda}})\end{pmatrix} \tag{147}$$

and

$$\langle z^L_\Lambda|\mathbf{r}\rangle = \sqrt{\frac{E+c^2}{2c^2}}\left(z_l(kr)(\chi_\Lambda|\hat{\mathbf{r}}), \frac{-ickS_\kappa}{E+c^2}z_{\bar{l}}(kr)(\chi_{\bar{\Lambda}}|\hat{\mathbf{r}})\right) \tag{148}$$

with $z = j$ for regular or $z = h$ for irregular solutions. The wave number k is $\sqrt{E^2 - c^4}/c$. Each representation can be transformed into the other by

$$\langle\mathbf{r}|f^R_{\mathbf{k}\tau}\rangle = \sum_\Lambda \langle\mathbf{r}|j^R_\Lambda\rangle a_{\Lambda\tau}(\hat{\mathbf{k}}) \tag{149}$$

with $a_{\Lambda\tau}(\hat{\mathbf{k}})$ from Eq. (98).

Free-Electron Green Function. The retarded Green function of free space obeys the Dirac equation

$$(E - H)G^+_0(\mathbf{r}, \mathbf{r}'; E) = \begin{pmatrix}1 & 0\\ 0 & 1\end{pmatrix}\delta(\mathbf{r} - \mathbf{r}')\otimes\delta_{\text{spin}} \tag{150}$$

with the Hamiltonian $H = c\alpha\cdot\mathbf{p} + c^2\beta$ and $V(\mathbf{r}) = 0$. δ_{spin} denotes the Kronecker δ in spin space, $\delta_{\text{spin}} = \sum_{\tau=\pm}\chi^\tau(\chi^\tau)^T$. For given energy E and wave vector $\mathbf{k}_\parallel$, G^+_0 is given in plane wave representation by

$$G^+_0(\mathbf{r}, \mathbf{r}') = \frac{1}{iF_A}\sum_{\mathbf{g}\tau}\frac{1}{k_{\mathbf{g}\perp}}\begin{cases}\langle\mathbf{r}|f^R_{\mathbf{k}^+_{\mathbf{g}}\tau}\rangle\langle f^L_{\mathbf{k}^+_{\mathbf{g}}\tau}|\mathbf{r}'\rangle & z > z' \\ \langle\mathbf{r}|f^R_{\mathbf{k}^-_{\mathbf{g}}\tau}\rangle\langle f^L_{\mathbf{k}^-_{\mathbf{g}}\tau}|\mathbf{r}'\rangle & z < z'\end{cases} \tag{151}$$

$\mathbf{k}^\pm_{\mathbf{g}}$ is taken from Eq. (94) and the $+$ ($-$) sign refers to the case $z > z'$ ($z < z'$). F_A is the area of the two-dimensional layer unit cell. In angular-momentum representation, $G^+_0(\mathbf{r}, \mathbf{r}')$ reads

$$G^+_0(\mathbf{r}, \mathbf{r}') = -ik\sum_\Lambda\begin{cases}\langle\mathbf{r}|j^R_\Lambda\rangle\langle h^L_\Lambda|\mathbf{r}'\rangle & r < r' \\ \langle\mathbf{r}|h^R_\Lambda\rangle\langle j^L_\Lambda|\mathbf{r}'\rangle & r > r'\end{cases} \tag{152}$$

With $r_>$ ($r_<$) being the larger (smaller) of r and r', the Green function can be written in a more compact form as

$$G^+_0(\mathbf{r}, \mathbf{r}') = -ik\sum_\Lambda\langle\mathbf{r}_<|j^R_\Lambda\rangle\langle h^L_\Lambda|\mathbf{r}'_>\rangle \tag{153}$$

keeping in mind the two cases in Eq. (152).

Lippmann–Schwinger Equation and Single-Site Green Function. The regular solutions $|J_\Lambda^R\rangle$ fulfill the Lippmann–Schwinger equation $|J^R\rangle = |j^R\rangle + G_0^+ V|J^R\rangle$, or explicitly for the radial part,

$$\langle r|J_\Lambda^R\rangle = \langle r|j_\Lambda^R\rangle - ik\langle r|h_\Lambda^R\rangle \int_0^r dr' r'^2 \langle j_\Lambda^L|r'\rangle V(r')\langle r'|J_\Lambda^R\rangle - ik\langle r|j_\Lambda^R\rangle \int_r^\infty dr' r'^2 \langle h_\Lambda^L|r'\rangle V(r')\langle r'|J_\Lambda^R\rangle \quad (154)$$

The irregular solutions obey $|H^R\rangle = |h^R\rangle + G_0^+ V|H^R\rangle$ and

$$\int_0^\infty dr\, r^2 \langle h^L|r\rangle V(r)\langle r|H^R\rangle = 0 \quad (155)$$

where $|H^R\rangle$ and $|h^R\rangle$ are either of the first (+) or of the second (−) kind [81]. Analogously to the spherical Bessel and Hankel functions, the regular and irregular solutions are related by $|J^R\rangle = (|H^{R(+)}\rangle + |H^{R(-)}\rangle)/2$.

To determine the single-site Green function $G^+(\mathbf{r}, \mathbf{r}')$, one starts from the expression for G^+ in terms of eigenfunctions of the Hamiltonian,

$$G^+(\mathbf{r}, \mathbf{r}') = \int \frac{dk^3}{(2\pi)^3} \frac{\langle \mathbf{r}|\Psi(\mathbf{k}, E)\rangle\langle\Psi(\mathbf{k}, E)|\mathbf{r}'\rangle}{E + i\eta - k^2} \quad (156)$$

and obtains with the regular solutions after integration over angles in reciprocal space

$$G^+(\mathbf{r}, \mathbf{r}') = \frac{2}{\pi} \sum_\Lambda \int_0^\infty dk \frac{\langle \mathbf{r}|J_\Lambda^R(k, E)\rangle\langle J_\Lambda^L(k, E)|\mathbf{r}'\rangle}{E + i\eta - k^2} \quad (157)$$

Because the integrand is even in k, the integration can be extended to the interval $[-\infty, +\infty]$, allowing the integral to be treated as a contour integral. Defining $\alpha = p + i\eta/(2p)$, $p = \sqrt{E}$, and noticing that $\eta = 0^+$, one has $\alpha^2 = E + i\eta$. Thus, the preceding integral contains the factor

$$\frac{k^2}{\alpha^2 + k^2} = -\frac{1}{2}\left(\frac{2k}{k - \alpha} + \underbrace{\frac{k}{k + \alpha} - \frac{k}{k - \alpha}}\right) \quad (158)$$

(k^2 in the numerator on the l.h.s. is due to the path element). The underbraced term is odd in k and thus gives no contribution to the integral. Therefore, one is left with

$$G^+(\mathbf{r}, \mathbf{r}') = \frac{1}{\pi} \sum_\Lambda \int_{-\infty}^\infty dk \frac{\langle \mathbf{r}|J_\Lambda^R(k, E)\rangle k \langle J_\Lambda^L(k, E)|\mathbf{r}'\rangle}{k - \alpha} \quad (159)$$

Replacing $\langle J^L(k, E)|\mathbf{r}'\rangle$ by the sum of $\langle H^{L(+)}(k, E)|\mathbf{r}'\rangle$ and $\langle H^{L(-)}(k, E)|\mathbf{r}'\rangle$, the integral can be performed. Taking the limit $\lim_{\eta\to 0^+}$ eventually yields

$$G^+(\mathbf{r}, \mathbf{r}') = -ik \sum_\Lambda \langle \mathbf{r}_<|J_\Lambda^R(k, E)\rangle\langle H_\Lambda^{L(+)}(k, E)|\mathbf{r}_>\rangle \quad (160)$$

Alternative representations of the single-site Green function follow immediately from operator equations for G. For example, $G = G^0 + G^0 T G^0$ yields [72]

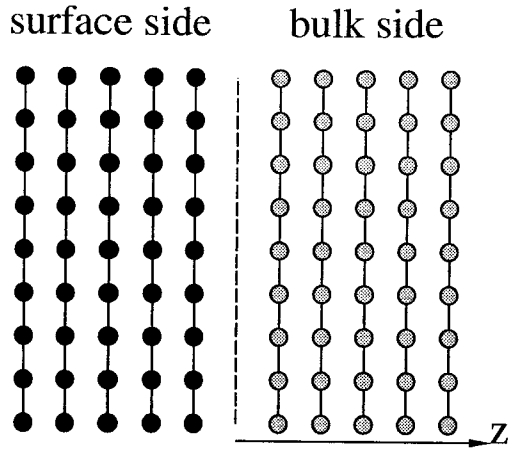

Fig. 31. Arrangement of layers for the calculation of the empty-layer Green function. An empty layer (dashed line) is embedded between stacks of layers (left, surface side, black circles; right, bulk side, gray circles).

$$G^+(\mathbf{r}, \mathbf{r}') = -ik \sum_\Lambda \langle \mathbf{r}_<|j_\Lambda^R(k, E)\rangle\langle h_\Lambda^{L(+)}(k, E)|\mathbf{r}_>\rangle - k^2 \sum_{\Lambda\Lambda'} \langle \mathbf{r}_<|h_\Lambda^R(k, E)\rangle t_{\Lambda\Lambda'} \times \langle h_{\Lambda'}^{L(+)}(k, E)|\mathbf{r}_>\rangle \quad (161)$$

Empty-Layer Green Function. Now consider a solid buildup by layers from which one layer of scatterers is removed (cf. Fig. 31). We will denote this layer with index i as "empty". For semi-infinite solids, one side belongs to the surface region, the other to the bulk region. Note that the following method can treat any kind of embedded layers, the embedding regions may consist of vacuum, films, or semiinfinite solids, respectively. For the Green function of the empty layer, one makes the ansatz

$$G_{\mathrm{EL}}^+(\mathbf{r}_i, \mathbf{r}_i') = G_0^+(\mathbf{r}_i, \mathbf{r}_i') + \sum_{\Lambda\Lambda'} \langle \mathbf{r}_i|j_\Lambda^R\rangle D_{\Lambda\Lambda'}^{ii} \langle j_{\Lambda'}^L|\mathbf{r}_i'\rangle \quad (162)$$

with arguments E and $\mathbf{k}_\parallel$ dropped. The coordinates are taken with respect to layer i, $\mathbf{r}_i = \mathbf{r} - \mathbf{R}_i$. G_0^+ is the retarded Green function of free space, Eq. (152). The coefficients $D_{\Lambda\Lambda'}^{ii}$ have to be determined by the boundary conditions: the Bloch condition parallel to the layers,

$$G_{\mathrm{EL}}^+(\mathbf{r}_i + \mathbf{R}, \mathbf{r}_i') = \exp(i\mathbf{k}_\parallel \cdot \mathbf{R})\, G_{\mathrm{EL}}^+(\mathbf{r}_i, \mathbf{r}_i') \quad (163)$$

($\mathbf{R}$ is a vector of the layer lattice) and correct reflection at both the surface and the bulk side. Thus, $D_{\Lambda\Lambda'}^{ii}$ is decomposed into $D_{\Lambda\Lambda'}^{ii} = A_{\Lambda\Lambda'}^{ii} + B_{\Lambda\Lambda'}^{ii}$. $A_{\Lambda\Lambda'}^{ii}$ is the structure constant of layer i, which obeys

$$A_{\Lambda\Lambda'}^{ii} = -ik \frac{E + c^2}{c^2} \sum_{\mathbf{R}\neq\mathbf{0}} G_{\Lambda\Lambda'}^{ii}(-\mathbf{R}) \exp(i\mathbf{k}_\parallel \cdot \mathbf{R}) \quad (164)$$

Further, one has $h_l^+(k|\mathbf{r} - \mathbf{R}|)\widehat{\langle \mathbf{r} - \mathbf{R}|}\chi_\Lambda\rangle = \sum_{\Lambda'} G_{\Lambda\Lambda'}^{ii}(-\mathbf{R}) \times j_{l'}(kr)\langle \hat{\mathbf{r}}|\chi_{\Lambda'}\rangle$.

To determine the coefficients $B^{ii}_{\Lambda\Lambda'}$, it is convenient to switch from angular-momentum ($\kappa\mu$) to plane wave representation ($\mathbf{g}\tau$), which yields

$$B^{ii}_{\Lambda\Lambda'} = \sum_{s,s'=\pm}\sum_{\mathbf{g}\tau}\sum_{\mathbf{g}'\tau'} a_{\Lambda\tau}(\mathbf{k}^s_{\mathbf{g}}) W^{ss'}_{\mathbf{g}\tau,\mathbf{g}'\tau'} \left(a_{\Lambda'\tau'}(\mathbf{k}^{s'}_{\mathbf{g}'})\right)^* \quad (165)$$

Thus, the matrix B^{ii} is completely determined by the matrices $W^{\pm\pm}$. Considering the reflection at the boundaries of the empty layer, one obtains the following matrix equation:

$$\begin{pmatrix} -R^{+-} & 1 \\ 1 & -R^{-+} \end{pmatrix} \begin{pmatrix} W^{++} & W^{+-} \\ W^{-+} & W^{--} \end{pmatrix} = \frac{1}{iA} \begin{pmatrix} R^{-+} & 0 \\ 0 & R^{+-} \end{pmatrix} \begin{pmatrix} K & 0 \\ 0 & K \end{pmatrix} \quad (166)$$

R^{+-} and R^{-+} are the reflection matrices at the surface side and the bulk side, respectively, which can easily be computed from the scattering matrices of the layers forming the surface and the bulk side stacks. Further, $K_{\mathbf{g}\tau,\mathbf{g}'\tau'} = \delta_{\mathbf{g}\tau,\mathbf{g}'\tau'}/k_{\mathbf{g}\perp}$. Eventually, one obtains

$$W^{++} = R^{+-}W^{-+} \quad (167a)$$

$$W^{+-} = \frac{1}{iF_A}(1 - R^{+-}R^{-+})^{-1}R^{+-}K \quad (167b)$$

$$W^{-+} = \frac{1}{iF_A}R^{-+}(1 - R^{+-}R^{-+})^{-1}K \quad (167c)$$

$$W^{--} = R^{-+}W^{+-} \quad (167d)$$

Note that for a standalone layer, that is, a layer without vacuum embedding on both sides, $R^{+-} = R^{-+} = 0$, which leads to $W^{\pm\pm} = 0$, and the matrix D is given by the structure constant A alone.

It is illustrative to write the empty-layer Green function in terms of outgoing and incoming plane waves. With the definitions

$$\langle v^{\pm}_{\mathbf{g}\tau}|\mathbf{r}'_i\rangle = \frac{1}{iF_A k_{\mathbf{g}\perp}}\langle f^L_{\mathbf{k}^{\pm}_{\mathbf{g}}\tau}|\mathbf{r}'_i\rangle + \sum_{s'=\pm}\sum_{\mathbf{g}'\tau'} W^{\pm s'}_{\mathbf{g}\tau,\mathbf{g}'\tau'}\langle f^L_{\mathbf{k}^{s'}_{\mathbf{g}'}\tau'}|\mathbf{r}'_i\rangle \quad (168a)$$

$$\langle \tilde{v}^{\pm}_{\mathbf{g}\tau}|\mathbf{r}'_i\rangle = \sum_{s'=\pm}\sum_{\mathbf{g}'\tau'} W^{\pm s'}_{\mathbf{g}\tau,\mathbf{g}'\tau'}\langle f^L_{\mathbf{k}^{s'}_{\mathbf{g}'}\tau'}|\mathbf{r}'_i\rangle \quad (168b)$$

one has in matrix form

$$\begin{pmatrix} \mathbf{v}^+ \\ \mathbf{v}^- \end{pmatrix} = \begin{pmatrix} \frac{1}{iF_A}K + W^{++} & W^{+-} \\ W^{-+} & \frac{1}{iF_A}K + W^{--} \end{pmatrix} \begin{pmatrix} \mathbf{f}^{L+} \\ \mathbf{f}^{L-} \end{pmatrix} \quad (169a)$$

$$\begin{pmatrix} \tilde{\mathbf{v}}^+ \\ \tilde{\mathbf{v}}^- \end{pmatrix} = \begin{pmatrix} W^{++} & W^{+-} \\ W^{-+} & W^{--} \end{pmatrix} \begin{pmatrix} \mathbf{f}^{L+} \\ \mathbf{f}^{L-} \end{pmatrix} \quad (169b)$$

and the empty-layer Green function is given by

$$G^+_{\mathrm{EL}}(\mathbf{r}_i, \mathbf{r}'_i) = \sum_{\mathbf{g}\tau}\langle \mathbf{r}_i|f^R_{\mathbf{k}^{\pm}_{\mathbf{g}}\tau}\rangle\langle v^{\pm}_{\mathbf{g}\tau}|\mathbf{r}'_i\rangle + \sum_{\mathbf{g}\tau}\langle \mathbf{r}_i|f^R_{\mathbf{k}^{\mp}_{\mathbf{g}}\tau}\rangle\langle \tilde{v}^{\mp}_{\mathbf{g}\tau}|\mathbf{r}'_i\rangle \quad (170)$$

where the upper (lower) signs are for the case $z > z'$ ($z < z'$). According to this decomposition, the Green function can be interpreted as a propagator: From $\mathbf{r}'_i$ there are outgoing plane waves into the $+z$ direction ($\mathbf{v}^+$ and $\tilde{\mathbf{v}}^+$) and into the $-z$ direction ($\mathbf{v}^-$ and $\tilde{\mathbf{v}}^-$) that are collected at $\mathbf{r}_i$ via $\mathbf{f}^R$. This interpretation is quite helpful in obtaining the interlayer part of the Green function.

Full-Layer Green Function. For the layer-diagonal Green function for the full layer i, we make the ansatz[15]

$$G(\mathbf{r}_i, \mathbf{r}'_i) = G^+(\mathbf{r}_i, \mathbf{r}'_i) + \sum_{\Lambda\Lambda'}\langle \mathbf{r}_i|J^{iR}_{\Lambda}\rangle U^{ii}_{\Lambda\Lambda'}\langle J^{iL}_{\Lambda'}|\mathbf{r}'_i\rangle \quad (171)$$

with the single-site Green function G^+ for a site at layer i, Eq. (160). The regular solutions of the single-site problem fulfill the Lippmann–Schwinger equation for the site potential $V_i(\mathbf{r})$,

$$\langle \mathbf{r}_i|J^{iR}_{\Lambda}\rangle = \langle \mathbf{r}_i|j^R_{\Lambda}\rangle + \int_{\Omega_i} G^+_0(\mathbf{r}_i, \mathbf{r}'_i)V_i(\mathbf{r}'_i)\langle \mathbf{r}'_i|J^{iR}_{\Lambda}\rangle dr'^3_i \quad (172)$$

Thus, the single-site t matrix is given by

$$t^{iR}_{\Lambda\Lambda'} = -ik\int_{\Omega_i}\langle j^L_{\Lambda}|\mathbf{r}_i\rangle V_i(\mathbf{r}_i)\langle \mathbf{r}_i|J^{iR}_{\Lambda'}\rangle dr^3_i \quad (173)$$

Further, $t^{iL}_{\Lambda'\Lambda} = t^{iR}_{\Lambda\Lambda'}$. The single-site solutions show the asymptotics as in Eq. (88). The coefficients $U^{ii}_{\Lambda\Lambda'}$ are determined by the Dyson equation for G,

$$G(\mathbf{r}, \mathbf{r}') = G_{\mathrm{EL}}(\mathbf{r}, \mathbf{r}') + \int_{\Omega} G_{\mathrm{EL}}(\mathbf{r}, \mathbf{r}'')V(\mathbf{r}'')G(\mathbf{r}'', \mathbf{r}')dr''^3 \quad (174)$$

Using the asymptotics for the single-site solutions, one obtains after some manipulation an equation for $U^{ii}_{\Lambda\Lambda'}$, which in matrix form reads

$$U^{ii} = \left(1 - \frac{i}{k}D^{ii}t^{iR}\right)^{-1} D^{ii} \quad (175)$$

where the indices of U^{ii}, D^{ii}, and t^{iR} run over all Λ.

Now we turn to the calculation of the non-layer-diagonal parts of the Green function, that is, the matrices U^{ij} for $i \neq j$. As we have seen, the empty-layer Green function can be interpreted in terms of outgoing and incoming plane waves, Eq. (170). Now the incoming waves do not belong to the empty layer (with index j) but to the full layer (with index i); see Figure 32. The first task is to find the transfer matrix from layer j to layer i. Therefore, the reflection matrix R^{+-}_{surf} at the surface side, the scattering matrix M_{slab} of the layers sandwiched between layers j and i, and the reflection matrix R^{-+}_{bulk} at the bulk side have to be computed according to the methods presented in Section 3. Then the matrix U^{ij} can be computed according to the following scheme:

(i) The wave fields outgoing from layer j in the $\pm z$ direction are given by $\mathbf{v}^{\pm}_j$ in the plane wave representation, Eq. (169). These have to be

[15] Note that the ansatz shows the same structure as in Eq. (162).

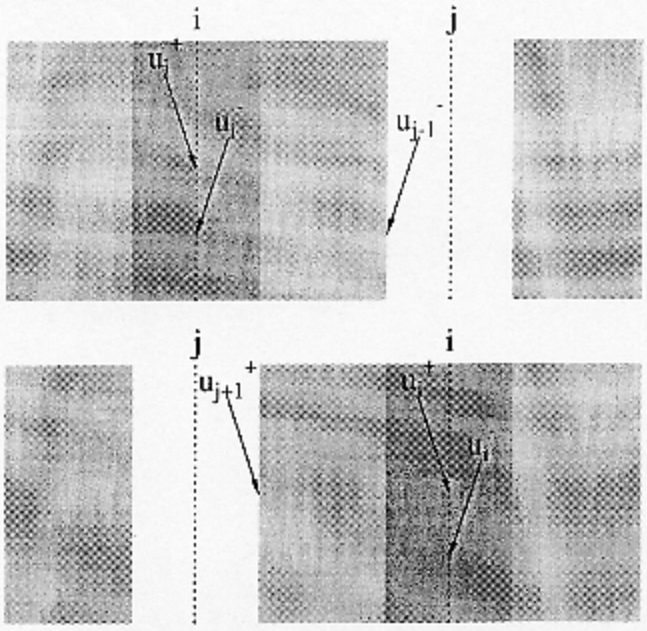

Fig. 32. Arrangement in the calculation of the interlayer part of the empty-layer Green function in the cases $i > j$ (top) and $i < j$ (bottom). The empty layer is labeled j (white), the full layer i (dark gray). Left (right) the surface (bulk) side is displayed. The stack is shown in between layers j and i. Arrows represent outgoing ($\mathbf{u}_{j+1}^+$, $\mathbf{u}_{j-1}^-$) and incoming ($\mathbf{u}_i^\pm$) wave functions.

propagated to the boundaries of the layer stack and give rise to $\mathbf{u}_{j+1}^+ = P^+\mathbf{v}_j^+$ and $\mathbf{u}_{j-1}^- = P^-\mathbf{v}_j^-$.

(ii) The wave field impinging on layer i, which is due to the wave field outgoing from layer j, has to be calculated. For the case $i > j$, that is, the empty layer on the surface side (cf. lower part of Fig. 32), one has

$$\mathbf{u}_i^+ = (1 - M_{\text{slab}}^{+-}R_{\text{bulk}}^{-+})^{-1}M_{\text{slab}}^{++}\mathbf{u}_{j+1}^+ \tag{176a}$$

$$\begin{aligned}\mathbf{u}_i^- &= R_{\text{bulk}}^{-+}(1 - M_{\text{slab}}^{+-}R_{\text{bulk}}^{-+})^{-1}M_{\text{slab}}^{++}\mathbf{u}_{j+1}^+ \\ &= R_{\text{bulk}}^{-+}\mathbf{u}_i^+\end{aligned} \tag{176b}$$

For the case $i < j$, that is, the empty layer on the bulk side (cf. upper part of Fig. 32), analogously

$$\mathbf{u}_i^- = (1 - M_{\text{slab}}^{-+}R_{\text{surf}}^{+-})^{-1}M_{\text{slab}}^{--}\mathbf{u}_{j-1}^- \tag{177a}$$

$$\begin{aligned}\mathbf{u}_i^+ &= R_{\text{surf}}^{+-}(1 - M_{\text{slab}}^{-+}R_{\text{surf}}^{+-})^{-1}M_{\text{slab}}^{--}\mathbf{u}_{j-1}^- \\ &= R_{\text{surf}}^{+-}\mathbf{u}_i^+\end{aligned} \tag{177b}$$

(iii) To express the incoming wave field in terms of regular solutions of layer i, one has to multiply $\mathbf{u}_i^\pm$ by $(1 - iA^{ii}t^i/k)^{-1}$, where A^{ii} and t^i are the structure constant and the single-site t matrix of layer i, respectively.

(iv) To obtain the "full layer" j, one has to solve the Dyson equation. Applying the similar considerations as for the layer-diagonal part, $\mathbf{v}_j^\pm$ has to be multiplied by $-i(1 + it^jU^{jj}/k)$. In summary, the Green function is given by

$$G(\mathbf{r}_i, \mathbf{r}'_j) = G^+(\mathbf{r}_i, \mathbf{r}'_i)\delta_{ij} + \sum_{\Lambda\Lambda'}\langle\mathbf{r}_i|J_\Lambda^{iR}\rangle U_{\Lambda\Lambda'}^{ij}\langle J_{\Lambda'}^{jL}|\mathbf{r}'_j\rangle \tag{178}$$

Table III. Properties of Single-Site Solutions

Function	Behavior for $r \to 0$	Asymptotics for $r \to \infty$
$\|J\rangle$	Regular	$\|j\rangle + \|h\rangle t$
$\|H\rangle$	Irregular	$\|h\rangle$
$\|Z\rangle$	Regular	$\|j\rangle t^{-1} + \|h\rangle$
$\|\bar{J}\rangle$	Irregular	$\|j\rangle$

Scattering-Path Operator and Scattering Solutions. Certain equations of multiple-scattering theory become nicer when they are not formulated in terms of regular and irregular solutions of the single-site problem but in terms of scattering solutions; for example, the matrices U^{mn} are replaced by the scattering-path operators (SPOs) τ^{mn}. The latter are the on-the-energy-shell matrices of the transition operator T. Because the derivation of τ^{mn} can be found in several textbooks (see, e.g., [70–72]), we just recall some basic properties.

The SPO τ^{mn} from site n to site m obeys $\tau^{mn} = t^{mR}\delta_{mn} + t^{mR}\sum_{k\neq m}G^{mk}\tau^{kn}$, where G^{mk} is the structure constant. The matrices U and τ are closely related,

$$U^{mn} = (t^{mR})^{-1}(\tau^{mn} - t^{mR}\delta_{mn})(t^{nL})^{-1} \tag{179}$$

Consider, for example, the Green function that propagates an electron from a site $\mathbf{R}_n$ to a site $\mathbf{R}_m$, $m \neq n$. Taking $\mathbf{r}_n$ and $\mathbf{r}_m$ outside the muffin-tin sphere and using the asymptotic behavior of $|J^{nR}\rangle$ and $\langle J^{mL}|$, cf. Eq. (88), one arrives at

$$G(\mathbf{r}_n, \mathbf{r}_m) = \langle\mathbf{r}_n|j^R(t^{mR})^{-1} + h^R\rangle\tau^{mn}\langle j^L(t^{nL})^{-1} + h^L|\mathbf{r}_m\rangle \tag{180}$$

The preceding equation establishes the regular scattering solutions [169]. Within the muffin-tin sphere, they are given by

$$|Z_\Lambda^R\rangle = \sum_{\Lambda'}|J_{\Lambda'}^R\rangle(t^R)_{\Lambda'\Lambda}^{-1} \tag{181a}$$

$$\langle Z_\Lambda^L| = \sum_{\Lambda'}(t^L)_{\Lambda\Lambda'}^{-1}\langle J_{\Lambda'}^L| \tag{181b}$$

Analogously, the Green function at site $\mathbf{R}_n$ can be written as

$$G(\mathbf{r}_n, \mathbf{r}'_n) = \langle\mathbf{r}_n|Z^{nR}\rangle\tau^{nn}\langle Z^{nL}|\mathbf{r}'_n\rangle - ik\langle\mathbf{r}_n|Z^{nR}\rangle\langle\bar{J}^{nL}|\mathbf{r}'_n\rangle \tag{182}$$

where $|\tilde{J}\rangle$ is an irregular scattering solution. The main properties of the single-site solutions are given in Table III.

Screened-KKR Methods. The Green function G of a system can be obtained from the Dyson equation with respect to the free-space Green function G_0, $G = G_0 + G_0tG$, where t is the single-scattering matrix. The SPO τ is implicitly defined by $G = G_0 + G_0\tau G_0$, which leads to $\tau = (t^{-1} - G_0)^{-1}$ or $G = t^{-1}\tau t^{-1} - t^{-1}$.

The preceding formalism is based on free space as a reference system but can, in fact, rely on any other reference system [170]. The Green function G_r of the reference system is given by $G_r = G_0(1 - t_r G_0)^{-1}$. Now G can be expressed in terms of G_r as $G = G_r(1 - \Delta t\, G_r)^{-1}$ with $\Delta t = t - t_r$. For the SPO, one obtains $\tau_\Delta = [(\Delta t)^{-1} - G_r]^{-1}$. Now, one can ask for a reference system that (i) can easily be computed and (ii) allows for a rapid computation of the Green function G by means of $G = (\Delta t)^{-1}\tau_\Delta(\Delta t)^{-1} - (\Delta t)^{-1}$. One answer is the screened-KKR method, that is, the transformation of the KKR equations into a tight-binding (TB) form.[16] In TB calculations, one exploits that the interaction integrals, which describe the hopping of the electron from one site to another, decay rapidly in configuration space, so that only a few nearest neighbor shells have to be taken into account. This approximation allows for the use of a variety of computational methods to obtain the Green function. Of practical interest is the renormalization scheme or, in the case of disordered systems, the recursion method [171].

Within the screened-KKR method, one uses a reference system that allows a fast computation of τ_Δ. Because Δt is site diagonal, a perfectly suited G_r should also be site diagonal. This, however, cannot be the case in real solid systems. Thus, one tries to construct a reference Green function, that decays as fast as possible in, configuration space. One way is to follow Anderson who invented the screening method and to exploit the scaling properties of the preceding equations in order to construct a "most screened" set of basis functions [172]. Another, more practical way builds the reference system by repulsive ($V_0 > 0$) well-shaped and spherically symmetric potentials of muffin-tin form [173],

$$V(\mathbf{r}) = \begin{cases} V_0 & r < r_{\mathrm{mt}} \\ 0 & \text{otherwise} \end{cases} \tag{183}$$

the t matrix of which can easily be calculated analytically. The screening, that is, the exponential decay of the SPO in real space, can be tuned by the height of the potential wells. Further, in order to compute the reference Green function, one can employ the translational properties of the reference system, in particular, the Bloch property.

Photoemission Final State. The final state in photoemission, the time-reversed LEED state, can be computed either directly via the reflection and transmission matrices of the layers [136] or within the Green function formalism presented here. The LEED state $\Phi_\tau^{\mathrm{LEED}}(\mathbf{r}; E, \mathbf{k})$ at energy E, wave vector $\mathbf{k}$, and spin τ fulfills the Lippmann–Schwinger equation

$$\Phi_\tau^{\mathrm{LEED}}(\mathbf{r}; E, \mathbf{k}) = \langle \mathbf{r} | f_{\mathbf{k}\tau}^R \rangle + \int d^3r' G(\mathbf{r}, \mathbf{r}'; E) V(\mathbf{r}') \langle \mathbf{r}' | f_{\mathbf{k}\tau}^R \rangle \tag{184}$$

that is, the relativistic version of Eq. (137), with the free-space solution $|f_{\mathbf{k}\tau}^R\rangle$ and the potential in the solid V. Instead of using the plane wave representation, we turn again to angular-momentum representation. With Eqs. (147) and (149) for regular solutions ($z = j$), the LEED state at site $\mathbf{R}_n$ is given by

$$\begin{aligned} \Phi_\tau^{\mathrm{LEED}}(\mathbf{r}_n; E, \mathbf{k}) &= \exp(i\mathbf{k}\cdot\mathbf{R}_n) \sum_\Lambda \langle \mathbf{r}_n | j_\Lambda^R \rangle a_{\Lambda\tau}(\hat{\mathbf{k}}) \\ &\quad + \sum_m \exp(i\mathbf{k}\cdot\mathbf{R}_m) \sum_\Lambda \int_{\Omega_m} d^3r'_m G(\mathbf{r}_n, \mathbf{r}'_m; E) \\ &\quad \times V(\mathbf{r}'_m) \langle \mathbf{r}'_m | j_\Lambda^R \rangle a_{\Lambda\tau}(\hat{\mathbf{k}}) \end{aligned} \tag{185}$$

with G from Eq. (171). Inserting the interlayer contribution to the Green function, one arrives at a term

$$\begin{aligned} &\sum_m \exp(i\mathbf{k}\cdot\mathbf{R}_m) \sum_{\Lambda\Lambda'\Lambda''} \langle \mathbf{r}_n | J_{\Lambda'}^R \rangle U_{\Lambda'\Lambda''}^{nm} \\ &\quad \times \underbrace{\int_{\Omega_m} d^3r'_m \langle J_{\Lambda''}^L | \mathbf{r}'_m \rangle V(\mathbf{r}'_m) \langle \mathbf{r}'_m | j_\Lambda^R \rangle}_{= t_{\Lambda''\Lambda}^L/(-ik)} a_{\Lambda\tau}(\hat{\mathbf{k}}) \\ &= \frac{i}{k} \sum_m \exp(i\mathbf{k}\cdot\mathbf{R}_m) \sum_{\Lambda\Lambda'\Lambda''} \langle \mathbf{r}_n | J_{\Lambda'}^R \rangle U_{\Lambda'\Lambda''}^{nm} t_{\Lambda''\Lambda}^L a_{\Lambda\tau}(\hat{\mathbf{k}}) \end{aligned} \tag{186}$$

For the evaluation of the remaining single-site terms, one exploits the Lippmann–Schwinger equation (172) for the regular solutions. Thus, these terms reduce to $|J_\Lambda^{nR}\rangle$. In summary, the LEED state at site $\mathbf{R}_n$ is given by

$$\begin{aligned} \Phi_\tau^{\mathrm{LEED}}(\mathbf{r}_n; E, \mathbf{k}) &= \exp(i\mathbf{k}\cdot\mathbf{R}_n) \sum_\Lambda \langle \mathbf{r}_n | J_\Lambda^R \rangle a_{\Lambda\tau}(\hat{\mathbf{k}}) + \frac{i}{k} \sum_m \exp(i\mathbf{k}\cdot\mathbf{R}_m) \\ &\quad \times \sum_{\Lambda\Lambda'\Lambda''} \langle \mathbf{r}_n | J_{\Lambda'}^R \rangle U_{\Lambda'\Lambda''}^{nm} t_{\Lambda''\Lambda}^L a_{\Lambda\tau}(\hat{\mathbf{k}}) \end{aligned} \tag{187}$$

A slightly more compact form is obtained using the SPO,

$$\Phi_\tau^{\mathrm{LEED}}(\mathbf{r}_n; E, \mathbf{k}) = \frac{i}{k} \sum_m \exp(i\mathbf{k}\cdot\mathbf{R}_m) \sum_{\Lambda\Lambda'} \langle \mathbf{r}_n | Z_\Lambda^R \rangle \tau_{\Lambda\Lambda'}^{nm} a_{\Lambda\tau}(\hat{\mathbf{k}}) \tag{188}$$

It is worth mentioning that a construction of the final state in terms of Bloch states has been given by Bross [174] (see also [69]).

Transition-Matrix Elements and Photocurrent. A photoemission theory is incomplete as long as the transition-matrix elements are not taken into account. The interaction of an electron with incoming monochromatic light of frequency ω and with wave vector $\mathbf{q}$ is relativistically described by the Hamiltonian

$$H'(\mathbf{r}, t) = \alpha \cdot \mathbf{A}(\mathbf{r}, t) = \alpha \cdot \mathbf{A}_0 \exp(i\mathbf{q}\cdot\mathbf{r} - \omega t) \tag{189}$$

Upper and lower components of the Dirac spinors are coupled via α, Eq. (79). Usually, one decomposes $\mathbf{A} = (A_x, A_y, A_z)$ into (A_+, A_-, A_z) with $A_\pm = A_x \pm iA_y$, that is, into contribution from left- and right-handed circularly polarized light as well as linearly polarized light.

[16] Therefore, screened methods are sometimes loosely denoted as TB methods (TB-KKR, TB-LMTO, where LMTO is short for linearized muffin-tin orbital).

The transition-matrix elements between the Dirac spinors at a particular site are integrals over the muffin-tin sphere. Integration over angles, that is, matrix elements of $\alpha \cdot \mathbf{A}$ of the central-field spinors $|\chi_\Lambda\rangle$, yield the well-known "atomic" selection rules [175]: The angular momentum l has to differ by 1, $\Delta l = \pm 1$, and its z projection m is conserved for linearly polarized light, $\Delta m = 0$, or for circularly polarized light it is changed by 1, $\Delta m = \pm 1$. The integration over the radial part has to be computed numerically. The Green function of the initial state consists of both regular and irregular solutions, the time-reversed LEED state of regular solutions only. Therefore, one has to consider two general types of matrix elements. For those between regular solutions, one has

$$M^{(1)}_{i\Lambda'\Lambda} = \int_0^{R_{\mathrm{mt}}} \langle J_{\Lambda'}|r\rangle \alpha_i A_i \langle r|J_\Lambda\rangle dr \qquad i = \pm, z \qquad (190)$$

The single-site term of the Green function gives rise to a double integral, $M^{(2)}_{i\Lambda'\Lambda}$, due to the selection of regular and irregular wave functions with respect to r; see Eq. (160). In the preceding definition, we have suppressed the indices L and R, which are due to the occurrence of left and right wave functions.

Eventually, the spin-density matrix ρ of the photoelectron is given by [cf. Eq. (138)]

$$\rho_{\tau\tau'} \sim \langle \Phi_{0\tau}|G^{\mathrm{a}}(E+\omega)\Delta \operatorname{Im} G^{+}(E)\Delta^{\dagger}G^{r}(E+\omega)|\Phi_{0\tau'}\rangle \qquad \tau, \tau' = \pm \qquad (191)$$

which, besides the computation of the photocurrent $I = \mathrm{tr}(\rho)$, allows for computation of the spin polarization of the photoelectrons $\mathbf{P} = \mathrm{tr}(\sigma\rho)/\mathrm{tr}(\rho)$. Note that due to SOC the spin polarization can be nonzero even from nonmagnetic solids (see, e.g., [150]).

Because the final state is a time-reversed LEED state, it shows the same symmetry properties as a LEED state; cf. Section 3.2.2. This, together with knowledge of the light polarization, allows for a detailed group-theoretical analysis of photoemission from (ferromagnetic) surfaces [58, 176]. In particular, it reveals the initial states for which dipole transitions are allowed or forbidden (see also [97]).

A popular approximation for analyzing experimental spectra is the direct-transition model. If the initial states are taken as Bloch states, for example, by neglecting the surface of the sample, the normal component $k_\perp$ of the wave vector is conserved in the transition process. This allows for a mapping of the intensity maxima to the band structure $k_\perp(E, \mathbf{k}_\parallel)$.

Before turning to applications of the multiple-scattering theory of photoemission, basic properties of photoemission from ultra-thin films should be addressed.

4.2.4. *Simple Theory of Photoemission from Ultra-Thin Films*

In recent experimental work on photoemission from films with thicknesses of a few layers, the photoemission intensity maxima show dispersion, as in the bulk case, and can be well described within the direct-transition model using bulk-band structures.

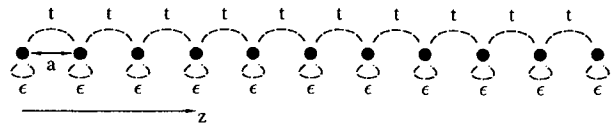

Fig. 33. Linear chain along the z axis with $n = 11$ equidistant sites with intersite distance a. The tight-binding parameters, cf. Eq. (192), are the on-site energy ϵ and the next nearest neighbor hopping energy t, visualized by dashed lines.

This led to the conclusion that even ultra-thin films "show a (bulk) band structure" [177, 178]. This behavior can be understood within a simple theory of photoemission from linear chains [179], which will be presented in the following (for an approach based on Green functions, see [180]).

There are two limits in which valence electrons in a film can be described (see Section 2 and, e.g., [21, 181–184]): (i) In a plane wave representation, free electrons can be confined to a quantum well. (ii) In a tight-binding description, electrons are allowed to hop only within a finite number of layers. The prototypical realization of the latter model is rare-gas layers on a (metal) substrate (cf. Section 2.2.3).

The film is represented by a linear chain oriented along the z axis, that is, perpendicular to the surface, with n equidistant sites i, $i = 1, \ldots, n$, with one orbital $|\Phi_i\rangle$ per site. The latter is located at $ia\mathbf{e}_z$, a denoting the intersite distance (Fig. 33) [185–188]. Further, the overlap between the normalized orbitals located on different sites is assumed to be 0, $\langle \Phi_i|\Phi_j\rangle = \delta_{ij}$. Neglecting the substrate completely, the elements of the Hamiltonian matrix $H^{(n)}$ read

$$H^{(n)}_{ij} = \epsilon\delta_{ij} + t\delta_{|i-j|,1} \qquad i, j = 1, \ldots, n \qquad (192)$$

with on-site energies $\epsilon = \langle \Phi_i|H^{(n)}|\Phi_i\rangle$ and next nearest neighbor hopping energies $t = \langle \Phi_i \mid H^{(n)} \mid \Phi_{i+1}\rangle$. The eigenvalues of $H^{(n)}$ can be written as

$$\lambda^{(n)}_i = \epsilon + 2t\cos\left(k^{(n)}_i a\right) \qquad i = 1, \ldots, n \qquad (193)$$

with $k^{(n)}_i = \pi i/[a(n+1)]$. In the case of a single site where there is obviously no hopping, $\lambda^{(1)}_1 = \epsilon$. For an infinite chain (i.e., in the limit $n \to \infty$), $k^{(n)}_i a$ is dense in $[0, \pi]$ and, thus, the eigenvalues represent the bulk-band structure $E(k) = \epsilon + 2t\cos(ka)$; cf. Figure 34. An eigenfunction $|\Psi^{(n)}_i\rangle$ of $H^{(n)}$ with energy $\lambda^{(n)}_i$ can be written as

$$\left|\Psi^{(n)}_i\right\rangle = \sum_{j=1}^{n} c^{(n)}_{ij}|\Phi_j\rangle \qquad i = 1, \ldots, n \qquad (194)$$

the coefficients $c^{(n)}_{ij}$ of which can be calculated iteratively by

$$c^{(n)}_{ij} = 2\cos\left(k^{(n)}_i a\right)c^{(n)}_{i,j-1} - c^{(n)}_{i,j-2} \qquad j = 2, \ldots, n \qquad (195)$$

with $c^{(n)}_{i0} = 0$ and $c^{(n)}_{i1} = 1$. The additional relation $2\cos(k^{(n)}_i a)c^{(n)}_{i,n} = c^{(n)}_{i,n-1}$ ensures that $k^{(n)}_i$ has to be chosen properly. It can easily be shown that $c^{(n)}_{ij} \sim \sin(\pi_{ij}/a(n+1))$. Strictly speaking, $k^{(n)}_i$ is not a wave number as it is in the case

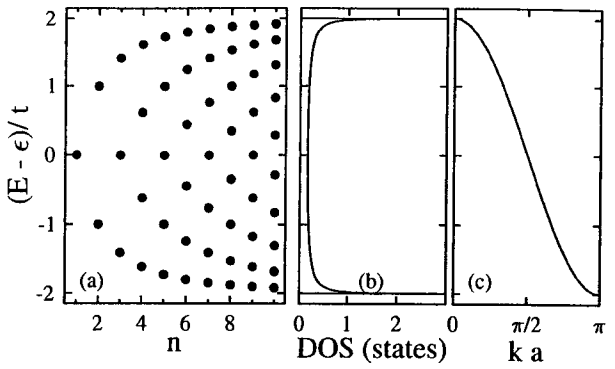

Fig. 34. Tight-binding electronic structures of linear chains. The tight-binding parameters are ϵ and t; cf. Eq. (192). (a) Eigenenergies $\lambda_i^{(n)}$ [dots; cf. Eq. (193)] of chains with $n = 1, \ldots, 10$ sites. (b) Density of states (DOS) of the infinite chain. (c) Band structure $E(k) = \epsilon + 2t\cos(ka)$ of the infinite chain. Reprinted with permission from J. Henk and B. Johansson, *J. Electron Spectrosc. Relat. Phenom.* 105, 187 (1999). Copyright 1999, by Elsevier Science.

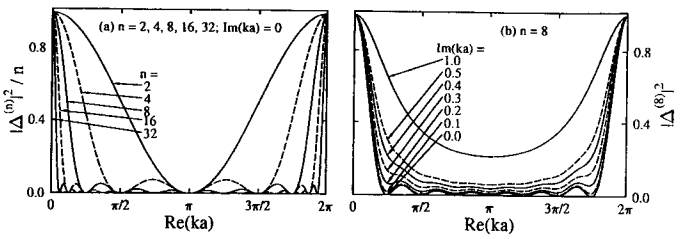

Fig. 35. The "k-conservation" function $|\Delta^{(n)}|^2$, as defined in Eq. (198). (a) Dependence on the number of sites n in the linear chain. n ranges from 2 to 32, as indicated, $\mathrm{Im}(ka) = 0$. (b) Dependence on $\mathrm{Im}(ka)$. $\mathrm{Im}(ka)$ ranges from 0.0 to 1.0, $n = 8$.

of Bloch states because there is no translational symmetry and therefore no periodicity. Due to the inversion symmetry, the eigenstates $\Psi_i^{(n)}$ show the expected even–odd alternation [cf. Eq. (19)], and the number of nodes in the wave function increases with $|k_i^{(n)}|$.

The photoelectron state $|\Psi_f\rangle$ can crudely be approximated by a single plane wave, $\langle \mathbf{r}|\Psi_f\rangle = \exp(i\mathbf{k}_f \cdot \mathbf{r})$, as is often done in the interpretation of experimental data. This way, quantum-size effects in the upper band structure that show up, for example, in LEED (cf. Section 3.3) are ignored. The wave vector $\mathbf{k}_f$ is determined by both the position of the detector and the energy of the photoelectron, $E_f \sim k_f^2$. The photocurrent $I_i^{(n)}$ at photon energy ω from the initial state $|\Psi_i^{(n)}\rangle$ is given by Fermi's golden rule, Eq. (141). Inserting the previous expressions for the wave functions and defining the Fourier-transformed atomic wave function $F(\mathbf{k})$ by $F(\mathbf{k}) = \int \Phi^*(\mathbf{r}) \exp(i\mathbf{k}\cdot\mathbf{r})\, d^3r$, one obtains eventually

$$I_i^{(n)} \propto |\mathbf{E}\cdot\mathbf{k}_f|^2 |F(\mathbf{k}_f)|^2 \left|\Delta_i^{(n)}(k_{f\perp})\right|^2 \delta\left(E_f - \omega - \lambda_i^{(n)}\right) \quad (196)$$

The function $\Delta_i^{(n)}(k)$, which is defined by

$$\Delta_i^{(n)}(k) = \sum_{j=1}^{n} c_{ij}^{(n)} \exp(ikja) \quad (197)$$

determines considerably the dependence of the photocurrent on the photon energy and, thus, should be discussed in more detail. Obviously, $\Delta_i^{(n)}$ is periodic with period $2\pi/a$. In the case of a single site, $n = 1$, $|\Delta^{(1)}(k)| = 1$ and the photon energy dependence of the photocurrent is determined solely by $F(\mathbf{k}_f)$. In the case of an infinite chain, $n \to \infty$, strict wave vector conservation, $\Delta^{(\infty)}(k_{f\perp}) = \delta(k_{f\perp} - k)$, is obtained; that is, the direct-transition model is recovered.

Setting all $c_{ij}^{(n)} = 1$ leads to a geometrical series for $\Delta^{(n)}$,

$$\Delta^{(n)}(k) = \begin{cases} n & \text{for } k = 0 \\ (q^n - 1)/(q - 1) & \text{otherwise} \end{cases} \qquad q = \exp(ika) \quad (198)$$

Obviously, $\Delta^{(n)}$ shows $n - 1$ zeros in $[0, 2\pi]$ at $ka = 2\pi i/n$ with $i = 1, \ldots, n - 1$. Its absolute value increases with n in the vicinity of $k = 0$, whereas it decreases in the interior of the interval $[0, 2\pi]$. In short, $\Delta^{(n)}$ is an approximation of Dirac's δ function [189] (cf. Fig. 35). The main photoemission intensity comes from the region around $k = 0$ (i.e., $k_{f\perp} = k_i^{(n)}$), but additional intensity maxima, which are due to the oscillatory behavior of $\Delta^{(n)}$, should occur.

So far, we have considered only the case of infinite lifetime of the photoelectron. Introducing a finite lifetime leads to a complex wave number [53], which results in an additional weakening of the k conservation, as is also shown in Figure 35. $\Delta^{(n)}$ decreases rapidly around $k = 0$ with increasing $\mathrm{Im}(ka)$ (as is evident from the geometrical series), but the oscillatory behavior is still visible, except for very strong damping, for example, $\mathrm{Im}(ka) = 0.5$ in Figure 35b.

Photoemission from chains with length of 5 and 10 sites is compared in Figure 36. The intensities were obtained from Eq. (196) with $|\mathbf{E}\cdot\mathbf{k}_f|^2 |F(\mathbf{k}_f)|^2$ set to 1, but $\Delta_i^{(n)}$ calculated with the coefficients $c_{ij}^{(n)}$ obtained from Eq. (195). At the bottom of each box, the initial-state band structure $E(k_{f\perp})$ is shown (note that $k_{f\perp}$ is related to the photon energy ω by $\mathbf{k}_f^2 \sim \lambda_i^{(n)} + \omega$). The individual photoemission intensities show main maxima at $k_i^{(n)}$, that is, $E(k_{f\perp}) = \lambda_i^{(n)}$. In other words, one obtains approximate $k_\perp$ conservation. However, the intensities show oscillatory behavior (cf. Fig. 35). Further, the main maxima for $n = 5$ (Fig. 36b) are much broader than those for $n = 10$ (Fig. 36a) due to the weakening of the k conservation for shorter chains.

The finite photoelectron lifetime can be modeled using complex energies [53], which leads to complex $k_{f\perp}$. Its effect is addressed for a 10-site chain in Figure 37. For a rather large lifetime [$\mathrm{Im}(k_{f\perp}a) = 0.2$, in Fig. 37b], there are still oscillations with $k_{f\perp}$ in the photoemission intensities from the individual initial states. These become smeared out for decreasing lifetime [e.g., $\mathrm{Im}(k_{f\perp}a) = 0.5$ in Fig. 37a]. However, the intensities follow the bulk-band structure in both cases. At a fixed photon energy or a fixed $\mathrm{Re}(k_{f\perp})$, for example, $\mathrm{Re}(k_{f\perp}) = 0$, the EDC becomes broader with increasing $\mathrm{Im}(k_{f\perp})$, which is due to the smearing out of the individual maxima and not to the uncertainty in $k_{f\perp}$.

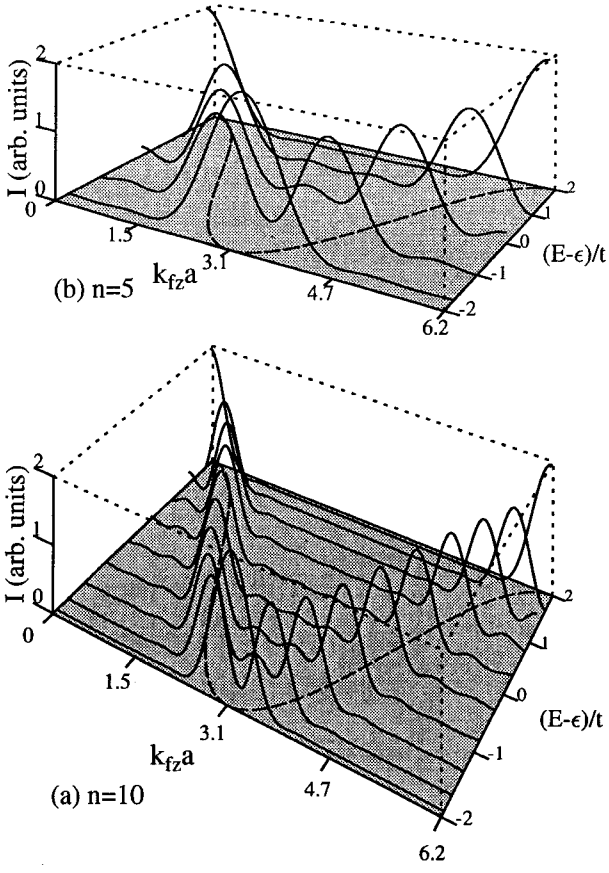

Fig. 36. Photoemission from linear chains with lengths 10 (a) and 5 sites (b), respectively. The intensity I is shown for each initial state at energy $\lambda_i^{(n)}$ [cf. Eq. (193)] for final-state wave numbers $k_{f\perp}$ ranging from 0 to $2\pi/a$ and $\mathrm{Im}(k_{f\perp}a) = 0$. The initial-state band structure $E(k) = \epsilon + 2t\cos(ka)$ (dashed) is shown at the bottom of each box. Intensities are scaled to the same maximum in each box. Reprinted with permission from J. Henk and B. Johansson, *J. Electron Spectrosc. Relat. Phenom.* 105, 187 (1999). Copyright 1999, by Elsevier Science.

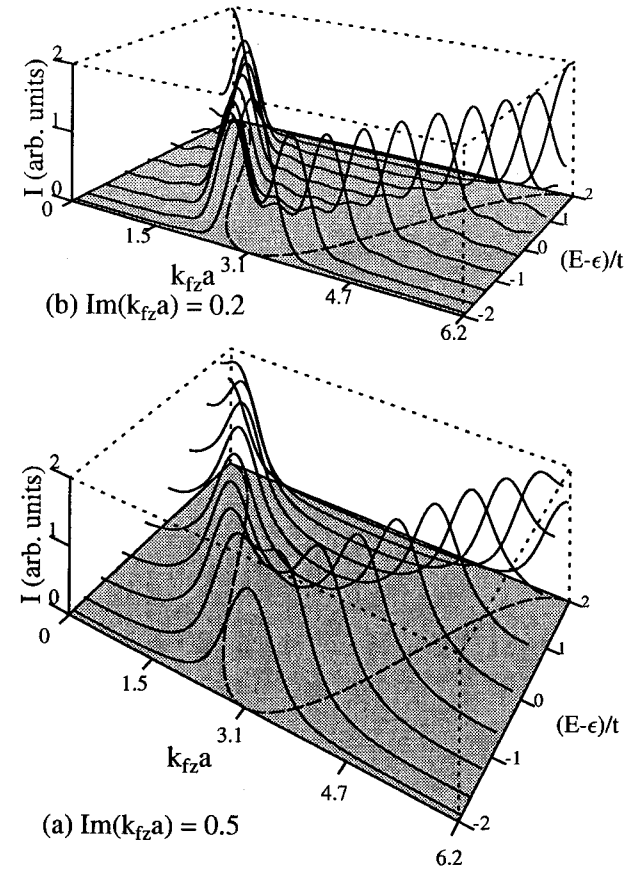

Fig. 37. Same as Figure 36, but for photoemission from chains with 10 sites for $\mathrm{Im}(k_{f\perp}a) = 0.5$ (a) and $\mathrm{Im}(k_{f\perp}a) = 0.2$ (b), respectively. Reprinted with permission from J. Henk and B. Johansson, *J. Electron. Spectrosc. Relat. Phenom.* 105, 187 (1999). Copyright 1999, by Elsevier Science.

In summary, photoemission from ultra-short chains shows the following properties: (i) The confinement of the valence electrons to the chain leads to a weakening of the wave number conservation: the shorter the chain, the broader the photoemission maxima in $k_{f\perp}$. (ii) Besides the periodicity with $2\pi/a$, individual photoemission intensities show oscillations with $k_{f\perp}$, the number of which is proportional to the chain length. These oscillations become smaller in intensity with decreasing photoelectron lifetime [increasing $\mathrm{Im}(k_{f\perp})$]. (iii) Even for very small lengths, the main maxima in the photoemission intensity follow the initial-state bulk-band structure, despite the fact that the initial-state energies are discrete (quantum-well states).

4.3. Applications

In the following, we focus on theoretical photoemission results for metallic films on metal substrates, which were obtained by multiple-scattering methods. Further, representative experimental data that show fingerprints of QWSs are presented.

4.3.1. Ultra-Thin Cu Films on fcc Co(100)

Hansen et al. performed photoemission experiments for ultrathin Cu films on fcc Co with an identical number of Cu layers but different crystallographic orientation of the substrate [190]. For 14 layers of Cu on fcc Co(111), they found a bulklike dispersion in the Cu *sp* states but three quantized states with fixed energy for fcc Co(100) and fcc Co(110) substrates (see Fig. 38). These findings were explained by the bulk-band structure of Co: Only in the latter two cases do bandgaps lead to confinement of the valence electrons to the Cu films and thus to QWSs. Further, it was observed that for the (100) and (110) films the photoemission intensities from the QWSs behave similarly to those of semi-infinite Cu(100) or Cu(110), respectively, which can also be understood by means of photoemission from linear chains (Section 4.2.4). A closer look at the intensity variations, however, gives hints that the maxima show more structure in their dependence on both the binding energy and the photon energy.

Ultra-thin Cu films on fcc Co(001) lend themselves support as prototypical systems because of extensive experimental and theoretical work. However, experimental [183, 191–194] and theoretical [195] investigations dealing with Cu/Co have focused mainly on the properties of QWSs as a function of the film thickness (e.g., binding energy and spin polarization). Usu-

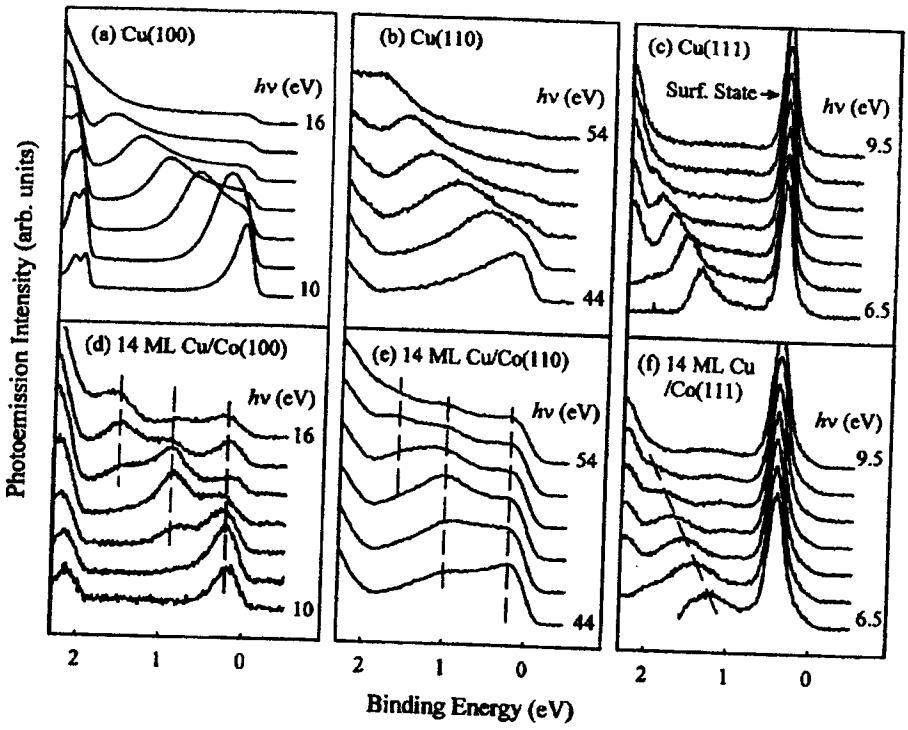

Fig. 38. Experimental normal-emission photoelectron spectra for single-crystal Cu surfaces and for Cu films 14 layers in thickness on Co substrates for (100) (left), (110) (middle), and (111) (right) orientation. Photon energies are evenly spaced between the lower and upper bounds indicated in each graph. The vertical dashed lines for Cu/Co(100) and Cu/Co(110) indicate the position of intensity maxima related to quantum-well states, while the dashed line for Cu/Co(111) indicates the dispersion of a peak related to emission from a Cu bulk band. Reprinted with permission from E. D. Hansen, T. Miller, and T.-C. Chiang, *J. Phys.: Condens. Matter* 9, L435 (1997). Copyright 1997, by the Institute of Physics.

ally, such analyses were performed at a fixed photon energy. In the following, we focus on a few film thicknesses but extend the analysis to variable photon energy in order to work out the manifestation of quantum-size effects in photoemission. Photoemission from Cu/Co(001) is analyzed by means of calculations within the one-step model of photoemission based on multiple-scattering theory (SPRLKKR), as presented in Section 4.2.3.

Quantum-Well States in Cu Films on fcc Co(001). Typical photoemission spectra from Cu/Co(001) for various thicknesses of the Cu films are shown in Figure 39. The intensity maxima are labeled by numbers that refer to the QWSs in the film (cf. Fig. 7). With increasing thickness, the maxima disperse to higher energies. At a fixed binding energy, for example, at the Fermi level E_F, the intensity is higher if a QWS crosses this energy than if there is no QWS at that particular energy. This gives rise to oscillations in the photoemission intensity at a fixed binding energy, as shown in the top panel of Figure 39 (and discussed later).

Before turning to the photoemission results, the electronic structure of Cu films on fcc Co(001) at $\bar{\Gamma}$, which is relevant for normal emission, $\mathbf{k}_\parallel = 0$, is briefly analyzed. The perpendicular component $k_\perp$ of the wave vector takes values from the direction Γ–Δ–X in the bulk Brillouin zone. The Cu *sp* band belongs to the double-group representation Δ_6; the related wave functions show a prominent Δ^1 single-group (spatial) contribution (for applications of group theory in solid-state physics, see [59, 196]). To confine these electrons completely within the Cu film, the Co substrate has to have a gap in the Δ^1 bands. This is the case for minority electrons below -0.65 eV (light-gray area in Fig. 40), for majority electrons below -2.09 eV (dark-gray area in Fig. 40).

To distinguish among surface states, interface states, and QWSs, one calculates the layer-resolved Bloch spectral function (LDOS) for the whole Cu film and the subsequent Co layers. Surface and interface states, the energies of which may also lie in a bandgap of Co, are localized at the respective boundary (e.g., vacuum/Cu or Cu/Co). This means that the corresponding maxima in the LDOS decrease with distance from the boundary. Quantum-well states, however, show maxima in the whole Cu film but decreasing maxima in the Co substrate. The latter can be attributed to the gap in the bulk-band structure of Co because the QWSs cannot couple to Bloch states but to evanescent states in the Co substrate. Further, the energetic position of surface and interface states is expected not to depend significantly on the number of Cu layers, whereas QWSs should show the typical dispersion with film thickness (see Section 2 and Fig. 39).

The Bloch spectral function for a 14-ML Cu film shows two sharp maxima of minority spin character with energies -1.52 and -0.80 eV, respectively, which are denoted as QWSs *A*

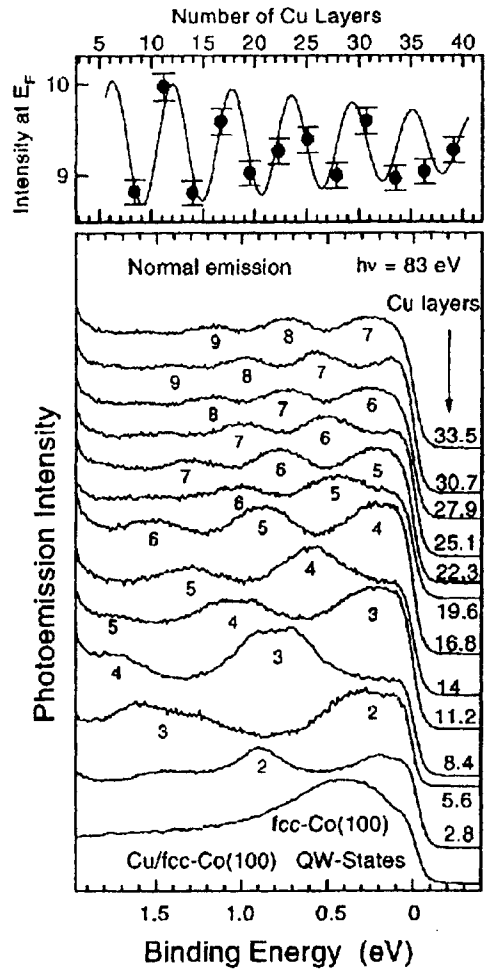

Fig. 39. Experimental photoemission from Cu films on fcc Co(100) for $\mathbf{k}_\parallel = 0$ and 83 eV photon energy. The lower panel shows intensity versus Cu film thickness (as indicated on the right of each spectrum). Intensity maxima related to quantum-well states are labeled by numbers (cf. also Fig. 7). The upper panel depicts intensity modulation at the Fermi level (0 eV) versus film thickness. Reprinted with permission from P. Segovia, E. G. Michel, and J. E. Ortega, *Phys. Rev. Lett.* 77, 3455 (1996). Copyright 1996, by the American Physical Society.

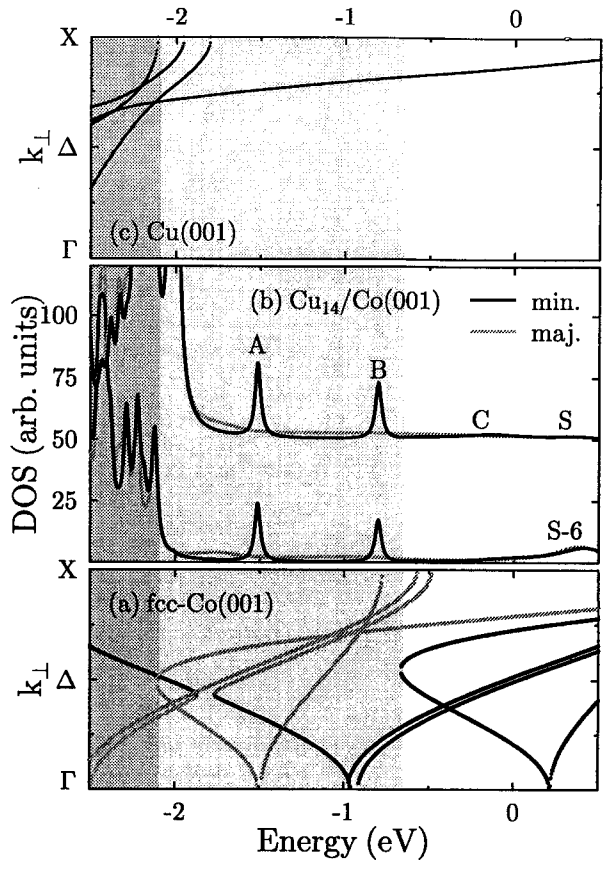

Fig. 40. Spin-resolved relativistic electronic structure of 14-ML Cu on fcc Co(001) for $\overline{\Gamma}$ ($\mathbf{k}_\parallel = 0$, Γ–Δ–X in the bulk Brillouin zone). (a) Band structure of fcc Co(001) along Γ–Δ–X. The sliding gray scale of the bands indicates dominant majority (minority) spin orientation with black (light gray). (b) Density of states of 14-ML Cu on fcc Co(001) for the outermost (S) and a central ($S-6$) layer with black (light gray) lines indicating minority (majority) spin orientation. (c) Same as (a), but for Cu(001). Gray areas indicate gaps in the Co band structure: dark gray for both majority and minority electrons, light gray for minority electrons with prominent Δ^1 spatial symmetry. The latter leads to confinement of minority electrons in the Cu film; see maxima A and B in panel (b). For C, see text. The Fermi energy is at 0 eV. Reprinted with permission from J. Henk and B. Johansson, *J. Electron Spectrosc. Relat. Phenom.* 105, 187 (1999). Copyright 1999, by Elsevier Science.

and B in Figure 40b. The latter agree reasonably well with those obtained experimentally by Hansen and coworkers [190], who found QWSs at -1.5 and -0.9 eV (see also Fig. 39 and [191, 192]). At energies larger than -0.65 eV, the Bloch spectral function shows weak maxima, which may also be associated with QWSs but lack the complete confinement due to the weak reflection at the Cu/Co interface at these energies [197]. There is no even–odd alternation of the QWSs, as found in the simple tight-binding model (Section 4.2.4), due to the lack of inversion symmetry in the Cu film.

The reflectivity at the Cu/Co boundary, as obtained theoretically by Dederichs and co-workers [197], is shown in Figure 41. In the lowest panel, the reflectivity of the Bloch state, which is associated with the Cu *sp* valence band, is shown for incidence on a Co film with 20 ML thickness. At energies less than -0.6 eV, there is almost complete reflection in the minority spin channel, in accordance with the band structure shown in Figure 40. Above -0.6 eV, there are QWSs in the Co film, which reduce the reflectivity; cf. the pronounced minima in the reflectivity. This picture corresponds nicely to that of the quantum-well resonances in LEED (see Section 3.3): Here, the incoming wave is the Cu Bloch state, whereas in LEED it is the electron beam.

Manifestation of Quantum-Size Effects in Photoemission. As a prototypical example, normal photoemission ($\mathbf{k}_\parallel = 0$) with p-polarized light that impinges with a polar angle of 45° onto the surface is discussed in detail. In Figure 42, photoemission from semi-infinite Cu(001) is compared to that of 14-ML Cu on fcc Co(001). For the former (Fig. 42a), the intensity at energies below -2 eV stems from the d-band regime. The maximum that disperses from the Fermi energy at 10 eV photon energy down to -2 eV at 17 eV photon energy is due to emission

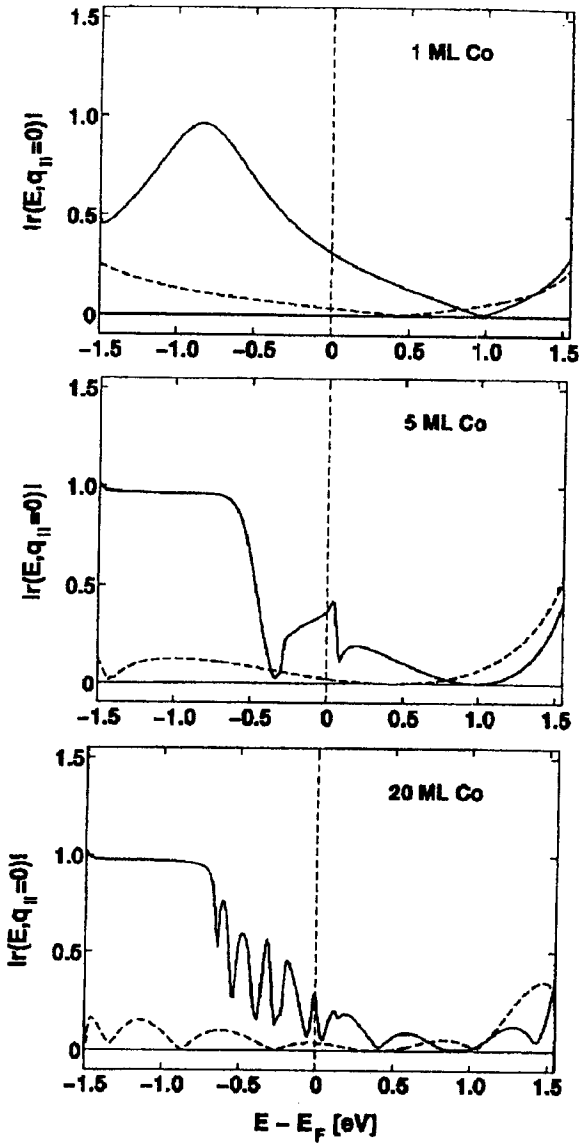

Fig. 41. Reflectivity r of a Cu Bloch wave of Δ_1 representation (along the Γ–Δ–X direction, $\mathbf{k}_{\parallel} = 0$) at the Cu/Co interface versus Co film thickness [from top to bottom, 1-ML, 5-ML, and 20-ML Co on Cu(001)]. Note that distinct minima occur which can directly be attributed to quantum-well states in the Co film (cf. [198]). Solid lines, minority spin; dashed lines, majority spin. Reprinted with permission from P. H. Dederichs, K. Wildberger, and R. Zeller, *Physica B* 237–238, 239 (1997). Copyright 1997, by Elsevier Science.

from the Cu *sp* band (cf. Fig. 40c). The direct-transition model can be used to explain the widths of these maxima: The *sp* band and the final-state band are almost parallel in the band structure and, thus, there is a certain energy range where the difference in the respective $k_\perp$ is rather small [166]. The slightly weakened $k_\perp$ conservation results therefore in a broad maximum. For the 14-ML Cu film on fcc Co(001) (Fig. 42b), the energies of the QWSs lead to narrow maxima [199]. The two sharp peaks, *A* and *B*, correspond to those found in the LDOS (Fig. 40b). The intensity distribution of structure *C*, however, agrees with that found for Cu(001), which can be also explained by the LDOS: Near E_F there are no strictly confined electronic states in the Cu film because the reflection at the Cu/Co interface is small. This qualitative difference between *A* and *B* on the one hand and *C* on the other is further established in the photoelectron spin polarization. *A* and *B* show strong minority polarization ($P \approx -0.75$), whereas *C* is weakly spin polarized ($P \approx -0.05$), as expected from the LDOS.

The intensity variation with photon energy of maxima *A* and *B* is similar to that found for semi-infinite Cu(001) at the respective binding energies, a finding that confirms nicely both the simple theory presented in Section 4.2.4 and the experiment. At this point, quantum-size effects seem to occur only in the widths of those intensity maxima that are associated with QWSs [199]. This feature should be observable with high-resolution photoemission techniques [200]. However, hints about this behavior may be seen, for example, in the work by Hansen et al. (Fig. 38).

Further pronounced manifestations of quantum-size effects in photoemission are intensity oscillations with photon energy. These can be observed in the CIS mode of photoemission (Fig. 29): The initial-state energy is chosen as that of a QWS and the photon energy is varied while keeping $\mathbf{k}_{\parallel}$ fixed. The results for semi-infinite Cu(001) and 14 ML on fcc Co(001) are shown in Figure 43 where the initial-state energies were chosen as those of QWSs *A*, *B*, and *C*.

For semi-infinite Cu(001), one observes for each initial-state energy a dominating maximum and a few smaller maxima and shoulders (Fig. 43a). The former directly reflects the $k_\perp$ conservation; the latter can be explained by the final-state band structure. Further, because the wave function of the initial state does not change rapidly with energy, as is evident from the band structure, the three CIS spectra show almost the same shape, which appears only shifted in photon energy (see the inset in Fig. 43a). In other words, the CIS spectral shapes are governed by the final states. The fine structure for the energy of state *C* is slightly more pronounced when compared to those for *A* and *B* because of the larger photoelectron lifetime, which decreases with kinetic energy. The most important observation, however, is the absence of significant oscillations with photon energy.

For the 14-ML film, one finds similar behavior regarding the overall CIS intensity distribution (Fig. 43b). In particular, the relative heights of the main maxima for *A*, *B*, and *C* are close to their counterparts of semi-infinite Cu(001). The main differences are distinct intensity oscillations, which become clearly visible in the insets showing the logarithm of the intensities. In particular, maxima *A* and *B* show almost the same oscillation period, which is indicated by vertical lines in the inset of Figure 43b. The period for maximum *C*, however, differs significantly from those of *A* and *B*. Further, the spectral shapes of *A* and *B* are nearly identical and again differ from that of *C*; in particular, the double-peak structure near the maximum intensity occurs for both *A* and *B* but is missing for *C*. This double-peak structure is clearly due to the quantum-size induced oscillations of the CIS intensity. These findings show directly the different confinement strengths of the QWSs: strict confinement for *A* and *B*, less confinement for *C*.

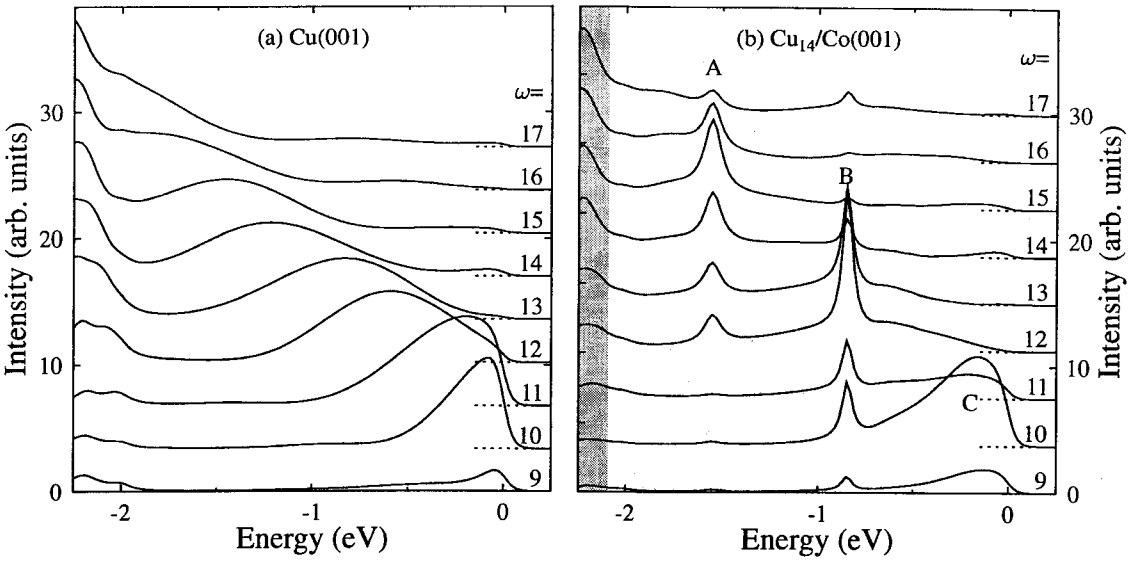

Fig. 42. Photoemission for $\mathbf{k}_{\parallel} = 0$ with p-polarized light incident at 45° off-normal from Cu(001) (a) and 14-ML Cu on fcc Co(001) (b). The photon energy ω ranges from 9 eV (bottom spectra) to 17 eV (top spectra), as indicated on the right. Gray areas in (b) indicate gaps in the Co band structure as in Figure 40. *A*, *B*, and *C* refer to quantum-well states (see text and Fig. 40). The Fermi energy is at 0 eV. Reprinted with permission from J. Henk and B. Johansson, *J. Electron Spectrosc. Relat. Phenom.* 105, 187 (1999). Copyright 1999, by Elsevier Science.

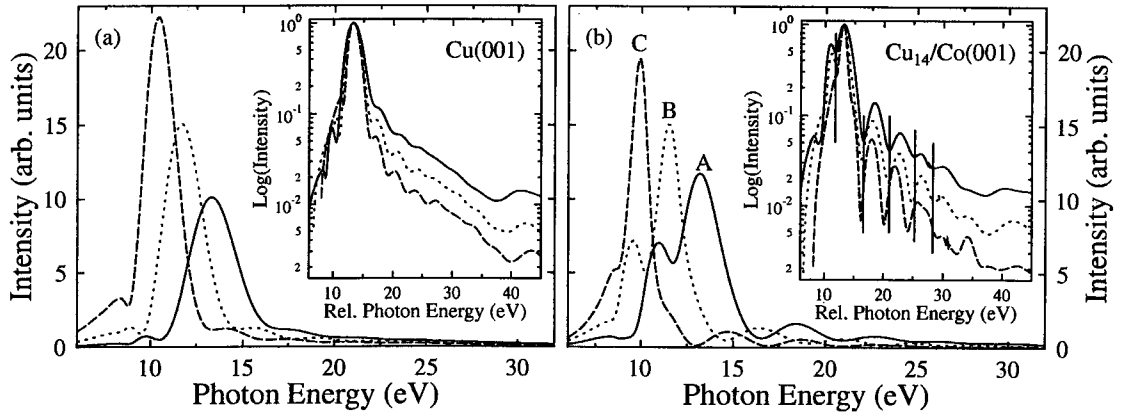

Fig. 43. Constant initial-state photoemission for $\mathbf{k}_{\parallel} = 0$ with p-polarized light incident at 45° off-normal from Cu(001) (a) and 14-ML Cu on fcc Co(001) (b). The initial-state energies are chosen as those of quantum-well states *A* (solid lines), *B* (dotted lines), and *C* (dashed lines); see text as well as Figures 40 and 42. Insets show the logarithms of the intensities, which are normalized to 1 and shifted in energy such that the maximum intensity is at 13 eV (relative photon energy). Vertical lines in the inset of (b) indicate intensity minima of state *A*. Reprinted with permission from J. Henk and B. Johansson, *J. Electron Spectrosc. Relat. Phenom.* 105, 187 (1999). Copyright 1999, by Elsevier Science.

Finally, the dependence of the oscillatory behavior on film thickness is addressed. According to Section 4.2.4, the oscillation period should decrease with increasing film thickness. For quantum-well state *A* of the 14-ML film and the corresponding states for films with thicknesses of 9 ML, 19 ML, 24 ML, and 29 ML, the energy positions are almost identical. This means that hole and photoelectron lifetimes are also almost identical, and the main differences in the CIS spectra can unambiguously be attributed to the difference in film thickness. Constant initial-state spectra for the various film thicknesses are shown in Figure 44. Both the width of the main maximum and the oscillation period decrease with film thickness. Further, the intensity at higher photon energies decreases with film thickness, which is also evident from Section 4.2.4, particularly from Figure 35. The double-peak structure can clearly be attributed to the quantum-size induced oscillations: For the Cu film, the main intensity maximum is broadened with respect to the semi-infinite case due to the weakening of the $k_{\perp}$ conservation, as is evident from Figure 44. This maximum is "divided" in two due to the intensity oscillations (cf. the dashed–dotted guideline in Fig. 44). With increasing film thickness, the double-peak structure disappears.

In summary, quantum-size effects in photoemission from ultra-thin films manifest themselves in the following features: (i) Strict confinement of valence electrons to the film leads to a weakening of the $k_{\perp}$ conservation: the thinner the film,

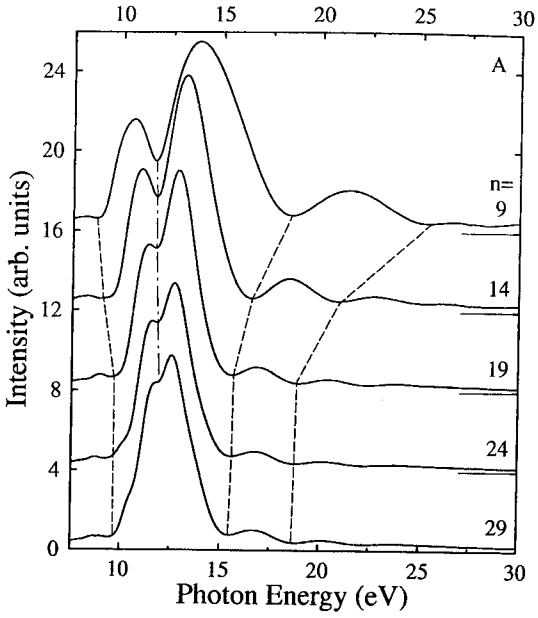

Fig. 44. Constant initial-state photoemission for $\mathbf{k}_{\parallel} = 0$ with p-polarized light incident at 45° off-normal from Cu films on fcc Co(001). The initial-state energies are chosen as those of quantum-well state A for selected film thicknesses n from 9 ML (top spectrum) to 29 ML (bottom spectrum), as indicated on the right. Dashed and dashed–dotted lines visualize the behavior of oscillations. Short horizontal lines represent zero intensity for each respective spectrum. Reprinted with permission from J. Henk and B. Johansson, *J. Electron Spectrosc. Relat. Phenom.* 105, 187 (1999). Copyright 1999, by Elsevier Science.

the broader the photoemission maxima. (ii) Photoemission intensities from individual QWSs show oscillations with photon energy, the period of which decreases with film thickness. (iii) Even for films only a few layers thick, the main maxima in the photoemission intensity follow the initial-state bulk-band structure, despite the fact that the initial-state energies are discrete.

Oscillations of Photoemission Intensity with Film Thickness. Another example of investigating QWSs at a fixed binding energy is illustrated in Figure 45. Kläsges et al. recorded experimentally the photocurrent at 0.3 eV binding energy and fixed photon energy ($\omega = 77$ eV) of Cu films on Co(100) for a variety of film thicknesses (1 ML–17 ML) [194]. Besides a global decrease of the intensity with film thickness, they found significant oscillations in the current, which, of course, can be attributed to QWSs. The period of the maxima was determined as 2.3 ML ± 0.1 ML.

Results of electronic-structure calculations of Cu films on Co(100) are shown in Figure 45b. Dederich's group calculated self-consistently the Bloch spectral function $A_B(\mathbf{k}_{\parallel}, E) = -\operatorname{Im} G(\mathbf{k}_{\parallel}; E)/\pi$. Each maximum in A_B in the sp-band range indicates a QWS (filled circles in Fig. 45b). Again, one finds the familiar dispersion with film thickness, as discussed in Section 2.2. With increasing film thickness, the QWSs disperse in energy toward the Fermi level, as visualized, by the dashed lines. The latter cross the binding energy of 0.3 eV with a period of 2.4 ML, which corresponds nicely to the experimentally obtained value. Because the photoemission intensity shows a maximum at the energy position of a QWS, the dispersion of the QWSs can be translated into a dispersion of the photoemission maxima. As shown in Figure 45a, a model photoemission calculation reproduces all general features found in the experimental results, in particular, the global decay and the oscillations. The model assumes that each QWS contributes to the photocurrent with a finite peak width corresponding to the experimental energy resolution. Further, this intensity is expected to be proportional to the inverse of the film thickness. The background intensity due to the Co substrate is approximated as decaying

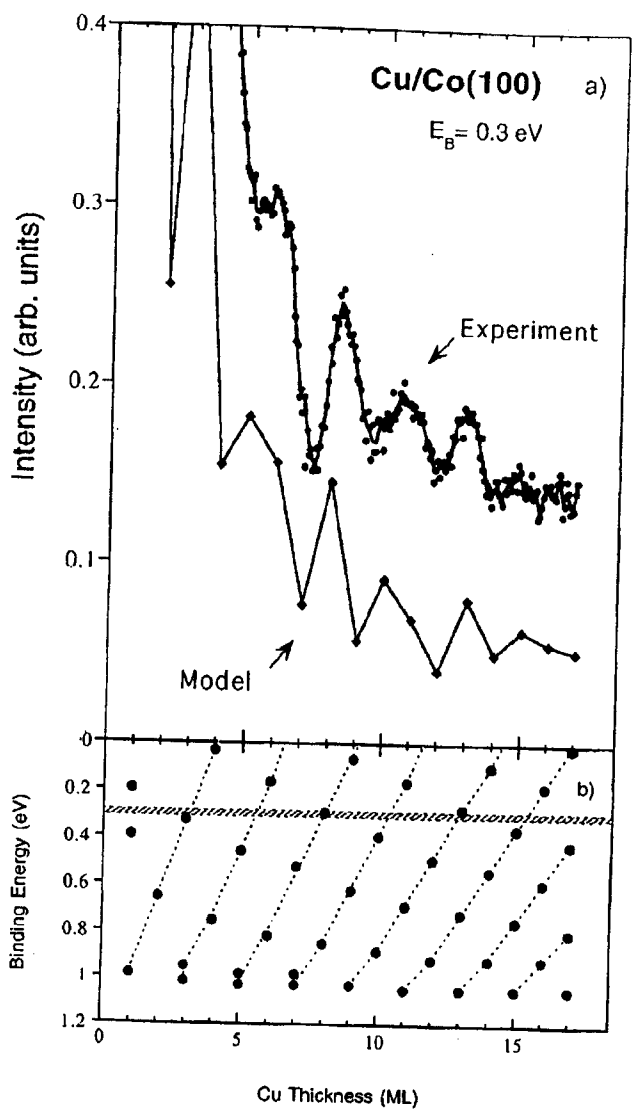

Fig. 45. Photoemission intensity from Cu films on Co(100) at 0.3 eV binding energy versus Cu film thickness. The emission angle chosen is 12° ($\mathbf{k}_{\parallel} = 0.94$ Å^{-1}). (a) Shows experimental data (dots) and results of a model calculation (solid line). Binding energies of quantum-well states are shown in (b). Dashed lines serve as a guide to the eye. The hatched area indicates the binding energy as chosen in the photoemission experiment. Reprinted with permission from R. Kläsges, D. Schmitz, C. Carbone, W. Eberhardt, P. Lang, R. Zeller, and P. H. Dederichs, *Phys. Rev. B.* 57, R696 (1998). Copyright 1998, by the American Physical Society.

exponentially with Cu thickness, in accordance with the mean free path of the photoelectron (Fig. 12). This causes the global decay of the intensity. Missing are, however, interference effects in both the initial and the final state of the photoemission process. These can, for example, lead to significant changes in the photocurrent that call into question the one-to-one correspondence between maxima in the Bloch spectral function and the photocurrent maxima. These effects have been observed, for example, for Co/Cu(001) [201] and Au/Ag(111) [202]: Due to destructive interference in the final state at a particular kinetic energy, only one of two QWSs of the 2-ML films has been observed in both experiment and theory although the layer- and symmetry-resolved Bloch spectral function of both states shows maxima of comparable height. The effect of interference is discussed in more detail in the following Section.

4.3.2. Quantum-Well States and Interference: Ag on Fe(001)

Particle wave duality is one of the fundamental features of quantum mechanics. We now investigate how photoemission from a thin film establishes an almost perfect analogy between a standing electromagnetic wave caught between two mirrors and an electron confined to a thin film.

Consider an electron confined to a quantum well, the latter, for example, being realized by a thin film (Fig. 46). The electron is reflected at both the surface side (s) and the substrate side (interface, i) of the film with reflection coefficients $R_s = |R_s|\exp(i\phi_s)$ and $R_i = |R_i|\exp(i\phi_i)$, respectively. The propagation from one side to the other is taken into account via the phase factors P^+ and P^-. For $\mathbf{k}_\parallel = 0$, these read $P^\pm = \exp(ik_\perp Nd)$, where N is the number of layers of the film, d is the interlayer distance, and $k_\perp$ is the wave number of the electron. The Bohr–Sommerfeld quantization rule, which is well known from the theory of atomic spectra, then reads $2k_\perp Nd + \phi_s + \phi_i = 2n\pi$, $n \in \mathbb{Z}$. In other words, constructive interference occurs if the accumulated phase shift is an even multiple of π. This relation is known as the round-trip criterion

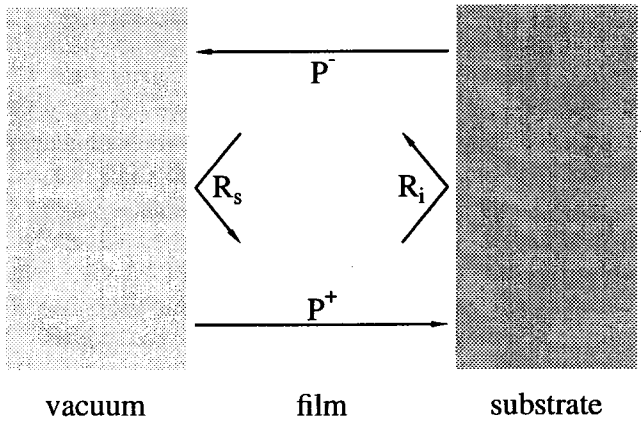

Fig. 46. Electron confined to a quantum well. Arrows $P^\pm$ denote propagation between the interfaces (vacuum–film and film–substrate). R_i and R_s are the reflectivities at the film boundaries.

(see Sections 2.2.2 and 3.3) and holds for perfectly reflecting boundaries ($|R_s| = |R_i| = 1$).

The more general case can be discussed in terms of an interference factor I. For each round trip, the wave function of the electron is changed by the factor $P^+R_sP^-R_i$, with $P^\pm = \exp(i\mathbf{k}^\pm \cdot \mathbf{d})$. For $\mathbf{k}_\parallel = 0$, the interference factor I then becomes

$$I = \sum_{j=0}^{\infty}(P^+R_sP^-R_i)^j = \left(1 - R\exp\left(i(\phi + 2k_\perp Nd)\right)\exp\left(-Nd/\lambda\right)\right)^{-1} \quad (199)$$

with the definitions $R = |R_sR_i|$ and $\phi = \phi_s + \phi_i$. Note that the mean free path λ is taken into account. The modulus of the interference factor is given by

$$|I|^2 = \left(1 - R\exp\left(-\frac{Nd}{\lambda}\right)\right)^{-2} \times \left[1 + \left(\frac{2f}{\pi}\right)^2 \sin^2\left(k_\perp Nd + \frac{\phi}{2}\right)\right]^{-1} \quad (200)$$

with

$$f = \frac{\pi\sqrt{R}\exp\left(-Nd/2\lambda\right)}{1 - R\exp\left(-Nd/\lambda\right)} \quad (201)$$

f is the finesse (i.e., the ratio of peak separation and peak width) of a Fabry–Pérot interferometer with an absorptive medium ($\lambda < \infty$). Such a device was invented by Fabry and Pérot in 1899 [203]. Equation (200) establishes the close analogy between interference of electromagnetic waves and of electrons (cf., e.g., [204]).

The first factor in Eq. (200), $(1 - R\exp(-Nd/\lambda))^{-2}$, depends on both the mean free path λ and the reflectivity R, quantities that are expected to depend rather smoothly on energy. The same holds for the finesse f and the phase shift ϕ. Therefore, the modulation of the interference factor can be mainly attributed to the wave number $k_\perp$. Assuming the first factor, the finesse, and the phase shift as energy independent, the interference factor becomes approximately

$$|I|^2 \approx \left[1 + \left(\frac{2f}{\pi}\right)^2 \sin^2\left(k_\perp(E)Nd + \frac{\phi}{2}\right)\right]^{-1} \quad (202)$$

which is shown in Figure 47. Maxima in $|I|^2$ occur if $\sin^2(k_\perp(E)Nd + \phi/2) = 0$ or, equivalently, if $k_\perp(E) = (n\pi - \phi/2)/(Nd)$, $n \in \mathbb{Z}$.

The relevant quantities that determine the interference can be cast into two categories. (i) The wave number $k_\perp(E)$ and the mean free path $\lambda(E)$ depend on the band structure of the film material. Because the electrons can be described as quasiparticles, the band structure $k_\perp(E, \mathbf{k}_\parallel)$ is, in general, complex (cf. Section 3.2.2). The imaginary part of $k_\perp$ is related to the mean free path by the group velocity $v_\perp = \partial_{k_\perp}E(k_\perp)$, $\lambda = v_\perp/\operatorname{Im}k_\perp(E)$. (ii) The reflectivity R and the phase shift ϕ depend on the quantum-well boundaries, in particular, on the reflection properties at the film–substrate interface. For thick films, R and ϕ can be regarded as independent of the film thickness Nd. Therefore, one can expect to determine them by

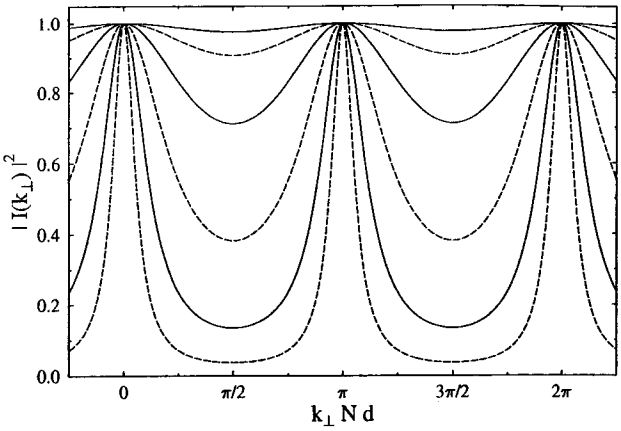

Fig. 47. Interference factor $I(k_\perp)$ for a Fabry–Pérot-type quantum well as a function of wave number $k_\perp$ for finesses 0.5, 1.0, 2.0, 4.0, 8.0, and 16.0 (from top to bottom, alternating solid and dashed lines). N and d are the number of layers and the interlayer distance of the film, respectively. The phase shift ϕ is chosen as 0; cf. Eq. (202).

ARPES from films with different thicknesses Nd. For very thin films, however, the interfaces (surface side and substrate side) cannot be separated and R and ϕ should differ considerably from their values for thicker films. This becomes evident by comparing reflectivities for various film thicknesses, as, for example, shown in Figure 41. The peak positions depend on $k_\perp$ and ϕ, the peak widths on R and λ.

If the film were infinitely thick, the photocurrent J_s would be expressed in the form of Fermi's golden rule, Eq. (141). However, for a finite thickness, the initial state $|i\rangle$ can be seen as modulated by the interference factor I, Eq. (200), and thus is given by $I_i|i\rangle$ [205]. Therefore, the photocurrent from the film with finite thickness reads

$$J_{qw} \sim \sum_i |I_i|^2 |\langle f|\mathbf{A}\cdot\mathbf{p}|i\rangle|^2 \delta(E_f - \omega - E_i) \qquad (203)$$

The task to determine the interference-determining quantities $k_\perp$, ϕ, R, and λ might be complicated by several facts. (i) The growth of the film material on the substrate should be in the layer-by-layer mode, which leads to well-defined film boundaries and minimizes film imperfections. (ii) The electronic properties of the film and the substrate should "match". In other words, they should allow for QWSs; for example, there has to be a gap in the band structure of the substrate. (iii) In general, several initial states $|i\rangle$ contribute to the total photocurrent in the considered energy range and, thus, one has to deal with a set of parameters for each initial state. Fortunately, there are systems in which only a single initial state is present in the considered energy range.

Paggel et al. reported on an experimental investigation of the interference properties of Ag films on Fe(001) [206], another prototypical system. In the considered initial-energy range (−2 eV up to 0 eV) and the chosen photon energy, the spectrum for semi-infinite Ag looks almost structureless. Therefore, the intensity modulations due to the Ag films can be easily identified (cf. Fig. 48). Further, Ag films grow in a layer-by-layer

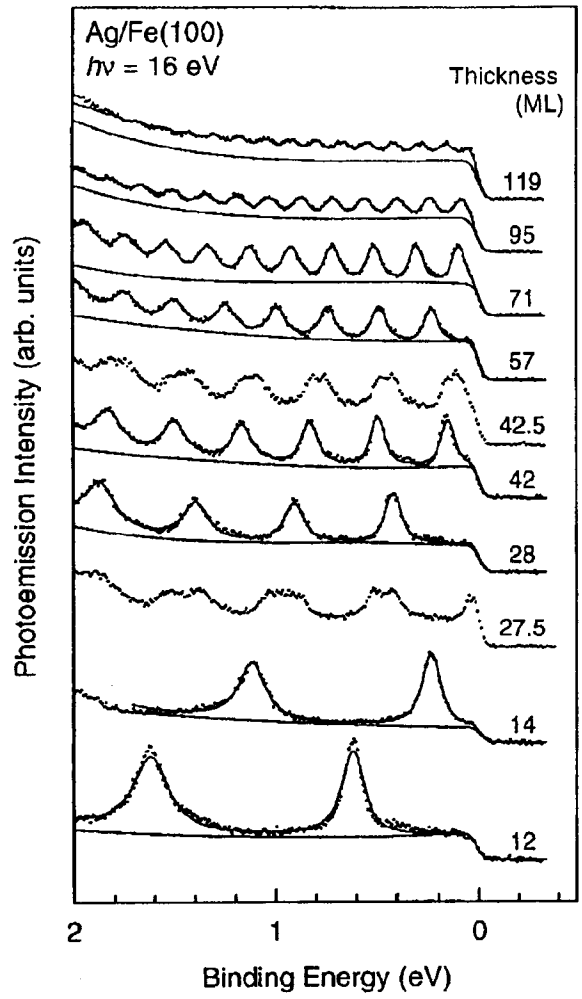

Fig. 48. Photoemission spectra for Ag films on Fe(001) for various film thicknesses in monolayers (ML), as indicated on the right of each spectrum. The experimental data (given by dots) were recorded for normal emission ($\mathbf{k}_\parallel = 0$) and 16 eV photon energy. Solid lines correspond to the fitted interference spectra and the background. Reprinted with permission from J. J. Paggel, T. Miller, and T.-C. Chiang, *Science* 283, 1709 (1999). Copyright 1999, by the American Association for the Advancement of Science.

mode on Fe(001), which allows for a very accurate thickness calibration via the observed intensity modulation. As an example, the spectrum for a film with thickness 27.5 ML shows simultaneously the peak structures of films with 27 and 28 ML. The modulated intensity appears as a superposition of those of the latter films (this holds, in addition, for the 42.5-ML film).

To determine the reflectivity R, the phase shift ϕ, and the mean free path λ, one has to know the initial-state band structure of Ag. The latter can be obtained either by the photoemission experiment itself, for instance, via band mapping using various photon energies or by a band structure calculation. The relevant band in the considered energy range is the sp valence band, which is roughly a free-electron parabola; see Figure 49a (cf., e.g., the band structure of Cu in Figure 40, which shows an sp band, too). Applying a fitting procedure, Paggel et al. obtained $R(E)$, $\phi(E)$, and $\lambda(E)$, which are assumed to be independent of the film thickness. The resulting

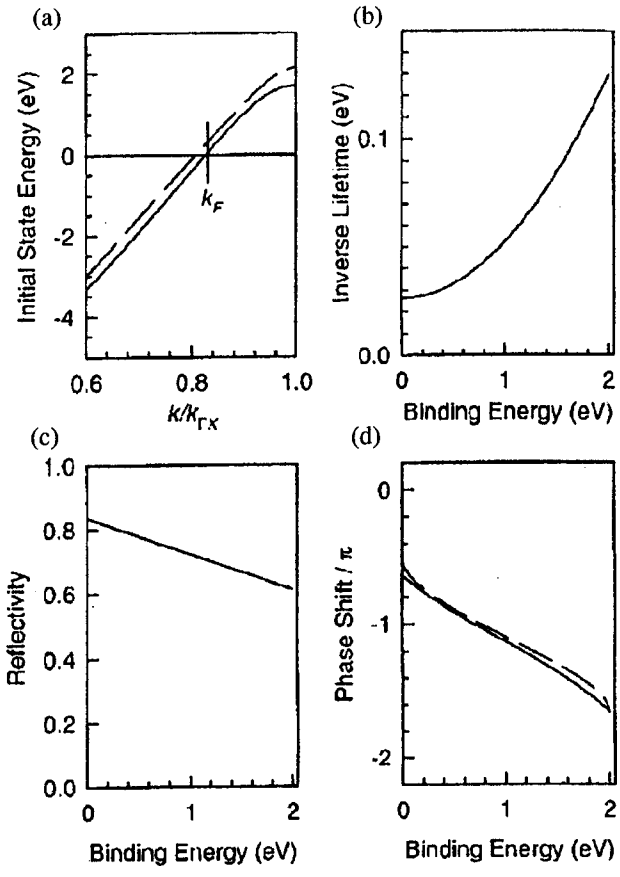

Fig. 49. Electronic structure of Ag films on Fe(100). Panel a shows the Ag band structure near the Fermi energy (i.e., the *sp* band range). The solid line corresponds to the experimentally determined dispersion of the *sp* band, the dashed line to one theoretically obtained. Panel b depicts the inverse lifetime as obtained from the experimental data. Panels c and d show the reflection coefficients and the phase shift at the Ag/Fe interface. Reprinted with permission from J. J. Paggel, T. Miller, and T.-C. Chiang, *Science* 283, 1709 (1999). Copyright 1999, by the American Association for the Advancement of Science.

theoretical modulated intensities are shown in Figure 48 and match almost perfectly the experimental ones for all film thicknesses. Note that the peak shapes in the experimental spectra agree very well with that of the interference factor I shown in Figure 47. The determined reflectivity R was less than unity ($R \in [0.6, 0.85]$, Fig. 49c), indicating that the electrons are not strictly confined to the Ag film. This can be attributed to the fact that the bandgap in the Fe substrate is not an absolute one but a hybridization bandgap. In the former case, there are no states in the bandgap energy range, whereas in the latter, there are states with different spatial symmetry, which, however, are mixed by SOC. Further, the small, but not negligible lattice mismatch between Ag and Fe leads to nonspecular reflection at the boundaries. The inverse lifetime depends quadratically on the binding energy (Fig. 49b and [207]), as in Fermi liquid theory.

Acknowledgments

It is a great pleasure to thank those colleagues who have made the present chapter possible. Unfortunately, it is nearly impossible to acknowledge them all. Therefore, I want to mention only four to whom I am especially grateful: Roland Feder, Samed Halilov, Thomas Scheunemann, and Eiichi Tamura.

REFERENCES

1. L. Bennett and R. Watson, Eds., "Magnetic Multilayers." World Scientific, Singapore, 1993.
2. J. Bland and B. Heinrich, "Ultrathin Magnetic Structures." Springer-Verlag, Berlin, 1994.
3. A. Barthélémy, A. Fert, and F. Petroff, *In* "Handbook of Magnetic Materials" (K. H. J. Buschow, Ed.), Vol. 12, p. 1. Elsevier, Amsterdam, 1999.
4. J. M. Daughton, *J. Magn. Magn. Mater.* 192, 334 (1999).
5. U. Hartmann, Ed., "Magnetic Multilayers and Giant Magnetoresistance: Fundamentals and Industrial Applications," Springer Series in Surface Sciences, Vol. 37. Springer-Verlag, Berlin, 1999.
6. A. Zangwill, "Physics at Surfaces." Cambridge Univ. Press, Cambridge, UK, 1988.
7. N. Ashcroft and N. Mermin, "Solid State Physics." Holt–Saunders, London, 1976.
8. L. Brillouin, "Wave Propagation in Periodic Structures." McGraw–Hill, New York, 1946.
9. R. L. Park and H. H. Madden, *Surf. Sci.* 11, 188 (1968).
10. S. Gull, A. Lasenby, and C. Doran, *Found. Phys.* 23, 1175 (1993).
11. T. G. Vold, *Am. J. Phys.* 61, 491 (1993).
12. G. Ertl and J. Küppers, "Low Energy Electrons and Surface Chemistry," Chap. 9, p. 201. VCH, Weinheim, 1985.
13. F. Bloch, *Z. Phys.* 52, 555 (1928).
14. P. Harrison, "Quantum Wells, Wires and Dots." Wiley, Chichester, 2000.
15. E. Merzbacher, "Quantum Mechanics," 2nd ed. Wiley, New York, 1970.
16. K. R. Brownstein, *Am. J. Phys.* 68, 160 (2000).
17. H. A. Kramers, *Koniklije Nederlandse Akademie van Wetenschapen* 33, 959 (1930).
18. G. Bastard, *Phys. Rev. B* 24, 5693 (1981).
19. G. Bastard, *Phys. Rev. B* 25, 7584 (1982).
20. P. D. Loly and J. B. Pendry, *J. Phys. C: Solid State Phys.* 16, 423 (1983).
21. J. E. Ortega, F. J. Himpsel, G. J. Mankey, and R. F. Willis, *Phys. Rev. B* 47, 1540 (1993).
22. M. Grüne, T. Pelzer, K. Wandelt, and I. T. Steinberger, *J. Electron Spectrosc. Relat. Phenom.* 98–99, 121 (1999).
23. K. Horn, M. Scheffler, and A. M. Bradshaw, *Phys. Rev. Lett.* 41, 822 (1978).
24. M. Scheffler, K. Horn, A. M. Bradshaw, and K. Kambe, *Surf. Sci.* 80, 69 (1979).
25. K. Kambe, *Surf. Sci.* 105, 95 (1981).
26. P. Trischberger, H. Dröge, S. Gokhale, J. Henk, H.-P. Steinrück, W. Widdra, and D. Menzel, *Surf. Sci.* 377–379, 155 (1996).
27. W. Widdra, P. Trischberger, and J. Henk, *Phys. Rev. B* 60, R5161 (1999).
28. C. Davisson and L. H. Germer, *Nature* 119, 558 (1927).
29. C. J. Davisson and L. H. Germer, *Phys. Rev.* 30, 705 (1927).
30. L. de Broglie, *Comte Rendu* 179, 676 (1924).
31. L. de Broglie, *Comte Rendu* 179, 1039 (1924).
32. L. de Broglie, *Comte Rendu* 180, 498 (1925).
33. J. F. van Veen and M. A. van Hove, Eds., "The Structure of Surfaces II," Springer Series in Surface Sciences, Vol. 11. Springer-Verlag, Berlin, 1988.
34. S. Y. Tong, M. A. van Hove, K. Takayanagi, and X. D. Xie, Eds., "The Structure of Surfaces III," Springer Series in Surface Sciences, Vol. 24. Springer-Verlag, Berlin, 1991.
35. C. Davisson and L. H. Germer, *Phys. Rev.* 31, 307 (1928).
36. C. Davisson and L. H. Germer, *Phys. Rev.* 31, 155 (1928).
37. M. P. Seah and W. A. Dench, *Surf. Interface Anal.* 1, 2 (1979).
38. Z.-J. Ding and R. Shimizu, *Surf. Sci.* 222, 313 (1989).
39. J. Rundgren, *Phys. Rev. B* 59, 5106 (1999).
40. C. J. Davisson, *J. Franklin Inst.* 205, 597 (1928).

41. K. Heinz, U. Starke, and J. Bernhardt, *Prog. Surf. Sci.* 64, 163 (2000).
42. K. Kambe, *Z. Naturforsch., A: Phys. Sci.* 22, 322 (1967).
43. K. Kambe, *Z. Naturforsch., A: Phys. Sci.* 22, 422 (1967).
44. K. Kambe, *Z. Naturforsch., A: Phys. Sci.* 22, 1280 (1967).
45. J. B. Pendry, "Low Energy Electron Diffraction." Academic Press, London, 1974.
46. M. A. van Hove, W. H. Weinberg, and C. M. Chan, "Low-Energy Electron Diffraction." Springer-Verlag, Berlin, 1986.
47. S. Y. Tong, *In* "Progress in Surface Science" (S. G. Davisson, Ed.), Vol. 7, p. 1. Pergamon, London, 1975.
48. M. A. van Hove and S. Y. Tong, "Surface Crystallography by LEED: Theory, Computation and Structural Results," Springer Series in Chemical Physics, Vol. 2. Springer-Verlag, Berlin, 1979.
49. R. Feder, *Solid State Commun.* 31, 821 (1979).
50. R. Feder and J. Kirschner, *Surf. Sci.* 103, 75 (1981).
51. R. Feder, *In* "Polarized Electrons in Surface Physics" (R. Feder, Ed.). Advanced Series in Surface Science, Chap. 4, p. 125. World Scientific, Singapore, 1985.
52. J. Kirschner and R. Feder, *Phys. Rev. Lett.* 42, 1008 (1979).
53. J. C. Slater, *Phys. Rev.* 51, 840 (1937).
54. V. N. Strocov, R. Claessen, G. Nicolay, S. Hüfner, A. Kimura, A. Harasawa, S. Shin, A. Kakizaki, P. O. Nilsson, H. I. Starnberg, and P. Blaha, *Phys. Rev. Lett.* 81, 4943 (1998).
55. I. Bartoš, *Prog. Surf. Sci.* 59, 197 (1998).
56. V. Heine, *Proc. Phys. Soc.* 81, 300 (1963).
57. Y.-C. Chang, *Phys. Rev. B* 25, 605 (1982).
58. J. Hermanson, *Solid State Commun.* 22, 9 (1977).
59. T. Inui, Y. Tanabe, and Y. Onodera, "Group Theory and Its Applications in Physics," 1st ed., Springer Series in Solid State Sciences, Vol. 78. Springer-Verlag, Berlin, 1990.
60. J. B. Pendry, *J. Phys. C: Solid State Phys.* 2, 1215 (1969).
61. J. B. Pendry, *J. Phys. C: Solid State Phys.* 2, 2273 (1969).
62. J. B. Pendry, *J. Phys. C: Solid State Phys.* 2, 2283 (1969).
63. V. N. Strocov, H. I. Starnberg, and P. O. Nilsson, *J. Phys.: Condens. Matter* 8, 7539 (1996).
64. V. N. Strocov, H. I. Starnberg, and P. O. Nilsson, *J. Phys.: Condens. Matter* 8, 7549 (1996).
65. J. Henk, W. Schattke, H.-P. Barnscheidt, C. Janowitz, R. Manzke, and M. Skibowski, *Phys. Rev. B* 39, 13286 (1989).
66. J. Henk, J.-V. Peetz, and W. Schattke, *In* "20th International Conference on the Physics of Semiconductors" (E. M. Anastassakis and J. D. Joannopoulos, Eds.), Vol. 1, pp. 175–178. World Scientific, Singapore, 1990.
67. J. Henk, W. Schattke, H. Carstensen, R. Manzke, and M. Skibowski, *Phys. Rev. B* 47, 2251 (1993).
68. S. Lorenz, C. Solterbeck, W. Schattke, J. Burmeister, and W. Hackbusch, *Phys. Rev. B* 55, R13432 (1997).
69. W. Schattke, *Prog. Surf. Sci.* 64, 89 (2000).
70. I. Mertig, E. Mrosan, and P. Ziesche, "Multiple Scattering Theory of Point Defects in Metals: Electronic Properties," Teubner-Texte zur Physik, Vol. 11. Teubner, Leipzig, 1987.
71. P. Weinberger, "Electron Scattering Theory of Ordered and Disordered Matter," Clarendon, Oxford, 1990.
72. A. Gonis, "Green Functions for Ordered and Disordered Systems," Studies in Mathematical Physics, Vol. 4. North-Holland, Amsterdam, 1992.
73. J. Korringa, *Physica* 13, 392 (1947).
74. W. Kohn and N. Rostoker, *Phys. Rev.* 94, 1111 (1954).
75. J. M. MacLaren, S. Crampin, D. D. Vvedensky, and J. B. Pendry, *Phys. Rev. B* 40, 12164 (1989).
76. E. M. Rose, "Relativistic Electron Theory." Wiley, New York, 1961.
77. S. Bei der Kellen and A. J. Freeman, *Phys. Rev. B* 54, 11187 (1996).
78. A. Gonis, P. Turchi, J. Kudrnovský, V. Drchal, and I. Turek, *J. Phys.: Condens. Matter* 8, 7869 (1996).
79. J. W. Krewer, "Beugung spinpolarisierter langsamer Elektronen (SPLEED) mit nicht-sphärischen Potentialen," Ph.D. Dissertation, Universität Duisburg, 1990.
80. J. W. Krewer and R. Feder, *Physica B* 172, 135 (1991).
81. M. Abramowitz and I. Stegun, Eds., "Handbook of Mathematical Functions." Dover, New York, 1965.
82. E. Tamura, *Phys. Rev. B* 45, 3271 (1992).
83. B. Ackermann, "Relativistische Theorie der Photoemission und Streuung langsamer Elektronen von ferromagnetischen Oberflächen," Ph.D. Thesis, Universität Duisburg, 1985.
84. D. D. Koelling and B. N. Harmon, *J. Phys. C: Solid State Phys.* 10, 3107 (1977).
85. H. Gollisch and L. Fritsche, *Phys. Status Solidi B* 86, 156 (1978).
86. T. Takeda, *J. Phys. F: Met. Phys.* 9, 815 (1979).
87. E. Tamura, private communication.
88. H. Ebert, H. Freyer, A. Vernes, and G. Y. Guo, *Phys. Rev. B* 53, 7721 (1996).
89. H. Ebert, H. Freyer, and M. Deng, *Phys. Rev. B* 56, 9454 (1997).
90. L. A. Mac Coll, *Phys. Rev.* 56, 699 (1939).
91. R. Jones, P. Jennings, and O. Jepsen, *Phys. Rev. B* 29, 6474 (1984).
92. E. Tamura and R. Feder, *Z. Phys. B: Condens. Matter* 81, 425 (1990).
93. C. S. Lent and D. J. Kirkner, *J. Appl. Phys.* 67, 6353 (1990).
94. Y. Joly, *Phys. Rev. Lett.* 68, 950 (1992).
95. R. Feder, *J. Phys. C: Solid State Phys.* 14, 2049 (1981).
96. J. Kessler, "Polarized Electrons," 2nd ed., Springer Series on Atoms and Plasmas, Vol. 1. Springer-Verlag, Berlin, 1985.
97. R. Feder, Ed., "Polarized electrons in surface physics," Advanced Series in Surface Science. World Scientific, Singapore, 1985.
98. E. Zanazzi and F. Jona, *Surf. Sci.* 62, 61 (1977).
99. J. B. Pendry, *J. Phys. C: Solid State Phys.* 13, 937 (1980).
100. E. Tamura, R. Feder, G. Waller, and U. Gradmann, *Phys. Status Solidi B* 157, 627 (1990).
101. O. Hjortstam, J. Trygg, J. M. Wills, B. Johansson, and O. Eriksson, *Phys. Rev. B* 53, 9204 (1996).
102. I. Delgadillo, H. Gollisch, and R. Feder, *Phys. Rev. B* 50, 15808 (1994).
103. R. Feder, B. Awe, and E. Tamura, *Surf. Sci.* 157, 183 (1985).
104. E. Tamura, R. Feder, J. Krewer, R. E. Kirby, E. Kisker, E. L. Garwin, and F. K. King, *Solid State Commun.* 55, 543 (1985).
105. P. Bruno, *J. Phys.: Condens. Matter* 11, 9403 (1999).
106. T. Scheunemann, R. Feder, J. Henk, E. Bauer, T. Duden, H. Pinkvos, H. Poppa, and K. Wurm, *Solid State Commun.* 104, 787 (1997).
107. B. Johnson, P. Berlowitz, D. Goodman, and C. Bartholomew, *Surf. Sci.* 217, 13 (1989).
108. J. G. Ociepa, P. J. Schultz, K. Griffiths, and P. R. Norton, *Surf. Sci.* 225, 281 (1990).
109. M. Tikhov and E. Bauer, *Surf. Sci.* 232, 73 (1990).
110. H. Knoppe and E. Bauer, *Phys. Rev. B* 48, 1794 (1993).
111. E. Bauer, *Rep. Prog. Phys.* 57, 895 (1994).
112. L. M. Falicov and J. Ruvalds, *Phys. Rev.* 172, 498 (1968).
113. C. M. Schneider, P. Bressler, P. Schuster, J. Kirschner, J. J. de Miguel, and R. Miranda, *Phys. Rev. Lett.* 64, 1059 (1990).
114. H. Bonzel and C. Kleint, *Prog. Surf. Sci.* 49, 107 (1995).
115. H. Hertz, *Ann. Phys. Chem. Neue Folge* 31, 983 (1887).
116. W. Hallwachs, *Ann. Phys. Chem. Neue Folge* 33, 301 (1888).
117. J. Elster and H. Geitel, *Ann. Phys. Chem. Neue Folge* 38, 40 (1889).
118. J. Elster and H. Geitel, *Ann. Phys. Chem. Neue Folge* 38, 497 (1889).
119. P. Lenard, *Ann. Phys.* 8, 149 (1902).
120. A. Einstein, *Ann. Phys.* 17, 132 (1905).
121. K. Siegbahn, C. Nordling, A. Fahlman, R. Nordberg, K. Hamrin, J. Hedman, G. Johanson, T. Bergmark, S.-E. Karlsson, I. Lindgren, and B. Lindberg, "ESCA–Atomic, Molecular and Solid State Structure Studied by Means of Electron Spectroscopy." Almqvist & Wiksell, Uppsala, 1967.
122. E. O. Kane, *Phys. Rev. Lett.* 12, 97 (1964).
123. M. Campagna and R. Rosei, Eds., "Photoemission and Absorption Spectroscopy of Solids and Interfaces with Synchrotron Radiation." North-Holland, Amsterdam, 1990.
124. R. Z. Bachrach, Ed., "Technique," Synchrotron Radiation Research: Advances in Surface and Interface Science, Vol. 1. Plenum, New York, 1992.
125. R. Z. Bachrach, Ed., "Issues and Technology," Synchrotron Radiation Research: Advances in Surface and Interface Science, Vol. 2. Plenum, New York, 1992.

126. C. Berglund and W. Spicer, *Phys. Rev.* 136, A1030 (1964).
127. M. Cardona and L. Ley, Eds., "Photoemission in Solids I," Topics in Applied Physics, Vol. 26. Springer-Verlag, Berlin, 1978.
128. A. Liebsch, *In* "Photoemission and the Electronic Properties of Surfaces" (B. Feuerbacher, B. Fitton, and R. F. Willis, Eds.), p. 167. Wiley, Chichester, 1978.
129. S. V. Kevan, Ed., "Angle-Resolved Photoemission: Theory and Current Applications." Elsevier, Amsterdam, 1992.
130. I. Adawi, *Phys. Rev. A* 134, 788 (1964).
131. G. D. Mahan, *Phys. Rev. B* 2, 4334 (1970).
132. G. D. Mahan, *Phys. Rev. Lett.* 24, 1068 (1970).
133. W. L. Schaich and N. W. Ashcroft, *Phys. Rev. B* 3, 2452 (1971).
134. D. C. Langreth, *Phys. Rev. B* 3, 3120 (1971).
135. J. B. Pendry, *J. Phys. C: Solid State Phys.* 8, 2431 (1975).
136. J. B. Pendry, *Surf. Sci.* 57, 679 (1976).
137. J. F. L. Hopkinson, J. B. Pendry, and D. J. Titterington, *Comput. Phys. Commun.* 19, 69 (1980).
138. G. Thörner and G. Borstel, *Phys. Status Solidi B* 126, 617 (1984).
139. J. Braun, G. Thörner, and G. Borstel, *Phys. Status Solidi B* 130, 643 (1985).
140. J. Braun, G. Thörner, and G. Borstel, *Phys. Status Solidi B* 144, 609 (1987).
141. M. Wöhlecke and G. Borstel, *In* "Optical Orientation" (F. Meier and B. P. Zakharchenya, Eds.), North-Holland, Amsterdam, 1984.
142. E. Tamura, W. Piepke, and R. Feder, *Phys. Rev. Lett.* 59, 934 (1987).
143. E. Tamura and R. Feder, *Europhys. Lett.* 16, 695 (1991).
144. J. Henk and R. Feder, *Europhys. Lett.* 28, 609 (1994).
145. B. Ginatempo, P. J. Durham, B. L. Gyorffy, and W. M. Temmerman, *Phys. Rev. Lett.* 54, 1581 (1985).
146. B. Schmiedeskamp, B. Vogt, and U. Heinzmann, *Phys. Rev. Lett.* 60, 651 (1988).
147. B. Schmiedeskamp, N. Irmer, R. David, and U. Heinzmann, *Appl. Phys. A* 53, 418 (1991).
148. N. Irmer, F. Frentzen, S.-W. Yu, B. Schmiedeskamp, and U. Heinzmann, *J. Electron Spectrosc. Relat. Phenom.* 78, 321 (1996).
149. R. Feder, F. Rosicky, and B. Ackermann, *Z. Phys. B: Condens. Matter* 52, 31 (1983).
150. R. Feder and J. Henk, *In* "Spin-Orbit Influenced Spectroscopies of Magnetic Solids" (H. Ebert and G. Schütz, Eds.), Lecture Notes in Physics, Vol. 466, p. 85. Springer-Verlag, Berlin, 1996.
151. W. Kuch, A. Dittschar, K. Meinel, M. Zharnikov, C. Schneider, J. Kirschner, J. Henk, and R. Feder, *Phys. Rev. B* 53, 11621 (1996).
152. A. Fanelsa, E. Kisker, J. Henk, and R. Feder, *Phys. Rev. B* 54, 2922 (1996).
153. A. Rampe, G. Güntherodt, D. Hartmann, J. Henk, T. Scheunemann, and R. Feder, *Phys. Rev. B* 57, 14370 (1998).
154. P. J. Durham, *J. Phys. F: Met. Phys.* 11, 2475 (1981).
155. P. J. Durham, J. Staunton, and B. L. Gyorffy, *J. Magn. Magn. Mater.* 45, 38 (1984).
156. P. Feibelman and D. Eastman, *Phys. Rev. B* 10, 4932 (1974).
157. C. Caroli, D. Lederer-Rozenblatt, B. Roulet, and D. Saint-James, *Phys. Rev. B* 8, 4552 (1973).
158. H. Gollisch, D. Meinert, E. Tamura, and R. Feder, *Solid State Commun.* 82, 197 (1992).
159. W. Schattke, *Prog. Surf. Sci.* 54, 211 (1997).
160. L. Hedin, J. Michiels, and J. Inglesfield, *Phys. Rev. B* 58, 15565 (1998).
161. L. Hedin, *J. Phys.: Condens. Matter* 11, R489 (1999).
162. T. Fujikawa and L. Hedin, *Phys. Rev. B* 40, 11507 (1989).
163. S. Lundqvist and N. H. March, Eds., "Theory of the Inhomogenous Electron Gas." Plenum, New York, 1983.
164. A. Liebsch, *Phys. Rev. Lett.* 43, 1431 (1979).
165. A. Goldmann, R. Matzdorf, and F. Theilmann, *Surf. Sci.* 414, L932 (1998).
166. R. Matzdorf, *Surf. Sci. Rep.* 30, 154 (1998).
167. J. Braun, *Rep. Prog. Phys.* 59, 1267 (1996).
168. P. M. Morse and H. Feshbach, "Methods of Theoretical Physics," Vol. 1. McGraw–Hill, New York, 1953.
169. J. S. Faulkner and G. M. Stocks, *Phys. Rev. B* 21, 3222 (1980).
170. P. Braspenning and A. Lodder, *Phys. Rev. B* 49, 10222 (1994).
171. G. Grosso, S. Moroni, and G. P. Parravicini, *Phys. Scr., T* 25, 316 (1989).
172. L. Szunyogh, B. Újfalussy, and P. Weinberger, *Phys. Rev. B* 51, 9552 (1995).
173. K. Wildberger, R. Zeller, and P. H. Dederichs, *Phys. Rev. B* 55, 10074 (1997).
174. H. Bross, *Z. Phys. B: Condens. Matter* 28, 173 (1977).
175. J. Henk, A. M. N. Niklasson, and B. Johansson, *Phys. Rev. B* 59, 13986 (1999).
176. J. Henk, T. Scheunemann, S. Halilov, and R. Feder, *J. Phys.: Condens. Matter* 8, 47 (1996).
177. C. M. Schneider, J. J. de Miguel, P. Bressler, P. Schuster, R. Miranda, and J. Kirschner, *J. Electron Spectrosc. Relat. Phenom.* 51, 263 (1990).
178. W. Kuch, A. Dittschar, M. Salvietti, M.-T. Lin, M. Zharnikov, C. M. Schneider, J. Camarero, J. J. de Miguel, R. Miranda, and J. Kirschner, *Phys. Rev. B* 57, 5340 (1998).
179. J. Henk and B. Johansson, *J. Electron Spectrosc. Relat. Phenom.* 105, 187 (1999).
180. A. Beckmann, *Surf. Sci.* 349, L95 (1996).
181. R. Paniago, R. Matzdorf, G. Meister, and A. Goldmann, *Surf. Sci.* 325, 336 (1995).
182. R. Schmitz-Hübsch, K. Oster, J. Radnik, and K. Wandelt, *Phys. Rev. Lett.* 74, 2995 (1995).
183. P. Segovia, E. G. Michel, and J. E. Ortega, *Phys. Rev. Lett.* 77, 3455 (1996).
184. F. G. Curti, A. Danese, and R. A. Bartynski, *Phys. Rev. Lett.* 80, 2213 (1998).
185. H. Hoekstra, *Surf. Sci.* 205, 523 (1988).
186. J. Henk and W. Schattke, *Comput. Phys. Commun.* 77, 69 (1993).
187. S. V. Halilov, J. Henk, T. Scheunemann, and R. Feder, *Surf. Sci.* 343, 148 (1995).
188. J. Heinrichs, *J. Phys.: Condens. Matter* 12, 5565 (2000).
189. W.-H. Steeb, "Hilbert Spaces, Generalized Functions and Quantum Mechanics." B.I. Wissenschaftsverlag, Mannheim, 1991.
190. E. D. Hansen, T. Miller, and T.-C. Chiang, *J. Phys.: Condens. Matter* 9, L435 (1997).
191. K. Garrison, Y. Chang, and P. Johnson, *Phys. Rev. Lett.* 71, 2801 (1993).
192. C. Carbone, E. Vescovo, O. Rader, W. Gudat, and W. Eberhardt, *Phys. Rev. Lett.* 71, 2805 (1993).
193. C. Carbone, E. Vescovo, R. Kläsges, D. Sarma, and W. Eberhardt, *Solid State Commun.* 100, 749 (1996).
194. R. Kläsges, D. Schmitz, C. Carbone, W. Eberhardt, P. Lang, R. Zeller, and P. H. Dederichs, *Phys. Rev. B* 57, R696 (1998).
195. P. van Gelderen, S. Crampin, and J. Inglesfield, *Phys. Rev. B* 53, 9115 (1996).
196. C. Bradley and A. Cracknell, "The Mathematical Theory of Symmetry in Solids." Clarendon, Oxford, 1972.
197. P. H. Dederichs, K. Wildberger, and R. Zeller, *Physica B* 237–238, 239 (1997).
198. P. Bruno, *Phys. Rev. B* 52, 411 (1995).
199. J. J. Paggel, T. Miller, and T.-C. Chiang, *Phys. Rev. Lett.* 81, 5632 (1998).
200. R. Matzdorf, A. Gerlach, R. Hennig, G. Lauff, and A. Goldmann, *J. Electron Spectrosc. Relat. Phenom.* 94, 279 (1998).
201. D. Reiser, J. Henk, H. Gollisch, and R. Feder, *Solid State Commun.* 93, 231 (1995).
202. F. Frentzen, J. Henk, N. Irmer, R. David, B. Schmiedeskamp, U. Heinzmann, and R. Feder, *Z. Phys. B: Condens. Matter* 100, 575 (1996).
203. C. Fabry and A. Pérot, *Ann. Chim. Phys.* 19, 115 (1899).
204. M. Born and E. Wolf, "Principles of Optics: Electromagnetic Theory of Propagation, Interference and Diffraction of Light," 3rd ed. Pergamon, Oxford, 1965.
205. P. Voisin, G. Bastard, and M. Voos, *Phys. Rev. B* 29, 935 (1984).
206. J. J. Paggel, T. Miller, and T.-C. Chiang, *Science* 283, 1709 (1999).
207. A. Beckmann, *Surf. Sci.* 326, 335 (1995).